

Quantitative simulation of synaptic vesicle release at the neuromuscular junction

Jun Ma

CMU-CB-14-100

May 2014

School of Computer Science
Carnegie Mellon University
Pittsburgh, PA 15213

Thesis Committee:

Markus Dittrich, Advisor

Nathan Urban, Advisor, Chair

Russell Schwartz

James Faeder (University of Pittsburgh)

Stephen Meriney (University of Pittsburgh)

*Submitted in partial fulfillment of the requirements
for the degree of Doctor of Philosophy.*

Copyright © 2014 Jun Ma

Keywords:

Monte Carlo simulation, MCell, synaptic vesicle release, short-term plasticity, frog neuromuscular junction, mouse neuromuscular junction, active zone, ultrastructure, lipid-membrane interaction.

To my parents Yongliang Ma, Cuilian Ding, and my wife Chialing Tsai.

*In memorial of my first advisor,
Dr. Joel Stiles (1958-2011),
former director of NRBSC*

Abstract

Nerve signals in the form of action potentials are relayed between neurons through specialized connections called synapses via neurotransmitter released from synaptic vesicles. The release process is Ca^{2+} dependent, and relies on fusion of neurotransmitter filled synaptic vesicle with the presynaptic membrane. During high frequency stimulation, the amount of vesicle release increases at some synapses (e.g., frog neuromuscular junction (NMJ)), a process known as short-term plasticity. Due to the micron scale size of the presynaptic active zone where vesicle fusion takes place, experimentally study is often difficult. Thus, computational modeling can provide important insight into the mechanism of synaptic vesicle release at active zones. In the first part of my thesis, I used the frog NMJ as a model synapse for computer simulation studies aimed as testing various mechanistic hypotheses proposed to underlie short-term plasticity. Building off a recently reported excess-binding-site model of synaptic vesicle release at the frog NMJ (Dittrich et al., 2013), I have investigated several mechanisms of short-term facilitation at the frog NMJ. My studies placed constraints on previously proposed mechanistic models, and concluded that the presence of a second calcium sensor protein on synaptic vesicles distinct from synaptotagmin, can explain known properties of facilitation observed at the frog NMJ. In addition, I was able to identify a second facilitation mechanism, which relied on the persistent binding of calcium bound synaptotagmin molecules to lipids of the presynaptic membrane. In the second part of my thesis, I investigated the structure function relationship at active zones, with the hypothesis that active zones are organized from the same basic synaptic building block consisting of a docked vesicle and a small number of closely associated voltage-gated-calcium-channels (VGCCs). To test this hypothesis, I constructed a vesicle release model of the mouse NMJ by reassembling frog NMJ model building blocks based on electron-microscopy imaging data. These two models successfully predicted the functional divergence between frog and mouse NMJ in terms of average vesicle release and short-term plasticity. In the meanwhile, I found that frog NMJ loses facilitation when VGCCs were systematically removed from active zone. By tracking Ca^{2+} ions from each individual VGCCs, I further show how the difference in short-term plasticity between frog and mouse NMJ may rise from their distinct release building block assemblies.

In summary, I have developed a stochastic computer model of synaptic transmission, which not only shed light on the underlying mechanisms of short-term plasticity, but was also proved powerful in understanding structural and functional relationships at synaptic active zones.

Acknowledgments

It is a hard journey through all these years to pursue a Ph.D. I could not make it without the help from many people, and I owe my thanks to all of them. First of all, I would like to thank my advisor, Dr. Markus Dittrich, for his insight and patience that guide me through years of research and studies. Markus not only helped me establishing a clear view of scientific thinking, shaping my understanding of being a researcher, he also spent enormous amount of time editing and commenting my scientific documents, which dramatically honed my scientific writing skills. I could not make so much progress without his encouragement and supervision, while his optimism towards difficulties and accuracy towards details will influence the rest of my life.

I owe great thanks to Dr. Nathan Urban, the chair of my advisor committee, who agreed to supervise me at my most difficult time. He guided me into the wonderful world of neuroscience, taught me the way of critical thinking, and offered me great opportunities to learn more for my interest.

I have to thank Dr. Stephen Meriney. Many parts of my research in modeling will be meaningless without the experimental data collected at Meriney lab. I would like to thank him for spending time editing my scientific document, for encouraging and helping prepare presentations at international academic meetings, and for giving his insightful suggestions on my thesis work.

I would like to thank Dr. Russell Schwartz and Dr. James Faeder for being in my committee. The suggestions from them helped me a lot in shaping my thesis work.

I would like to thank all members of Biomedical Applications Group (former NRBSC) at Pittsburgh Supercomputing Center (PSC), including but not limited to Dr. Pallavi Ishward, Dr. Arthur Wetzel, Greg Hood, Jacob Czech, Dr. Hugh Nicholas, Dr. Alexander Ropelewski, and importantly our coordinator Pat Sudac. I also appreciate the support from all PSC staff members.

I would like to thank all members (and former members) of Urban lab, including but not limited to Dr. Pete Jones, Dr. Jing Wen, Dr. Shreejoy Tripathy, Mathew Geramita, Santosh Chandrasekaran, Shawn Burton, Yiyi Yu, and Greg LaRocca.

I would like to thank all members (and former members) of Meriney lab, including but not limited to Dr. Fujun Luo, Tyler Tarr, Lauren Kelly, Justin Ingram, and Thomas Price.

I would like to thank Dr. Tom Bartol, Dr. Terry Sejnowski, and all people at San Diego working on MCell development.

I would also like to thank all staff members of SCS at Carnegie Mellon University, especially our program coordinator Thomas Gulish.

Special thanks to all people who helped me out when I experience the most difficult time at the 3rd year of my Ph.D studies. In addition to whom mentioned above, these people also include but not limited to Dr. Daniel Zuckerman, Dr. Panayiotis Benos, Dr. Ivet Bahar, and Dr. Robert Murphy.

Last but not least, I owe great thanks to Dr. Joel Stiles, my first advisor. He led me into the field of mirophysiology simulation, encouraged and guided me through early years of my Ph.D studies. As an old Chinese saying, “even he (she) teaches you for only one day, treat him (her) like a parent for rest of your life. (一日为师, 终身为父)”. Although Joel left us too early, he will always be in my memory.

Besides all the people I worked with, I really need to thank my parents Yongliang Ma, Cuilian Ding, my wife Chialing Tsai, and my to-be-born son. Without their physical and mental support, I would not be able to overcome all the difficulties in the way.

Contents

§ Chapter 1. Introduction.....	1
1.1 Types of synapses.....	1
1.2 Basics of a chemical synapse.....	2
1.3 Molecular machinery of vesicle release.....	4
1.4 Short-term plasticity in synaptic transmission.....	5
1.5 Ultrastructure of the frog and mouse neuromuscular junction.....	8
1.6 Thesis overview.....	11
§ Chapter 2. Modeling Methods.....	15
2.1 Introduction to computational cell modeling.....	15
2.2 Theories behind MCell simulation.....	18
2.2.1 Computer simulation of microphysiology: scale matters.....	18
2.2.2 Description of model geometry in MCell.....	19
2.2.3 Molecules in MCell.....	20
2.2.4 Diffusion in MCell.....	21
2.2.5 Reactions in MCell.....	23
2.3 MCell modeling pipeline.....	25
§ Chapter 3. Development of a vesicle release model that predicts short-term plasticity.....	27
3.1 Introduction.....	27
3.2 Methods.....	31
3.2.1 Excess-calcium-binding-site model.....	31
3.2.2 Vesicular Ca^{2+} sensor sites.....	32
3.2.3 VGCC and Ca^{2+} binding kinetics.....	33
3.2.4 Runtime logistics.....	35
3.2.5 Analyzing MCell simulation results with software AZ.....	36
3.2.6 Vesicle fusion mechanisms.....	37
3.2.7 Recording transmitter release from the frog neuromuscular junction.....	38
3.3 Results.....	39
3.3.1 Experimental model constraints.....	39
3.3.2 Residual free Ca^{2+} does not generate facilitation.....	42
3.3.3 Facilitation via persistent binding of Ca^{2+} bound synaptotagmin to the presynaptic membrane.....	45
3.3.4 A model with additional second sensors sites shows facilitation and agrees well with all our constraints.....	50
3.3.5 Second sensor model with energy based fusion mechanism further improves agreement.....	

with experimental constraints	55
3.3.6 Facilitation is enhanced under low external calcium conditions	64
3.3.7 Nanodomain coupling of VGCCs to synaptic vesicles persists during repeated stimuli....	65
3.3.8 The effect of exogenous buffer on Ca ²⁺ binding to synaptotagmin and the second sensor site	67
3.4 Discussion	69
3.4.1 Residual free Ca ²⁺ does not lead to facilitation	69
3.4.2 Facilitation via a second Ca ²⁺ sensor on synaptic vesicles	71
3.4.3 Persistent binding of synaptotagmin leads to facilitation	73
3.4.4 Conclusions	73
§ Chapter 4. Comparative analysis of frog and mouse NMJ models reveals the structure and function relationship	75
4.1 Introduction and motivation.....	75
4.2 Results.....	79
4.2.1 Distinct synaptic function observed at frog and mouse NMJ.....	79
4.2.2 A comprehensive mouse NMJ vesicle release model constructed by reassembling active zone building blocks of frog NMJ model	80
4.2.3 Frog and mouse NMJs are distinguished by individual vesicle release probability after a single action potential stimulus.....	85
4.2.4 Frog and mouse NMJs are distinguished by short-term plasticity.....	88
4.2.5 The short-term plasticity differences are insensitive of the modeled release mechanism ..	90
4.2.6 Vesicle release is triggered by nanodomain coupling between VGCC and Ca ²⁺ sensors...	91
4.2.7 Short-term plasticity is affected by the spatial organization of VGCCs.....	97
4.2.8 Short-term plasticity at the frog NMJ is affected by distance between associated VGCC and the docked vesicle	103
4.3 Discussion	106
§ Chapter 5. Discussion	111
5.1 Exploration of short-term plasticity mechanisms	111
5.2 Exploration of structure-function relationship in active zone.....	115
5.2.1 Refining the model with emerging new experimental data	115
5.2.2 Presynaptic homeostatic regulation of structure and function within active zones of frog NMJ.....	116
5.2.3 Presynaptic changes in active zone structure in a mouse model of LEMs	116
5.2.4 Unreliable single vesicle release sites at CNS synapses	117
5.3 Conclusions.....	118
Bibliography	121

List of Figures

Figure-1.1: Chemical synapse.	3
Figure-1.2: Illustration of molecules involved in synaptic vesicle fusion.....	5
Figure-1.3: Different forms of short-term plasticity	7
Figure-1.4: Active zone ultrastructure of frog and mouse NMJ.....	10
Figure-1.5: Illustration of microdomain and nanodomain.	11
Figure-2.1: Illustration of molecule reactions in MCell.	24
Figure-2.2: MCell modeling pipeline.....	26
Figure-3.1: Front and top view of frog neuromuscular junction active zone model.....	32
Figure-3.2: Illustration of binding sensors on bottom of a vesicle.....	33
Figure-3.3: Short-term plasticity of excess-binding-site model.	44
Figure-3.4: Schematic view of the persistent binding model state diagram.	46
Figure-3.5: Persistent binding site model.	48
Figure-3.6: Effects of exogenous buffer on persistent binding site model.	50
Figure-3.7: Schematic view of the bottom of a synaptic vesicle showing the 28 Y binding sites ...	53
Figure-3.8: 28-Y-site model.	55
Figure-3.9: Illustration of energy sampling.	56
Figure-3.10: Schematic view of the bottom of a synaptic vesicle showing the 16 and 68 Y binding sites.	60
Figure-3.11: Summary of 68-Y-site-energy model.	62
Figure-3.12: Summary of the 16-Y-site-energy-model with $k_{on}=4\times 10^8 \text{ M}^{-1}\text{s}^{-1}$ for synaptotagmin.	64
Figure-3.13: PPF as a function of external $[\text{Ca}^{2+}]$ shows an increase in PPF as $[\text{Ca}^{2+}]$ is decreased	65
Figure-3.14: Fractional contribution of increasing numbers of VGCC to release during repeated stimuli.....	66
Figure-3.15: Effects of Exogenous buffer on binding sites.....	68
Figure-4.1: Active zone organization in frog and mouse NMJs.....	78
Figure-4.2: Assembly of a basic building block of synaptic active zone.....	79
Figure-4.3: Comparison of geometric in the frog and mouse NMJ models.....	83
Figure-4.4: Different configurations of VGCCs in mouse active zone	86
Figure-4.5: CRR and release latency of frog and mouse NMJ	88
Figure-4.6: Comparison of frog and mouse NMJ in terms of short-term plasticity	90
Figure-4.7: VGCC contributions to vesicle release at frog NMJ	93
Figure-4.8: Analysis of mouse NMJ under single action potential	95

Figure-4.9: Conditional probability of vesicle release	96
Figure-4.10: Analysis of short-term plasticity	100
Figure-4.11: Configurations of VGCCs in frog NMJ for plot shown in Figure-4.10A	101
Figure-4.12: Contribution from VGCCs to primed vesicle.....	102
Figure-4.13: Illustration of VGCC location randomization.....	105
Figure-4.14: Synaptic function affected by VGCC-vesicle distance at frog NMJ.....	105
Figure-5.1: Effect of LEMS on the active zone and vesicle release	117

List of Tables

Table-1: List of model parameters.....	34
Table-2: Average number of released vesicles (n_r) and PPF for a range of persistent binding site models with different values for k_{lipid_on} and k_{lipid_off}.....	47
Table-3: Average number of released vesicles (n_r) and PPF for a range of second sensor models for different choices of parameters.....	54
Table-4: Average number of released vesicles (n_r), PPF, and CRR for a range of second sensor energy models for different choices of parameters	59
Table-5: Comparison of models matching our experimental n_r and PPF.....	62

§ Chapter 1. Introduction

This chapter provides the general background knowledge of my thesis work. More detailed background information of specific topics will be presented at beginning of each chapter. At the end of Chapter 1, I will give an overview of all thesis chapters.

The survival of animals, especially vertebrates with complex behavioral patterns, depends critically on the activity of their nervous system. In higher animals, information from sensory organs is processed in the central nervous system (CNS), whereas nerve signals encoding decisions made by the CNS travel along nerve fibers until reaching effectors such as the muscle fiber. Nerve signals, so called action potentials, propagate along neurons which are connected to each other with specialized structures called *synapses*, where signals are not only faithfully relayed, but also amplified or weakened. Formally, the term *synapse* refers to an individual, specialized contact that comprises electron-dense pre-and post synaptic membranes (Atwood and Karunanithi, 2002). For their role in relaying nerve signals across neurons and modifying nerve signals during information coding, synapses have received a lot of attentions, which led to years of research disclosing more and more details about its structure and function.

1.1 Types of synapses

Synapses can be divided into two major types: electrical synapses and chemical synapses. The electrical synapses consist of intracellular channels allowing small molecules to pass between neurons. Composed of proteins known as connexins, these channels form structures called gap-junctions in a narrow space of 2-4 nm between two adjoining cells, which allows inter-cellular exchange of ions and small molecules such as cAMP (Gilula and Feldman, 1978; Oshima, 2014). Unlike chemical synapses,

the electrical synapse does not distinguish between pre- and postsynaptic neurons, since the signal transduction at gap-junctions is usually bi-directional.

My thesis will focus on the chemical synapse (Figure-1.1), where presynaptic signals are transmitted uni-directionally via small molecules called neurotransmitters to the postsynaptic cell. There are different types of neurotransmitters such as acetylcholine (ACh, major neurotransmitter at neuromuscular junctions), glutamate, and GABA. The receptors for these transmitters can be ionotropic or metabotropic (Nicholls et al., 2000). Ionotropic receptors are themselves ion channels opened by binding of neurotransmitter. The metabotropic receptors do not have ion channels, but instead trigger a second messenger signal cascade upon neurotransmitter binding. This cascade can lead to opening of other ion channels on the membrane. As a consequence of neurotransmitter binding to receptors, the subsequent postsynaptic current can be either excitatory (glutamate, ACh) or inhibitory (GABA, glycine), thus they provide a rich regulatory repertoire for neuronal signal transduction.

1.2 Basics of a chemical synapse

Most signals across neurons are mediated by chemical synapses, which convert electric signals carried by action potentials into the chemical signals through release of neurotransmitter. As shown in the electron-microscopic image of synapses in Figure-1.1A, the presynaptic neuron forms a close contact with the postsynaptic cell membrane, with a dense population of molecules aggregated in the contact area called the *postsynaptic density*. Several synaptic vesicles containing neurotransmitters are docked on the presynaptic cell membrane. On the other hand, a large number of non-docked vesicles forms a ready-to-release pool, waiting to replenish the released vesicles (Kaeser et al., 2011; Südhof, 2012). Figure-1.1B shows a synaptic vesicle release cycle as well as the voltage-gated Ca^{2+} dependent

vesicle release process. Upon arrival of an action potential, the rise in membrane potential triggers opening of the voltage-gated-calcium-channels (VGCCs) in the presynaptic membrane, which causes an influx of Ca^{2+} ions into the presynaptic terminal. These Ca^{2+} ions then diffuse within the terminal and bind to Ca^{2+} sensor molecules on synaptic vesicles such as the synaptotagmin (Chapman, 2008). Sufficient Ca^{2+} binding then triggers the fusion of docked synaptic vesicles with the presynaptic cell membrane through a series of steps which are not yet fully understood (Südhof, 2012). Vesicle fusion releases neurotransmitter into the synaptic cleft, which diffuse and bind to receptors on the postsynaptic membrane after diffusion, and so initiate an action potential (or trigger a second messenger signal cascade) in the postsynaptic cell. To ensure proper synaptic function, unused neurotransmitters must be cleared immediately after firing of the synapse, either degraded by enzyme, or transported back into presynaptic terminal through the re-uptake pump for future uses.

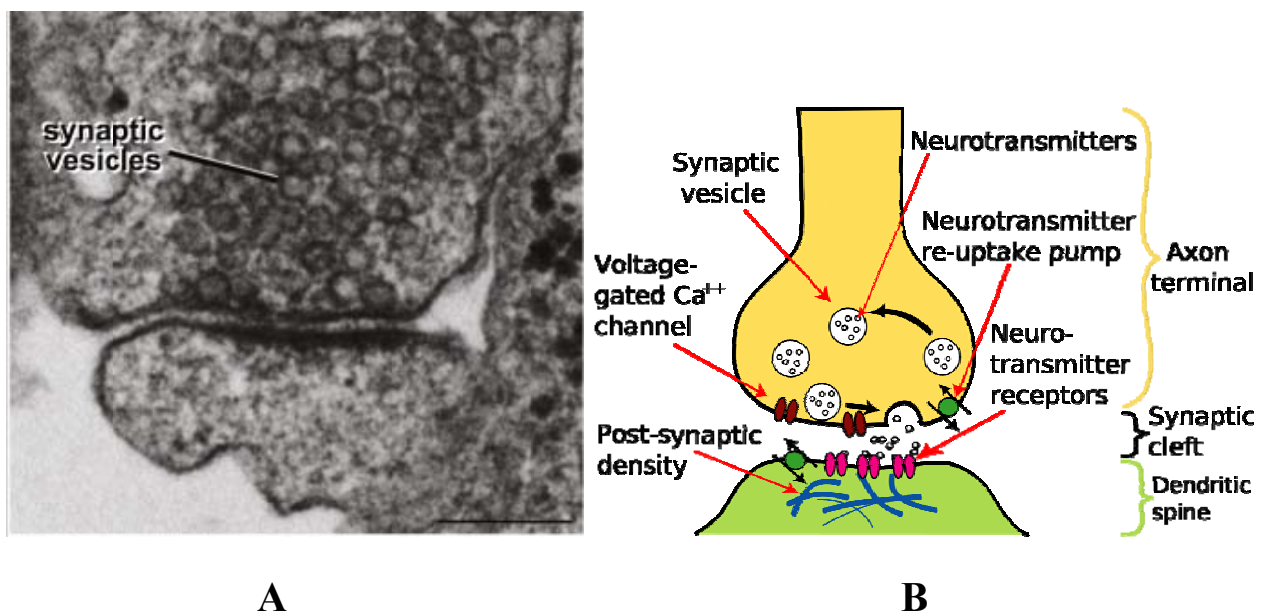


Figure-1.1: Chemical synapse. A. Electron-microscopy image showing structure of a chemical synapse at mouse hippocampal neurons. Bar = 200 nm. (Kaeser et al., 2011) B. Illustration of synaptic transmission at chemical synapses. Image is from <http://en.wikipedia.org/wiki/Neurotransmission>.

1.3 Molecular machinery of vesicle release

The vesicle release happens on a millisecond time scale, so fast that synaptic vesicles containing neurotransmitter have to become pre-docked on the presynaptic membrane via a series of processes including vesicle mobilization and priming (Pan and Zucker, 2009). While many proteins are linked to presynaptic functions such as active zone organizing (RIM), vesicle priming (Munc 13), fusion of the docked synaptic vesicle with presynaptic membrane involves the so called SNARE complex (Südhof and Rothman, 2009), a protein complex composed of syntaxin and SNAP-25 on the presynaptic membrane, and synaptobrevin on the vesicle membrane (Figure-1.2). Studies have shown that one SNARE complex may be enough to initiate vesicle fusion by forming the fusion pore, but three or more SNARE complexes significantly stabilize the fusion pore and increase the probability of vesicle fusion (Hua and Scheller, 2001; Shi et al., 2012). The Ca^{2+} dependent synaptic vesicle fusion process is significantly accelerated when Ca^{2+} bound protein synaptotagmin interacts with the SNARE complex (Martens et al., 2007; Chapman, 2008; Shin et al., 2010) (Figure-1.2). Based on overwhelming experimental evidence (Chapman, 2008), synaptotagmin is now accepted as the major Ca^{2+} sensor for fast Ca^{2+} -dependent synaptic vesicle release, with a copy number of up to 15 per vesicle (Takamori et al., 2006). Since a single synaptotagmin molecule has five Ca^{2+} binding sites (Südhof and Malenka, 2008), they together provide up to 75 binding sites on a vesicle. The important role of synaptotagmin for fast transmitter release was confirmed in a recent computational study which investigated the mechanistic details of action potential triggered vesicle release at the frog NMJ (Dittrich et al., 2013).

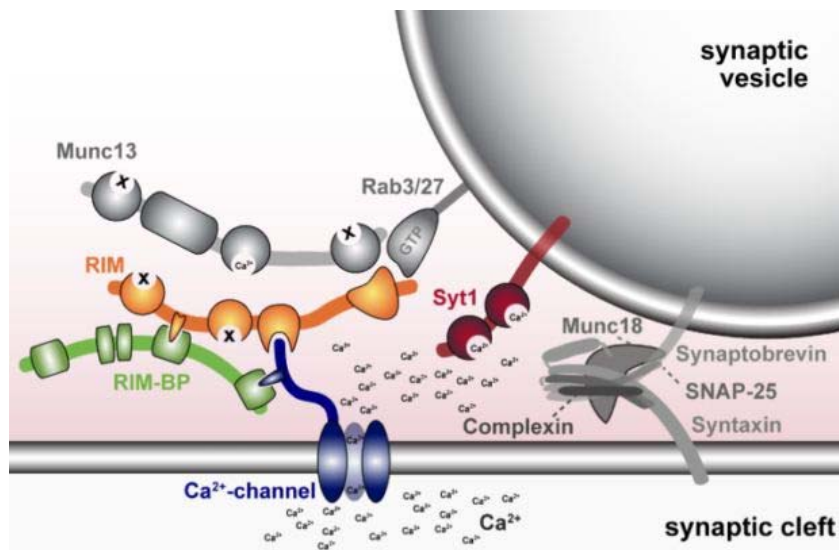


Figure-1.2: Illustration of molecules involved in synaptic vesicle fusion. Showing synaptic vesicle and the presynaptic membrane, and major active zone proteins (RIMs, Munc 13, and RIM-BPs), VGCC, a partial assembled SNARE-complex (composed of synaptobrevin on vesicles and SNAP-25 and syntaxin on plasma membrane), Munc18, complexin, and key synaptic proteins (Rab3 and synaptotagmin-1 [Syt1]). Adapted from (Kaeser et al., 2011)

1.4 Short-term plasticity in synaptic transmission

The magnitude of synaptic vesicle release in most synapses following action potential stimulation is subject to modulation known as short-term synaptic plasticity. The modulation can either strengthen (referred to as facilitation, augmentation, or potentiation, depending on the duration), or weaken (depression) the signal during repetitive action potential stimuli (Figure-1.3, Eccles et al., 1941; Feng, 1941; Magleby KL, 1987; Fisher et al., 1997; Zucker and Regehr, 2002). For example, in the frog neuromuscular junction (NMJ) where the motor neuron axon makes contact with muscle fibers, facilitation is the prominent form of short-term plasticity extending over tens to hundreds of milliseconds following an action potential. During a pair or a train of action potentials, the magnitude of synaptic vesicle release can increase up to several times the size of the initial release (Tanabe and

Kijima, 1989; Cho and Meriney, 2006). In contrast, the short-term plasticity at mouse NMJ is mostly observed as slight depression where the vesicle release during repetitive action potential stimuli actually decreases (Ma et al., 2014b). These use-dependent responses are also seen in other types of synapses, such as the well studied crayfish NMJ and the cerebellar Purkinje cells in the central nervous system (CNS), leading to a characterized diversity of synaptic short-term plasticity among synapses (Atwood and Karunanithi, 2002). With the time scale lying between fast neural signaling (milliseconds) and the experience-induced learning (minutes or more), short-term plasticity might be involved in many processes such as motor control and working memory. On the other hand, although the importance of Ca^{2+} ions had been recognized (Zucker and Regehr, 2002), it is still unclear on molecular level how short-term plasticity is triggered, which makes computer simulation a valuable tool for short-term plasticity mechanism investigation.

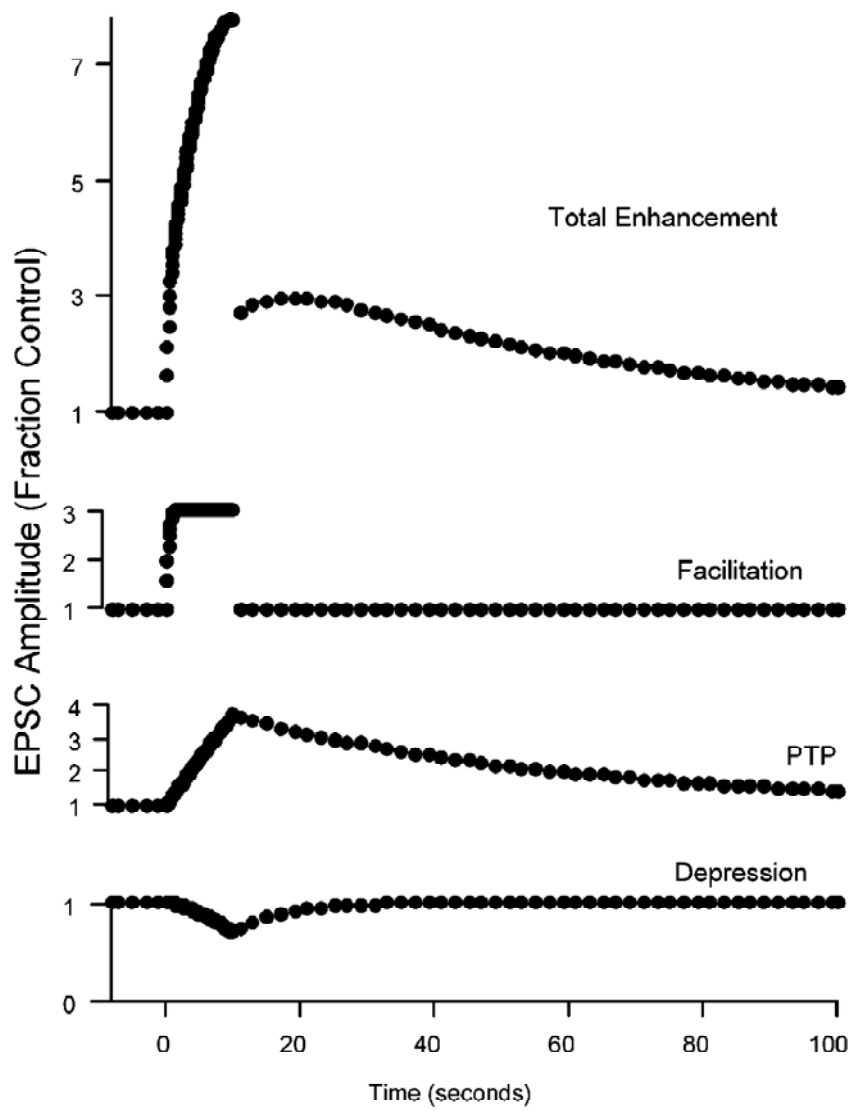


Figure-1.3: Different forms of short-term plasticity: facilitation, post-tetanic potentiation (PTP), depression. Adapted from (Zucker and Regehr, 2002)

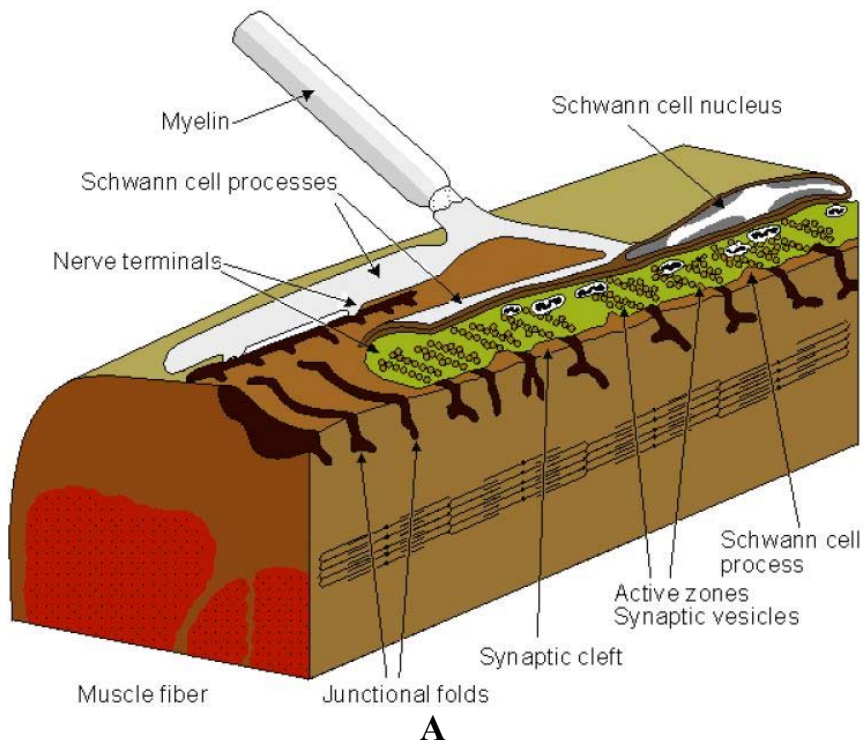
1.5 Ultrastructure of the frog and mouse neuromuscular junction

The frog neuromuscular junction (NMJ) is a model synapse featuring strong and reliable synaptic transmission as well as prominent facilitation under repetitive action potential stimuli. Morphologically at the NMJ, the axon divides into branches forming presynaptic terminal contacting with postsynaptic junction folds of the muscle fiber (Figure-1.4A). The synaptic vesicles are docked at a specialized structure known as *active zone* which is also where Ca^{2+} dependent vesicle fusion occurs. A frog NMJ contains an average of 700 linear (1 μm long) active zones separated from each other by around 1 μm (Heuser et al., 1974), and the ultrastructure of such a single active zone has been revealed by previous freeze-fracture and electron-tomography studies (Pawson et al., 1998; Harlow et al., 2001). As shown in Figure-1.4B, C and D, the frog NMJ active zone is composed of two lines of docked synaptic vesicles and four lines of intramembraneous particles, a fraction of which are thought to be VGCCs. The whole active zone is supported by scaffold structures referred as pegs, ribs and beams (Figure-1.4D) whose functions remain unclear besides anchoring and connecting all active zone components, although it is believed that at least some of the pegs and ribs might be involved directly in regulating fusion of the docked vesicles (Harlow et al., 2001).

Compared to frog NMJ, the mammalian NMJ looks quite different. The mouse NMJ consists of numbers of swellings or boutons, each with a area of 5-10 μm^2 containing 15-20 active zones (Slater, 2008). Electron-microscopic (EM) imaging studies show that these active zones are 100-200 nm long separated from each other by 500 nm. The active zone has 2-3 docked vesicles (2 on average), and two double rows of intramembraneous particles on each side of the docked vesicles (Figure-4E-G) (Nagwaney et al., 2009).

Here in both frog and mouse NMJ, VGCCs and docked vesicles are closely located to each other

(<100 nm), forming a tight spatial and functional coupling called nanodomain (Eggermann et al., 2012). Thus one or two VGCCs can control the gating of one vesicle's release (Figure-1.5). In contrast, many other synapses (e.g., rat hippocampus mossy fiber) form a loose microdomain coupling between VGCC and vesicles (Vyleta and Jonas, 2014) where VGCCs are located distant away (>100nm) from docked vesicles and a group of VGCCs may be necessary for gating one vesicle's release (Figure-1.5). Since the active zone ultrastructure is organized differently among synapses (Zhai et al., 2001), it is appealing to associate the structure with their distinct functions, which is a hypothesis to be further addressed in Chapter 4.



B

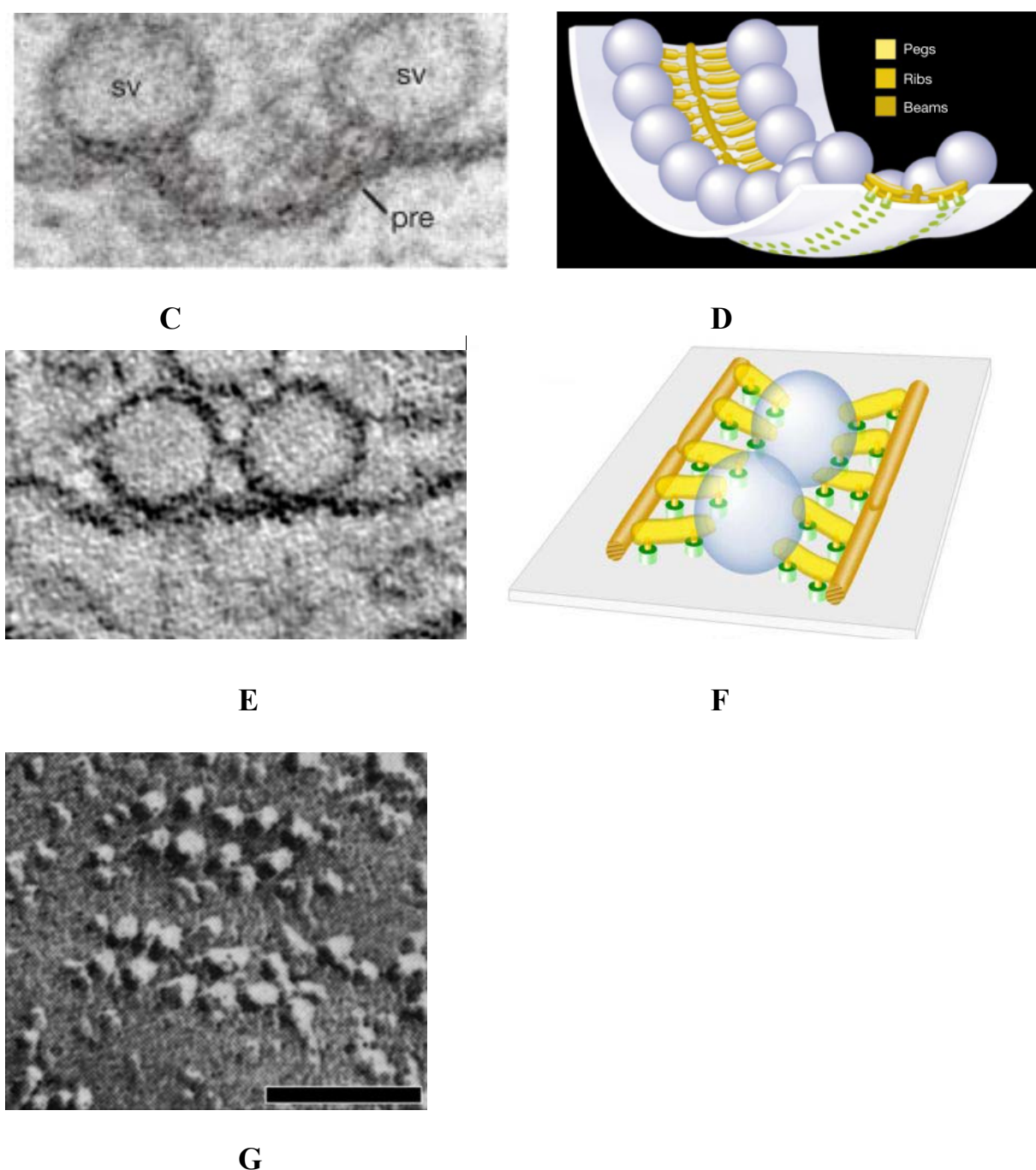


Figure-1.4: Active zone ultrastructure of frog and mouse NMJ. **A.** Illustration of the entire frog NMJ, shown axon, presynaptic terminal containing active zones, postsynaptic junction folds and muscle fiber. **B, C.** EM image of top view (**B**), and side view (**C**) of an active zone in frog NMJ. **B** shows the intramembraneous particles in roughly four lines. Bar = 100 nm. **B** shows the docked synaptic vesicles (SV) and presynaptic membrane (pre). **D.** Illustration of the frog NMJ active zone structure, showing vesicles (purple ball), intramembraneous particles (green), and scaffold structure called pegs, ribs, and beams (yellow). Adapted from (Harlow et al., 2001). **E, F, G.** EM image of side view (**E**) and top view (**G**) of a mouse NMJ active zone. Bar = 50 nm in **G**. **F.** Illustration of the mouse NMJ active zone structure, showing two docked vesicles and intramembraneous particles (green).

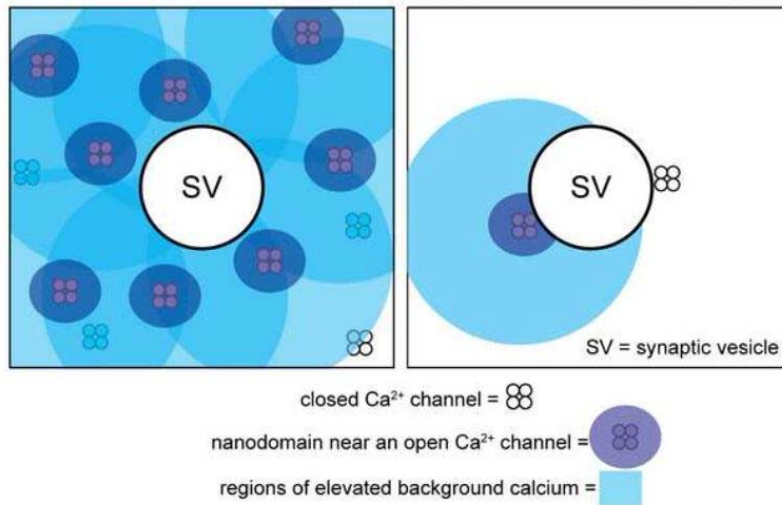


Figure-1.5: Illustration of microdomain (left) and nanodomain (right). Adapted from (Tarr et al., 2013)

1.6 Thesis overview

Despite of the fundamental role of Ca^{2+} -dependent synaptic vesicle release in the nervous system, the detailed mechanisms coupling Ca^{2+} influx and vesicle fusion remain only partially understood, largely due to the technical difficulties in observing living synapses. The sub-micron size of the active zone is below the resolution of ordinary optical microscopy techniques, while electron-microscopic imaging provides sufficient resolution but only allows one to study static samples. Although the emerging super resolution imaging techniques might potentially overcome such difficulties (Rust et al., 2006; Galbraith and Galbraith, 2011), computer simulation alternatively provides a powerful tool to address questions that cannot be investigated directly via experimental approaches. MCell (see Chapter 2) is a simulation package for particle-based reaction diffusion models, and is capable of handling complex arbitrary 3D meshes. Therefore MCell stands out as an idea tool for studying synaptic vesicle

release. In my thesis, as an effort to interrogate mechanisms of calcium-triggered vesicle release and use-dependent changes in release magnitude at neuromuscular junction (NMJ), I have completed:

1. Construct a vesicle release model at the frog NMJ that predicts short-term plasticity.
2. Investigate the structure-function relationships in synaptic active zone via MCell simulations of the frog and mouse NMJs.

The thesis is composed of three parts.

In Chapter 2, I will provide an introduction into the theory, methods and algorithms underlying MCell.

In Chapter 3, I will present the work of developing a vesicle release model that predicts facilitation using experimental data from frog NMJ, which shed new insight into the short-term plasticity mechanism. First, I will investigate the role of free residual calcium in facilitation. By extending our previously proposed excess binding site model to multi action potential stimuli, I will show that free residual calcium accumulation is not significant for facilitation. Next, I will introduce a persistent binding model motivated by recent biochemical evidence. Finally, I will present the development of the second binding site model, and show how such a model with 10-30 second Ca^{2+} binding sites, in addition to synaptotagmin, can successfully predict facilitation while remaining constrained by other experiments.

Given the short-term plasticity vesicle release model developed in Chapter 3, Chapter 4 will focus on the structural and functional relationship at active zones. First, I will present a mouse NMJ model via reassembling active zone building blocks used in the frog NMJ model according to corresponding EM data, and show that a significant synaptic functional divergence between the two NMJs could be

successfully predicted by the two models. Secondly I will discuss the observed nanodomain coupling at both frog and mouse NMJ. Thirdly, I will show how short-term plasticity is affected when changing the size and shape of a frog active zone. Later analysis further reveals how active zone structure affects primed/unbound vesicles, and subsequently how this affects short-term plasticity.

§ Chapter 2. Modeling Methods

In this chapter, I will present the simulation methodologies used in my thesis work. After introduction of general cell modeling techniques, I will focus on the theoretical foundations behind MCell, the stochastic modeling software I used for the thesis. I will end this chapter with a brief exposition of the steps required for building an MCell model.

2.1 Introduction to computational cell modeling

Given the complex and interwoven chemical reactions in a cell, modeling is an essential step to understand how cellular level phenomenon rise from those molecular interactions. Unlike in classical physics systems, the intrinsic molecular and spatial heterogeneity in sub-cellular space prohibits the description of the cellular systems using simplified equations. However, with the recent surge of computational modeling combined with experiments, we are closer than ever to system-level understanding of cellular activities. Depending on the scale and purpose of modeling, one should choose appropriate modeling methods for questions of their interest.

Perhaps the most straight forward quantitative model of a biological system is to use a mathematical equation describing relationship between two variables. Despite of a few examples such as modeling F-actin polymerization rate as a function of profiling (Vavylonis et al., 2006), such a simplified model in general cannot explain the interactions between a number of molecule species, which is very common in biological modeling.

For models involving multiple interplaying variables, ordinary differential equations (ODEs) are commonly used to describe their interactions usually in form of chemical reactions, where molecules

are represented by their concentration, and the reaction rates are usually specified using mass action kinetics or enzyme kinetic laws such as Michaelis-Menten or Hill kinetics (Wilkinson, 2009). The *non-spatial deterministic* ODE approaches are suitable for problems with large quantity of molecules that can be described using law of mass action, without much concern of geometrical heterogeneity. For moderate size problems, the ODE models can be easily numerically solved by solvers from various software packages or computational environments (e.g., Matlab, Octave, or XPPaut (<http://www.math.pitt.edu/~bard/xpp/xpp.html>)).

The classical ODE models assume that changes of reactants in amount of concentration are continuous and deterministic governed by the reactions. However, the deterministic approach failed to capture some important details of the biological system. If observations from the biological system are significantly influenced by unpredictable or even unknown factors, especially when amount of reactants is low, the observations tend to become noisy or stochastic (e.g., single-cell dynamics, neuron firing). Therefore to capture such stochastic fluctuations, deterministic ODE models should be replaced with the *non-spatial stochastic* models where events (reactions) are triggered with help of probabilities and random numbers. One common technique is to model reactions as a Markov jump process which is usually known as the Gillespie algorithm. Starting from the initial state, the algorithm generates time course trajectories over distinct time windows, by constantly sampling the “jump” events (reactions) (Li et al., 2008; Wilkinson, 2009). Since each run of the stochastic simulation would be different, properties of the system should be averaged over a sufficiently large number of simulations to reduce the Monte Carlo error. In addition, for large scale biological systems involving huge number of molecular states (e.g., intracellular signaling network) where manually defining all reactions has become impossible, the rule-based modeling languages such as BioNetGen (http://bionetgen.org/index.php/Main_Page) are powerful tools for model construction (Faeder, 2011).

The methods discussed so far did not address the spatial heterogeneity. On the other hand, in some models reactants cannot be assumed well-mixed within cell since the reaction dynamics are deeply affected by reactants' non uniform spatial distribution (e.g., actins during cell mitosis, retrograde axon cargo transport, and morphogen gradients in embryo). Therefore *spatial deterministic* the partial differential equations (PDEs) are used to model the spatially heterogeneous and compartmentized dynamics. PDE models combined with finite element methods (FEM) discretize the space into small voxels in which the concentration gradient of molecules is ignored (well mixed within voxel). Differential equations are used to compute fluxes and reactions between and within voxels, mimicking Brownian Motion of the molecules. Examples of software packages capable of using *spatial deterministic* approaches include the Virtual Cell (VCell, <http://www.nrcam.uchc.edu/index.html>, (Cowan et al., 2012)), as well the Neuron (<http://www.neuron.yale.edu/neuron/> (Brette et al., 2007)) which is widely-used for modeling of single neuron firing and neural-network.

The spatial deterministic approaches suffer the same problem as non-spatial deterministic approaches, when the amount of reactants within a voxel is too low for mass action description. In addition to that, for models requiring precise spatial description of irregular shapes, implementing the space subdivision using FEM may become complex and time consuming. When encountering these problems during modeling, the particle-based *spatial stochastic* approach using Monte Carlo 3D diffusion and chemical reaction is more suitable (Note that this is different from *non-spatial stochastic* simulation of ODE/PDEs, although Monte Carlo is used in both cases). In the particle-based model, all molecules are regarded as particles living in the space. At each iteration step, the simulated molecules' Brownian motion are stochastically sampled from a diffusion parameter distribution. When two molecules approach close to each other, occurrence of reactions is tossed according to reaction

probability calculated from mass action kinetics (Stiles and Bartol, 2001). Examples of software packages include ChemCell (<http://www.chemcell.sandia.gov> , (Plimpton and Slepoy, 2005)), Smoldyn (<http://www.smoldyn.org> , (Andrews et al., 2010)), and MCell (<http://www.mcell.psc.edu> , (Stiles and Bartol, 2001)). Since it has to process every individual molecule at each iteration, the computation cost of these *spatial stochastic* approaches may significantly increase in presence of large amount of reactants, for which the *spatial deterministic* PDE/FEM is more appropriate.

2.2 Theories behind MCell simulation

2.2.1 Computer simulation of microphysiology: scale matters

Computer simulation of biological systems has to be tailored for questions at different scales. For example, molecular dynamic simulation reveals atomic level resolution of interactions within biological macromolecules (e.g., Khalili-Araghi et al., 2009). On the cellular level, recent whole-cell modeling incorporating metabolome, genome, transcriptome, and proteome provided system level insight into cellular behavior (Karr et al., 2012). For multiple cells, simulation of neuron-circuits involving multiple neurons provided system level behavior of networks (e.g., Aradi and Erdi, 1996; Adesnik and Scanziani, 2010; Grimes et al., 2010), while more ambitious plans simulating all neurons in the human brain (86 billion neurons) is underway (Blue Brain Project, <http://www.artificialbrains.com/blue-brain-project>).

For simulation of systems on the sub-cellular level, taking into account their realistic 3D structure may become critical for some questions (Stiles and Bartol, 2001). For example, when asking how active zone ultrastructure affects synaptic function, it is unavoidable to incorporate the actual

ultrastructure, including shape, size, and distribution of membrane-embedded molecules. Synaptic function highly depends on buffered Ca^{2+} dynamics around docked synaptic vesicles and VGCCs. Since their spatial scale is between nanometer and microns, a realistic 3D approach for quantitative modeling of microphysiology is required. Monte Carlo Cell (MCell) is a software for reaction-diffusion simulation of microphysiological systems with arbitrary 3D geometry (Stiles et al., 1996; Stiles and Bartol, 2001; Kerr et al., 2008; Czech et al., 2009). Compared to deterministic modeling, MCell's stochastic modeling is able to characterize the intrinsic stochastic fluctuations in a non well-mixed microphysiology system. In the meanwhile, the optimized simulation algorithm of MCell guarantees efficient model explorations such as rapid model error-checking, model parameter searching, and condition variations.

2.2.2 Description of model geometry in MCell

The model geometry used in MCell simulations is represented by triangulated surface meshes. There are several ways of preparing a model geometry, e.g. from reconstruction of segmented volumetric image data (e.g., EM reconstruction) (Coggan et al., 2005), or via computer-aided-design software such as Blender (Czech et al., 2009).

While EM-reconstruction provides highly realistic representations of model geometry from a biological system under consideration (e.g., pre-synaptic terminal at nanometer scale resolution), simulations using EM-reconstruction could address questions that are highly related to the high-resolution structure. For example, MCell simulation using high-resolution serial EM tomography revealed the importance of ectopic neurotransmission (release distant away from postsynaptic density) at cholinergic synapses of the chick ciliary ganglion (Coggan et al., 2005). In another example, MCell simulation using serial EM reconstruction demonstrated that neurotransmitter diffusion rates are

affected by the extracellular space (Kinney et al., 2013). In principle, any technique that provides 3D structural data with sufficient resolution can be used as MCell modeling input. Although EM-reconstruction provides precise description of the real geometry, it is very time consuming and requires significant manual labor. Presently, automated or semi-automated EM segmentation methods are still in an immature stage. In addition to that, if all reactions are taking place within a 3D polygon from EM reconstruction, the polygon must be free of any leaking point so that molecules during a simulation won't exit the polygon unexpectedly. Thus extra careful model checking is essential for successful modeling, which requires extra manual labor.

Alternatively, if the precise geometry description is not critical to the studied problem, the model geometry can be created *in silico* based on geometrical information from experiments (e.g., number of components, size, and distance), while simulations of such models are still powerful shedding lights into the system (e.g., Nadkarni et al., 2010; Scimemi and Diamond, 2012; Dittrich et al., 2013). The simplest way of constructing MCell model geometries *in silico* is to use CellBlender, which is an add-on for the 3D modeling and animation software Blender (<http://www.blender.org/>). CellBlender provides a user-friendly environment for rapid creation and editing of arbitrary 3D geometric models through interactive GUI, along with the ability of mesh surface annotation, molecule placement, and parameter definition (Czech et al., 2009). The finished model can be exported as the MCell model file (.mdl) from CellBlender.

2.2.3 Molecules in MCell

There are two types of molecules in MCell: volume molecules with a three dimensional diffusion coefficient and surface molecules with a two dimensional diffusion coefficient. Both volume and surface molecules are point particles and can either be mobile or static. The surface molecules occupy

triangular tiles on mesh surfaces and diffuse through hopping between tiles. In MCell, specified numbers of molecules can be added onto mesh objects or into arbitrary unions/intersections of volumes enclosed by mesh objects.

Surface molecules typically represent transmembrane proteins with distinct extracellular, intramembranous, and cytoplasmic domains, such as ion channels, sodium-potassium ATPases, and G-protein coupled receptors. Thus the surface molecules have spatial orientations with respect to the diffusion spaces. In MCell, orientation of surface molecules is specified in reaction definition, while reactions involving surface molecules can only happen when reactants have the right orientation.

2.2.4 Diffusion in MCell

Diffusion in MCell is modeled according to Fick's second law:

$$\left(\frac{\partial C}{\partial t}\right)_{x,y,z} = D_L \left[\left(\frac{\partial^2 C}{\partial^2 x}\right)_t + \left(\frac{\partial^2 C}{\partial^2 y}\right)_t + \left(\frac{\partial^2 C}{\partial^2 z}\right)_t \right]$$

where C is concentration, D_L is the diffusion constant. It can be shown that for a single molecule of diffusion constant D_L at the origin, given time interval of Δt , the probability that it moves a distance r in a random direction is given by:

$$p(r, t) = \frac{1}{(4\pi D_L \Delta t)^{\frac{3}{2}}} e^{-\frac{r^2}{4D_L \Delta t}} (4\pi r^2 dr)$$

This equation is then used to pick a radial diffusion step length for each diffusing molecule during each iteration of an MCell simulation, In particular, by selecting a random number uniformly between 0 and 1, and the radial displacement R can be computed via:

$$X = \text{cdf}(r, t) = \int_0^r p(r, t) \cdot |\partial S_r^3| \cdot dr$$

$$= \int_0^R \frac{4\pi r^2}{\pi^{3/2}\lambda^3} e^{-r^2/\lambda^2} dr = \text{erf}(R') - \frac{2}{\sqrt{\pi}} R' e^{-R'^2}$$

where $|\partial S_r^3|$ is the surface area of 3-dimensional sphere of radius r , $\lambda = \sqrt{4D_L \Delta t}$ and $R' = R/\lambda$.

To speed up computation, MCell solves this distribution for regularly spaced values X when initializing the simulation, and stores the results in a look-up table. At run-time, a single random number is used to look up the corresponding R' and multiply λ to get the distance.

The direction of diffusion is sampled separately. One randomly picks up ϕ uniformly from $[0, 2\pi]$, and determines θ by solving $Y = \frac{1-\cos\theta}{2}$, with Y uniformly picked up from $[0, 1]$ at random. The combined ϕ and θ then determine a direction in the 3D polar coordinate. Again MCell uses look-up tables to speed up computation at run-time. The volume molecule is then updated with the new location.

All the above also apply to surface molecules with trivial modifications. For sampling travel distance of surface molecules, the cdf is now:

$$X = \int_0^{R'} 2r' e^{-r'^2} dr' = 1 - e^{-R'^2}$$

which can be reversed to get R' directly:

$$R' = \sqrt{-\ln(X)}$$

For direction, one only needs to pick up ϕ uniformly from $[0, 2\pi]$. Since a surface molecule only “lives” on the triangular tiles of the meshed surface, after diffusion it will move to the new tiles at the destination. In the case in which a destination tile is already being occupied, MCell will sample the distribution again for a new tile.

If a diffusing volume molecule hits a mesh surface during its movement, there are three possible cases: (1) if the surface is transparent to that molecule, the molecule position will be updated as if the mesh surface does not exist, (2) if the surface is absorptive to that molecule, then the molecule will be removed from simulation, (3) if the surface is reflective to that molecule, then the molecule will be specularly reflected.

2.2.5 Reactions in MCell

MCell can simulate uni- and bi-molecular reactions by assuming mass action kinetics. The following paragraphs derive the reaction probability at each reaction circumstance, where MCell stochastically sample from these probabilities to determine whether the reaction happens.

For unimolecular transitions, if a molecule leaves current state with rate k , the distribution of its expected life time is given by:

$$P(t) = \frac{1}{k} e^{-kt}$$

For reactions between surface molecules, on each time step, MCell checks neighbors of a surface molecule for reactants (Figure-2.1A). If the one reactant molecule exists at density σ , the expected number of reactions in Δt is $k\sigma\Delta t$. On the other hand, the probability of finding the reactants and have the reaction happening is $p_{\Delta t}\sigma A$, where $p_{\Delta t}$ is the probability of reacting and A is the area of tile.

Equating the two formulae gives:

$$p_{\Delta t} = \frac{k}{A} \Delta t$$

For reactions between a volume molecule and a surface molecule, MCell uses ray-tracing algorithm to check whether the moving ray of the volume molecule hit the surface with surface reactant. Suppose the surface molecule is sitting on a tile of area A (Figure-2.1B), it can be shown that once the volume molecule hit the surface, the probability of reaction happening is given by $p = \frac{2\sqrt{\pi}k}{Av}$, where $v = \lambda/\Delta t$.

For reactions between two volume molecules, one can think of it as a moving volume molecule in the center of a disk of area $A = \pi r_{\text{int}}^2$ sweeping a cylindrical volume (Figure-2.1C), where r_{int} is the interaction radius. It can be shown that the probability of reaction happening between two volume reactants (indexed as 1 and 2) within the interaction radius is:

$$p = \frac{\sqrt{\pi}}{2(v_1 + v_2)A} k$$

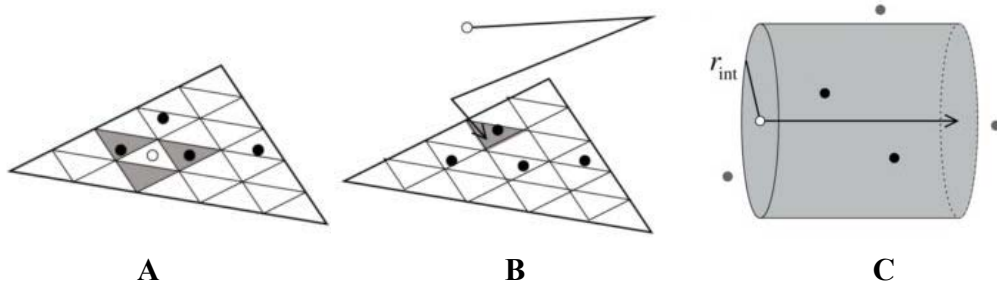


Figure-2.1: Illustration of molecule reactions in MCell. **A.** Surface molecules occupy tiles. The tested molecule (open circle) encounter other molecules (black circles) if they are in the three adjacent tiles (shaded). **B.** Volume molecules (open circle) diffuse and hit the surface molecule (black circle) in the shaded tile. **C.** Volume molecule (open circle) meets other volume molecules (black circle) in the cylinder of radius r_{int} . The gray molecule is missed. Adapted from (Kerr et al., 2008).

2.3 MCell modeling pipeline

Figure-2.2 shows a general pipeline of modeling using MCell. Step 1 “create geometry”, step 2 “generate meshes”, and step 3 “annotate meshes” can all be done using CellBlender, which is especially designed for convenient 3D mesh manipulations. With CellBlender, one can define properties of meshes (reflective, absorptive, or transparent to some molecules) or place surface molecules on the surface mesh. One can also easily define molecules, reactions, and set up simulation parameters with CellBlender. After the model is exported from as MCell model description language (MDL), in step 4 one needs to add all remaining on-spatial model parameters according to MDL syntax. In step 5, MCell starts the simulation as specified in all prepared MDL files. Due to the stochastic aspect of MCell, to get proper averages of model parameters one typically needs to run multiple statistically independent simulations. Depending on the model’s complexity and availability of computing resources, the simulation may take from seconds to weeks. In step 6, simulation results can be visualized via CellBlender, providing an easy way for model verification and data presentation. MCell can also generate ASCII/binary format files containing time-series quantity of every (or specified) molecule species, which become input of custom scripts for further analysis. Often during model development, the model parameters are refined iteratively to make predictions constrained by experimental data, so that step 5 and 6 may be executed repeatedly before a satisfying model is in hand.

MCell Model Building Pipeline

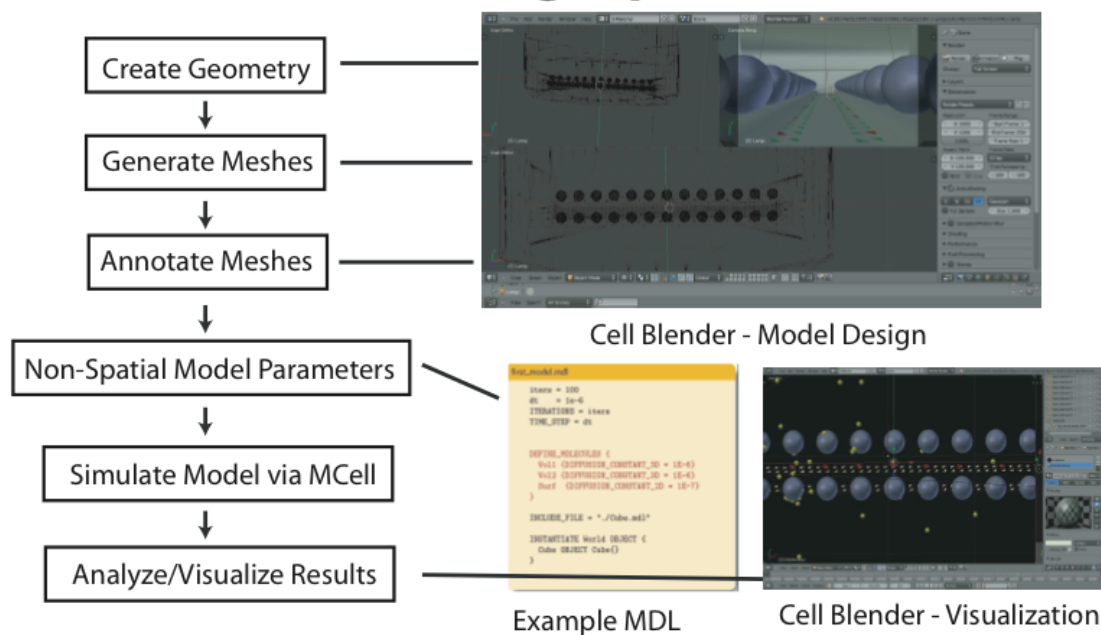


Figure-2.2: MCell modeling pipeline

§ Chapter 3. Development of a vesicle release model that predicts short-term plasticity

In this chapter, I will focus on my proposed aim 1---- to construct a vesicle release model that predicts short-term plasticity, where a successful implementation of this model means to comply with all the experimental constraints listed in Chapter 2. As reviewed in section 3.1, various mechanisms were proposed to explain the changes of vesicle release intensity. Starting from a relatively simple hypothesis, I will first investigate the free residual Ca^{2+} accumulation hypothesis in the excess binding site model. After I show that free residual Ca^{2+} cannot produce the observed facilitation, I will move on to models with more complex kinetics: the persistent binding model which assumes the synaptotagmin/lipid membrane interactions, and the second binding site model which assumes another type of Ca^{2+} binding sensors accounting for facilitation. Finally, I will present a model with a relatively low number of second binding sites. Employing an energy-barrier-crossing release scheme, I will show the model is consistent with all experimental constraints, and also show how these models help to gain understanding of short-term plasticity.

3.1 Introduction

The communication between neurons is mediated by chemical synapses, which convert electrical into chemical signals via an action potential-evoked, calcium-dependent synaptic vesicle fusion process (Miledi, 1960; Kuffler and Yoshikami, 1975; Heuser, 1989). Since the seminal studies of synaptic function at the frog neuromuscular junction (NMJ) by Katz and coworkers (Fatt and Katz, 1953; Katz and Miledi, 1965a, 1968), a large number of experimental, and more recently computational studies, have been conducted to investigate synaptic facilitation mechanisms (Magleby, 1979; Yamada and Zucker, 1992; Tank et al., 1995; Tang et al., 2000; Matveev et al., 2006). In addition, integrative

computer models have been developed to study synaptic vesicle priming, facilitation, and depression (Dittman et al., 2000; Pan and Zucker, 2009).

During action potential-triggered synaptic vesicle fusion, Ca^{2+} bound synaptotagmin molecules are thought to mediate fast vesicle fusion (<0.2 ms) through interactions with SNARE proteins and the presynaptic membrane (Martens et al., 2007; Chapman, 2008; Rizo, 2010). Based on a large body of experimental evidence (Bommert et al., 1993; DiAntonio et al., 1993; Littleton et al., 1993; Nonet et al., 1993; Geppert et al., 1994; Mikoshiba et al., 1995; Fukuda et al., 2000) synaptotagmin is now accepted as the major Ca^{2+} sensor for fast Ca^{2+} -dependent synaptic vesicle fusion, with a copy number of up to 15 per synaptic vesicle (Takamori et al., 2006). Since each synaptotagmin molecule has five Ca^{2+} binding sites (Südhof and Malenka, 2008), they together provide up to 75 Ca^{2+} binding sites per vesicle. Based on this structural insight we have recently developed an excess-calcium-binding site model of synaptic vesicle release at the frog NMJ (Dittrich et al., 2013).

At many synapses, the magnitude of synaptic vesicle fusion following action potential stimulation can be temporarily modulated by a process called short-term synaptic plasticity. This form of modulation occurs through either strengthening (referred to as facilitation, augmentation, or potentiation, depending on the duration) or weakening (depression) of the synaptic response during a train of action potential stimuli (Eccles et al., 1941; Feng, 1941; Magleby KL, 1987; Fisher et al., 1997; Zucker and Regehr, 2002). At the frog NMJ, facilitation is a prominent form of short-term plasticity extending over tens to hundreds of milliseconds following an action potential (Tanabe and Kijima, 1992; Mukhamedyarov et al., 2006; *this paper*). Here, during a pair or train of stimuli, the magnitude of synaptic vesicle release can increase to several times the size of the initial response (Tanabe and Kijima, 1989; Cho and Meriney, 2006).

Several mechanisms have been advanced to explain synaptic facilitation. Early studies identified the critical role of residual Ca^{2+} in facilitation, proposing that Ca^{2+} ions that entered during the first action potential lingered in the nerve terminal and added to the Ca^{2+} ions entering the terminal during subsequent stimuli. However, quantitative studies using Ca^{2+} uncaging combined with Ca^{2+} indicator dyes showed that residual free Ca^{2+} acting on vesicular Ca^{2+} binding sites could not explain facilitation (Blundon et al., 1993; Delaney and Tank, 1994; Schneggenburger and Neher, 2000; Zucker and Regehr, 2002). The pioneering work of Katz and Miledi (Katz and Miledi, 1965b, 1968) in the frog NMJ hypothesized that residual Ca^{2+} wasn't free, but remained bound to Ca^{2+} sensors and thereby enhanced vesicle release during future excitation events. Subsequently, the idea that residual bound Ca^{2+} could enhance subsequent stimuli evolved to include the possibility of multiple Ca^{2+} binding sites; some mediating vesicle fusion and release, and others responsible for facilitation during subsequent stimuli (Kamly and Zucker, 1994; Atluri and Regehr, 1996; Tang et al., 2000). Other studies suggested that facilitation resulted from saturation of local Ca^{2+} buffers such as calbindin-D28k and parvalbumin, giving rise to increased available Ca^{2+} during subsequent stimuli (Blatow et al., 2003; Matveev et al., 2004; Müller et al., 2007).

Additional insight into the nature of the Ca^{2+} binding sites responsible for transmitter release and facilitation came from studies of the effect of exogenous Ca^{2+} buffers. These experiments showed that the addition of a fast exogenous Ca^{2+} buffer (e.g. Fura-2, BAPTA) significantly reduced both facilitation and initial transmitter release (Tanabe and Kijima, 1992; Yamada and Zucker, 1992; Mukhamedyarov et al., 2009). In contrast, the addition of a slow Ca^{2+} buffer such as EGTA reduced facilitation without substantially affecting single action potential triggered transmitter release (Tanabe and Kijima, 1992; Suzuki et al., 2000; Mukhamedyarov et al., 2009). The differential effect of EGTA

on high frequency stimulus-triggered facilitation, versus single action potential-evoked vesicle fusion, suggests that two distinct processes acting on different timescales are involved. While there is clear evidence that Ca^{2+} binding to synaptotagmin is involved in the action potential-triggered fast fusion step (Lynch et al., 2007; Chapman, 2008; Südhof and Malenka, 2008; Rizo and Rosenmund, 2009), at the NMJ no distinct molecular player mediating facilitation has so far been identified. In contrast, studies at the calyx of Held have shown that facilitation may be mediated by Ca^{2+} binding to neuronal- Ca^{2+} -sensor proteins (NCS) which directly enhance Ca^{2+} flux through P/Q type VGCCs during repeated stimuli (Catterall and Few, 2008; Mochida et al., 2008; Catterall et al., 2013). Since the NMJ is thought to only contain N-type VGCCs (Kerr and Yoshikami, 1984) for which no Ca^{2+} binding induced facilitation has been reported, it is presently not known if this mechanism might also act at the NMJ.

Given the lack of direct experimental evidence into the presynaptic Ca^{2+} -dependent facilitation mechanism, computational modeling can provide crucial insight and also aid in consolidating physiological and biochemical evidence into a functional hypothesis at the sub-microscopic level. As an initial step toward this goal we recently developed an excess-calcium-binding site model of action potential triggered vesicle release at the frog NMJ (Dittrich et al., 2013). Using stochastic simulations via MCell (Stiles and Bartol, 2001; Kerr et al., 2008) we were able to show that a model with eight synaptotagmin molecules (corresponding to 40 Ca^{2+} binding sites) without any ad-hoc Ca^{2+} binding site cooperativity could predict experimentally known properties of single action potential-triggered vesicle fusion (Dittrich et al., 2013). Unfortunately, our model was not able to predict the experimentally observed facilitation during multiple stimuli at high frequency. Thus, via a step-by-step evolution of our excess-calcium-binding site model, and constrained by experimental observations, we have tested the viability of several facilitation mechanisms at the microscopic level. We found that a model with a second Ca^{2+} binding site, distinct from synaptotagmin, provided good agreement with our experimental

constraints. In addition, we identified a novel fusion mechanism based on the binding of Ca^{2+} bound synaptotagmin to the presynaptic membrane. Our results yield new insight into the facilitation mechanism at the frog NMJ and also provide constraints on the number and kinetic properties of a potential second sensor site whose precise molecular identity is presently unknown.

3.2 Methods

3.2.1 Excess-calcium-binding-site model

We started our investigation of short-term synaptic facilitation at the frog NMJ using our previously developed excess-calcium-binding site model (Dittrich et al., 2013) and simulated it using MCell (www.mcell.org). Our model contained a realistic 3D representation of a frog NMJ AZ created via CellBlender (www.mcell.org) based on published averages (Figure-3.1). The mesh geometry was created in CellBlender and then exported directly into MCell's model description language (MDL). 26 synaptic vesicles (diameter 50 nm) were arranged in two rows lateral to a trough containing VGCCs at a vesicle-channel stoichiometry of 1:1 (Luo et al., 2011), and at locations suggested by published estimates (Heuser et al., 1979; Pawson et al., 1998; Stanley et al., 2003). During each single or repeated action potential stimulation event, VGCCs opened stochastically (see below) giving rise to Ca^{2+} influx into the terminal, Ca^{2+} diffusion within the terminal, Ca^{2+} binding to sensors sites on synaptic vesicles, and vesicle fusion once a sufficient number of Ca^{2+} ions had bound in a prescribed binding pattern (vesicle fusion mechanism, see below). Key model parameters are listed in Table-1.

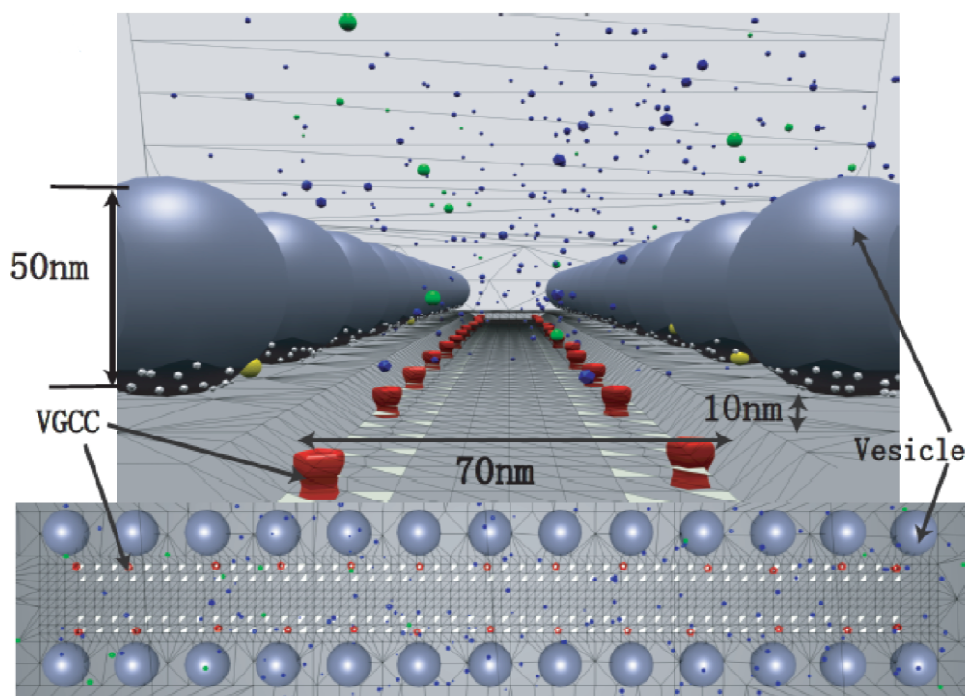


Figure-3.1: Front (top) and top (bottom) view of frog neuromuscular junction active zone model. Shown are docked vesicles, voltage-gated-calcium-channels (VGCC, red), Ca^{2+} ions (green), Ca^{2+} sensors (white), bound Ca^{2+} sensors (yellow), bound Ca^{2+} buffer (blue).

3.2.2 Vesicular Ca^{2+} sensor sites

The arrangement and number of synaptotagmin Ca^{2+} binding sites on synaptic vesicles was identical to the one employed in our previous study (Dittrich et al., 2013). 40 Ca^{2+} sensor sites corresponding to eight synaptotagmin molecules with five Ca^{2+} binding sites each were located at the bottom of individual synaptic vesicles on mesh tiles opposite to the presynaptic membrane (Figure-3.2). This arrangement of Ca^{2+} sensor sites was used both in our control and persistent-binding model. Our second sensor facilitation model included additional sensor sites (number of second sensor sites, $n_Y = 8, 12, 16, 28, 68, 144$) on vesicle mesh tiles located in an annular region directly above the synaptotagmin molecules (see Figure 3.7, 3.10A and C). These second sensor sites represented the as of yet unknown Ca^{2+} binding proteins that might be involved in facilitation.

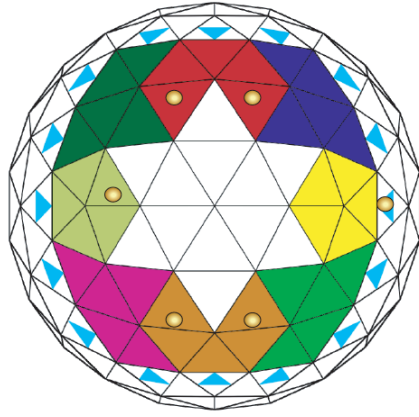
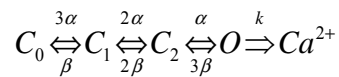


Figure-3.2: Illustration of binding sensors on bottom of a vesicle. Colored large triangular meshes in the middle represent synaptotagmin binding sensors (40 in total, grouped in 5 to reflect the 5 binding sites of synaptotagmin molecule). The smaller cyan triangular meshes are the 2nd binding sites (16 as shown, only existing in the 2nd binding site model). The orange circles are bound Ca²⁺ ions.

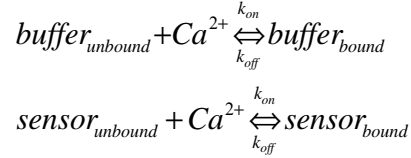
3.2.3 VGCC and Ca²⁺ binding kinetics

The kinetics of the VGCCs was identical to the one in our excess-calcium-binding-site model (Dittrich et al., 2013) and consisted of three closed (C_0 , C_1 , C_2) and one open (O) state which inter-converted according to the following scheme



The time dependent rate constants α , β , and k were determined based on experimentally measured action potentials and whole cell Ca²⁺ current (Dittrich et al., 2013). The time dependence of α , β , and k for repeated stimuli (paired pulse and five pulse experiments) were generated by stitching together the appropriate number of single action potential waveforms interspersed by the appropriate interstimulus intervals at a resting potential of -60 mV. Once in the open state, VGCCs released Ca²⁺ ions into the presynaptic terminal with a time dependent rate constant k . Ca²⁺ ions then diffused within the terminal

and could either bind to Ca^{2+} sensor sites on vesicles (synaptotagmin and/or second sensor binding sites) or 2 mM of static Ca^{2+} buffer molecules distributed randomly and uniformly throughout the terminal according to



with the appropriate rate constants taken from the literature (see Results, Table 1). The significance of the effect of exogenous Ca^{2+} buffer BAPTA and EGTA on vesicle release and PPF were tested using a one-way ANOVA ($p < 0.01$) followed by Tukey's post-hoc test ($p < 0.01$). All statistical analyses were conducted using Matlab (v. 7.8.0, MathWorks).

Input Parameters	Description	References
Diffusion coefficient for free Ca^{2+} ions	$D = 6 \times 10^{-8} \text{ cm}^2 \text{ s}^{-1}$	(Winslow et al., 1994)
VGCC kinetic properties	See Methods, conductance of open VGCC: 2.4 ps	(Dittrich et al., 2013)
Synaptotagmin-like calcium binding site (synaptotagmin)	$k_{on} = 1 \times 10^8 \text{ M}^{-1} \text{ s}^{-1}$ $k_{off} = 6000 \text{ s}^{-1}$	(Davis et al., 1999)
Endogenous calcium buffer	Concentration = 2mM $k_{on} = 1 \times 10^8 \text{ M}^{-1} \text{ s}^{-1}$ $k_{off} = 1000 \text{ s}^{-1}$	(Xu et al., 1997) (Yazejian et al., 2000)
synatotagmin/lipid interaction rates in the persistent binding model	$k_{lipid_on} = 2 \times 10^3 \text{ M}^{-1} \text{ s}^{-1}$ $k_{lipid_off} = 10 \text{ s}^{-1}$	based on (Hui et al., 2005)
Second calcium sensor binding site (Y sensor)	$k_{on} = 6 \times 10^6 \text{ M}^{-1} \text{ s}^{-1}$ $k_{off} = 36 \text{ s}^{-1}$	based on (Matveev et al., 2006)
BAPTA Ca^{2+} kinetics	$k_{on} = 4 \times 10^8 \text{ M}^{-1} \text{ s}^{-1}$ $k_{off} = 88 \text{ s}^{-1}$	(Eggermann et al., 2012)
EGTA Ca^{2+} kinetics	$k_{on} = 1 \times 10^7 \text{ M}^{-1} \text{ s}^{-1}$ $k_{off} = 0.77 \text{ s}^{-1}$	(Eggermann et al., 2012)

Table-1: List of model parameters

3.2.4 Runtime logistics

All simulations were conducted using MCell version 3.1 (rev. 788) using a custom binary output format to allow for efficient storage and compression of simulation results. The algorithms underlying MCell have been described in detail in the past (Stiles and Bartol, 2001; Kerr et al., 2008). For each distinct simulation condition (different numbers of Ca^{2+} sensor sites on vesicles, varying external Ca^{2+} concentration, etc.) we typically performed 10,000 statistically independent runs using different random number seeds and used these to compute proper averages of observables. To compute the variance of observables we resampled the data by randomly picking 1000 (corresponding to the experimentally observed average number of AZ per NMJ, (Dittrich et al., 2013)) out of the 10,000 MCell simulations and then repeated this procedure 1000 times to compute the standard deviation between samples. The resampling and data plotting were performed using Matlab (v7.8.0, MathWorks). We used a short simulation time step ($dt = 10$ ns) to ensure accurate spatial sampling of the confined regions between VGCCs and the Ca^{2+} binding sites on vesicles. During each simulation run, we kept track of Ca^{2+} ions emitted from individual open Ca^{2+} channels and recorded which sensor sites on synaptic vesicles bound Ca^{2+} ions from which VGCC and pulse (during multi-stimuli experiments). This allowed us to analyze if and to what degree Ca^{2+} ions from different stimuli contributed to release of synaptic vesicles. Scripts written in C++ and Python were then used to analyze the number and timing of vesicle release events post-simulation. With the exception of the runs to compute the CRR, all simulations were conducted at a physiological (in the frog) external Ca^{2+} concentration of 1.8 mM. Simulations were set up and analyzed on a local workstation (2.4GHz Core2-Duo iMac) and simulated on several computer clusters at the Pittsburgh Supercomputing Center (Salk, an SGI Altix 4700 shared-memory NUMA system with 144 Itanium 2 processors; Axon a 256 core cluster with 64 quad-core 2.5 GHz Intel Xeon E5420 CPUs). A typical duration for a single paired-pulse simulation with 10 ms inter-

stimulus interval was about 2 hours. The simulation results will be analyzed through third party software (e.g., active zone analyzer (AZ)).

3.2.5 Analyzing MCell simulation results with software AZ

As mentioned above, I developed the C++ script called active zone analyzer (AZ) to analyze the MCell simulation output. Once started, AZ sweeps the folder where all MCell simulation output files are located. Since each output file is a statistically independent simulation record with unique random number seed, the model predictions are then averaged over these files to minimize stochastic errors.

When dealing with a simulation output file which is highly compressed for easy storage, AZ first retrieves relative data block for the requested molecule species after data decompression. The data block of molecule \mathbf{X} is a vector with a size equal to MCell simulation steps, where the vector's i^{th} element corresponds to count of molecule \mathbf{X} at step i . To find occurrence of vesicle release events, AZ scans the data blocks of molecules called *bound sensor* which are nothing but vesicle-dwelling sensors bound by Ca^{2+} ions. Since all *bound sensor* molecules on every vesicle are named distinctively, scanning corresponding data blocks with the vesicle fusion criteria described in section 3.2.6 will determine at what time (which simulation step) and which vesicle has a release event. Once a vesicle is found released, AZ marks it as *released* and stops scanning the data blocks of *bound sensors* dwelling on that vesicle for the remaining time steps, since we assume that a vesicle can release at most once during the entire simulation period. After finishing working on all MCell simulation output files, the vesicle release events will be stored in an output file, which can be easily handled by custom analysis scripts using Matlab or python. For different analysis purposes, AZ can also output files containing simulation information for questions such as which VGCC did a specific Ca^{2+} ion came from, or how many buffer molecules were bound by Ca^{2+} ions at a specific time step.

3.2.6 Vesicle fusion mechanisms

The vesicle fusion mechanism utilized as part of our control and persistent binding model was as described previously (Dittrich et al., 2013). Synaptotagmin molecules occupied by at least two Ca^{2+} ions were considered active and vesicles were released as soon as three out of a total of eight synaptotagmin molecules became active.

The fusion mechanism for our second sensor model was a straightforward extension of this release mechanism. More specifically, a vesicle was released once a given number of synaptotagmin and/or second sensor sites were active simultaneously. Second sensor sites were considered active once bound by a single Ca^{2+} ion. In addition, we used a Metropolis-Hastings (Metropolis et al., 1953; Hastings, 1970) sampling protocol to decide which vesicles should be released using

$$P = \min \left(\exp \left(- \frac{E_b - n_S \cdot \Delta E_S - n_Y \cdot \Delta E_Y}{k_B T} \right), 1 \right)$$

for computing the fusion probability. Here, $E_b = 40k_B T$ is the free energy barrier for vesicle fusion (Li et al., 2007; Martens et al., 2007), n_S , n_Y are number of active synaptotagmin and Y sites, and ΔE_S and ΔE_Y the respective reductions in free energy barrier toward vesicle fusion. This probability was evaluated every $0.5 \mu\text{s}$ with updated Ca^{2+} binding information, where $0.5 \mu\text{s}$ corresponds to our chosen data output interval. Note that the probability calculated here is proportional to but not exactly equivalent to the reaction probability within the time interval.

For our persistent binding model shown in Figure-3.4, since the number of active synaptotagmin molecules could only be determined post-simulation (Dittrich et al., 2013), the lipid binding step into and out of the persistent state also had to be computed post-simulation. To this end, we converted the

reaction rate constants for the persistent step into reaction probabilities and then used a Monte Carlo scheme to sample transitions of activated synaptotagmin molecules into a persistent state and back. Since the transition from the active to the lipid bound state and back was modeled as a unimolecular process we used the exponential relationship

$$P = 1 - \exp(-k \cdot dt)$$

to convert reaction rate constants to reaction probabilities. E.g., using $k_{\text{lipid_off}} = 10 \text{ s}^{-1}$ (Hui et al., 2005) and $dt = 0.5 \text{ }\mu\text{s}$ yielded $P_{\text{lipid_off}} = 5 \times 10^{-6}$. Similarly, a $k_{\text{lipid_on}} = 2 \times 10^3 \text{ s}^{-1}$ and $dt = 0.5 \text{ }\mu\text{s}$ resulted in $P_{\text{lipid_on}} = 1 \times 10^{-3}$. Here, $dt = 0.5 \text{ }\mu\text{s}$ corresponded to our chosen data output interval.

The post-simulation analysis of the transition kinetics into and out of the persistent state was an approximation since Ca^{2+} ions which were sequestered within a persistent synaptotagmin state during analysis could still bind and unbind Ca^{2+} ions in the underlying MCell simulation. However, since at most three out of eight synaptotagmin sites would be persistent simultaneously this effect had limited impact on overall system dynamics.

3.2.7 Recording transmitter release from the frog neuromuscular junction

Adult northern leopard frogs (*Ranapipeus*) were anesthetized with 0.4% tricaine and double pitched in compliance with the Institutional Animal Use and Care Committee at the University of Pittsburgh. The cutaneous pectoris muscle was dissected from frogs and placed in normal frog Ringer (NFR, in mM: 5 glucose, 116 NaCl, 10 Hepes buffer, 2 KCl, 1 MgCl_2 , 1.8 CaCl_2 , pH 7.4). For recordings, the nerve-muscle preparation was placed in a Sylgard-coated recording chamber. Evoked transmitter release was elicited by drawing the nerve into a suction electrode and stimulating (in pairs,

or in trains at 1-100 Hz) using a current that was 10X the threshold required to elicit a muscle contraction. Microelectrodes were pulled from borosilicate glass, filled with 3M potassium acetate (resistances 40-60 M Ω), and impaled into muscle cells to allow recording of nerve stimulation-evoked endplate potentials (EPPs) from postsynaptic muscle cells near visually identified neuromuscular junctions as described previously (Cho and Meriney, 2006). All data were collected and analyzed using Clampex10 software (Axon Instruments).

3.3 Results

3.3.1 Experimental model constraints

The philosophy behind modeling of biological systems is more or less like the Bayes inference: to make predictions based on the existing observations, with certain prior assumptions or knowledge about the system. A computational model of biological system was usually built on prior knowledge from existing studies (e.g., shape and dimension of active zone in my thesis), but unavoidably it introduced free parameters such as undetermined reaction kinetics, or molecule quantities. To determine these parameters, one needs a number of experimental observations that strictly constrain the model's behavior. Given the assumption that an experimentally constrained model may represent the real world system at least for the investigated questions, it can be used to make new predictions and provide new insight into the biological system.

The constraint (i) is the average vesicle release per active zone per action potential (average release, for short). This quantity is obtained through dividing size of postsynaptic end-plate potentials (EPPs, reflecting total number of synaptic quantal release at the terminal), by number of active zones in the terminal estimated by fluorescence imaging. It indicates how often active zone releases a vesicle,

and serves as basis where many other observations are built on. In frog NMJ, the observed average vesicle release is 0.51 ± 0.09 . The modeled average vesicle release is measured by averaging the number of vesicle release over all parallel simulations while the frog NMJ model contains only one active zone.

The constraint (ii) is the calcium release relationship (CRR). Specifically, experiments found vesicle release depends on approximately a 4th order relationship to external Ca^{2+} concentration at both frog and mouse NMJ (Dodge and Rahamimoff, 1967; Smith, 1988). In the model, we estimate vesicle release under varying external Ca^{2+} concentrations, and find CRR through logarithmic regression.

The constraint (iii) is the vesicle release latency, which means that according to experimental data, vesicle release takes place in a narrow, 1-1.5 ms wide time window with a delay of about 1 ms (Katz and Miledi, 1965b). Since we did not know when action potential onset occurred for the data shown in, in the modeling work, we will only compare shape of the simulated vesicle release time histogram with the experimental data.

All three experimental constraints above apply to single action potential stimulus. When studying the short-term plasticity of synaptic release, we included additional experiments.

We measured the magnitude of transmitter release during pairs of stimuli as estimated by the size of postsynaptic end-plate potentials (EPPs). We then plotted the ratio of second EPP to the first (paired-pulse ratio, PPR) at different inter-stimulus intervals (ISIs; Figure-14D). At a short ISI of 10 ms, we measured a significant PPR of 1.55 ± 0.30 which decayed to baseline with increasing ISI. Next, we measured EPP amplitudes during short trains of five stimuli at 100 Hz (Figure-9A) which show that

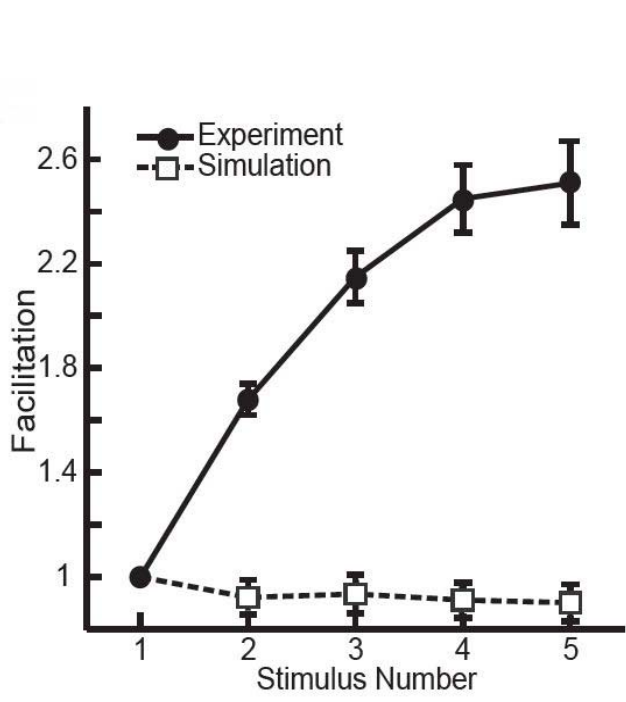
tetanic facilitation at the frog NMJ grew substantially by more than a factor of 2.5 between the first and fifth stimulation event. These data provided insight into the timescales underlying facilitation and furnished important constraints for our modeling studies described below. In particular, we used (iv) the time dependence of PPR as a function of inter-stimulus interval (10 ms to 100 ms), and (v) the growth of tetanic facilitation during a five-pulse stimulus train at 100 Hz as constraints for our model building.

Next, we considered the effect of exogenous Ca^{2+} buffer on facilitation in the frog NMJ active zone (AZ). Experimentally, it is well known that addition of the fast Ca^{2+} buffer BAPTA (1,2-bis(o-aminophenoxy)ethane-N,N,N',N'-tetraacetic acid) reduces both vesicle release and facilitation in the frog NMJ (Tanabe and Kijima, 1992; Naraghi and Neher, 1997; Suzuki et al., 2000; Mukhamedyarov et al., 2009). In contrast, addition of the slow Ca^{2+} buffer EGTA (ethylene glycol tetraacetic acid) to the nerve terminal cytoplasm reduces facilitation but has a much smaller impact on vesicle release at comparable buffer concentrations (Delaney et al., 1991; Meinrenken et al., 2002; Mukhamedyarov et al., 2009). Thus we used as model constraints that: (vi) the addition of BAPTA in our model should both significantly lower the magnitude of vesicle release during a single action potential (by about 70%, see (Tang et al., 2000)) and reduce facilitation; (vii) the addition of EGTA should only slightly reduce the magnitude of vesicle fusion during single action potentials but significantly reduce facilitation. Since experimentally the precise concentration of exogenous buffer in the presynaptic terminal is unknown, in our simulations we considered a range of buffer concentrations (in mM: 0.1, 0.5, 1.0, 2.0) and required that our model complied with (vi) and (viii) as described above. For computational efficiency reasons, we only considered static endogenous and exogenous Ca^{2+} buffer.

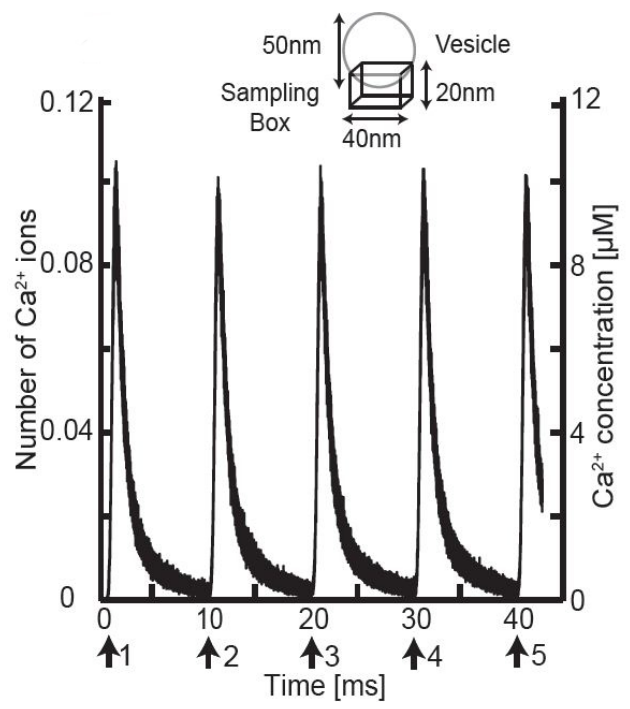
3.3.2 Residual free Ca^{2+} does not generate facilitation

To determine whether our previously developed excess-calcium-binding-site model could account for facilitation, we applied a series of five stimuli at 100 Hz (Dittrich et al., 2013). We found that the model did not generate any short-term facilitation and in fact showed slight depression (Figure-9A) due to the depletion of releasable vesicles during multiple stimuli, as observed in other synapses (Liley and North, 1953; Wu and Borst, 1999; Zucker and Regehr, 2002). Since free Ca^{2+} ions that encountered the edges of our AZ model were removed via absorptive boundary conditions (mimicking the presence of a full sized nerve terminal extension of our single AZ model), there was no significant accumulation of free Ca^{2+} in the terminal, which could have contributed to facilitation (Figure-3.3D). Moreover, when tracking the average number of Ca^{2+} ions within a $3.2 \times 10^4 \text{ nm}^3$ sampling box underneath docked vesicles, we did not observe any localized Ca^{2+} accumulation close to Ca^{2+} sensors on vesicles (Figure-3.3B). In fact, even when the Ca^{2+} ions encountering the edges of our model were not removed from the terminal (by changing absorptive into reflective boundary conditions), and thus accumulated during multiple stimulus events (Figure-3.3E), the limited amount of free Ca^{2+} within the terminal was ineffective in binding to vesicles and thus did not contribute significantly to facilitation (Figure-3.3F). In addition, the synaptotagmin binding kinetics were such that only a small percentage of Ca^{2+} ions that bound during the first stimulus remained bound until subsequent stimuli, and thus contributed very little to subsequent release (Figure-3.3C).

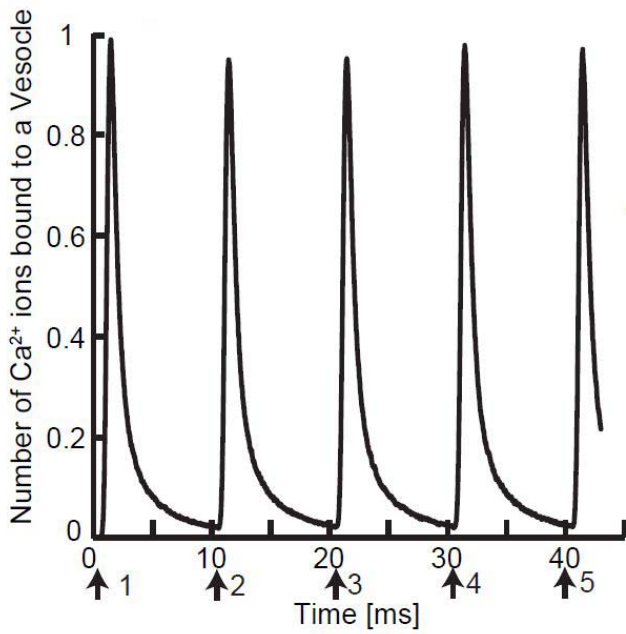
To gain further insight into the mechanistic details of short-term facilitation at the NMJ, we set out to investigate two facilitation mechanisms by making modifications to our previously developed excess-calcium-binding-site model (Dittrich et al., 2013). To guide our modeling efforts, we used the experimental constraints (i)-(vii) listed above.



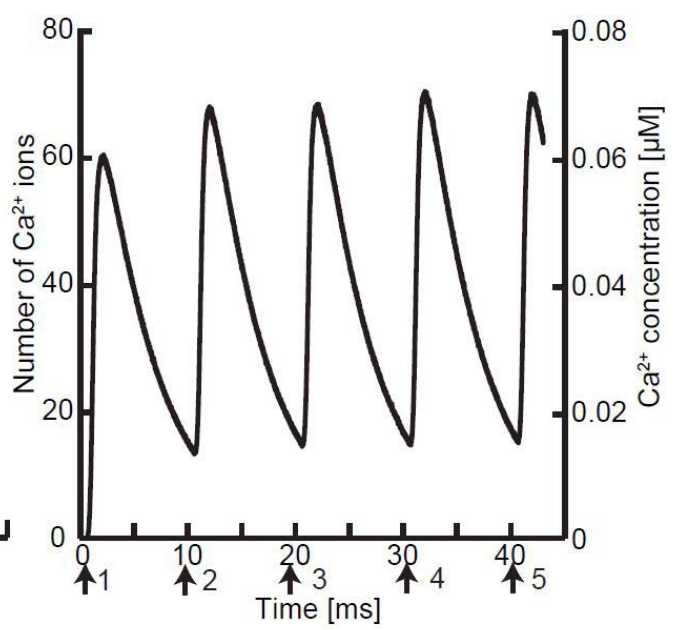
A



B



C



D

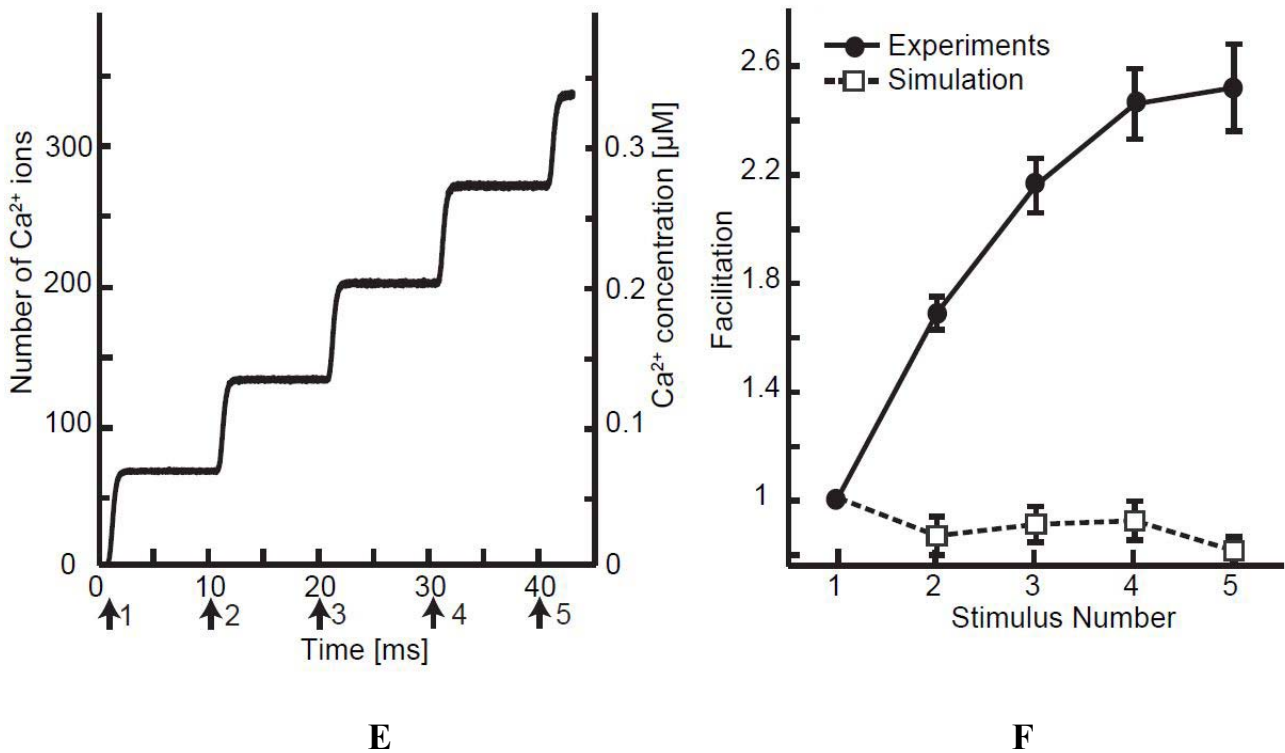


Figure-3.3: Short-term plasticity of excess-binding-site model. **A.** During a stimulus train at 100Hz, experimentally I observe facilitation while the MCell model shows depression. **B.** Average number and concentration of free Ca²⁺ ions in the sampling box underneath released vesicles. The inset illustrates the dimension and location of the sampling box. **C.** Average number of Ca²⁺ ions bound to binding sites on a vesicle. Arrows indicate time points of action potential peaks. **D.** Number and concentration of free Ca²⁺ in the presynaptic terminal with absorptive boundary conditions at the terminal edges. **E.** Number and concentration of free Ca²⁺ in the presynaptic terminal with reflective boundary conditions at the terminal edges. For **B**, **C**, **D**, and **E**, arrows indicate the time points of the action potential peak. **F.** Facilitation in the excess-binding-site-model with reflective boundary conditions.

3.3.3 Facilitation via persistent binding of Ca²⁺ bound synaptotagmin to the presynaptic membrane

The bound residual Ca²⁺ hypothesis posits that vesicular Ca²⁺ binding sites need to be able to hold on to their ions long enough for them to contribute to and enhance subsequent stimuli (Katz and Miledi, 1968; Bertram et al., 1996; Matveev et al., 2006). Since our previous excess-calcium-binding-site model demonstrated that synaptotagmin's binding kinetics for Ca²⁺ did not meet this requirement, we considered a different mechanism based on the association of Ca²⁺ bound synaptotagmin with the lipid bilayer. Recent biochemical evidence suggested that Ca²⁺ bound C2 domains of synaptotagmin penetrate and associate with the lipid membrane, and that this process is vital to exocytosis (Bai et al., 2002; Hui et al., 2006; Paddock et al., 2011). Interestingly, the reported kinetics of the lipid-synaptotagmin interaction in solution features high k_{on} ($10^{10} \text{ M}^{-1}\text{s}^{-1}$) and low k_{off} values (12 s^{-1}) (Hui et al., 2005). This suggests that a high-affinity lipid-bound synaptotagmin state might persist long enough to yield facilitation during high frequency stimulation.

To investigate whether such a protein-lipid association process could underlie facilitation at the frog NMJ, we incorporated this hypothesis into our model. This so-called *persistent binding model* consists of a simple two-state model and is illustrated schematically in Figure-3.4. The model comprised an initial Ca²⁺ binding step to synaptotagmin to yield an active state, followed by lipid association of synaptotagmin to form a longer lasting persistent state. Since we did not know the effective lipid concentration at the presynaptic membrane close to synaptic vesicles we modeled the lipid-synaptotagmin binding process as a simple unimolecular process. Similar to our previous excess-calcium-binding-site model, synaptotagmin became active once two out of its five binding sites bound Ca²⁺ ions according to our previously published binding rate constants (see Table-1) (Dittrich et al.,

2013). Once active, synaptotagmin molecules reversibly entered the persistent state with modeled lipid association rates k_{lipid_on} and k_{lipid_off} . Vesicle release occurred once at least three synaptotagmin molecules were simultaneously in this persistent state.

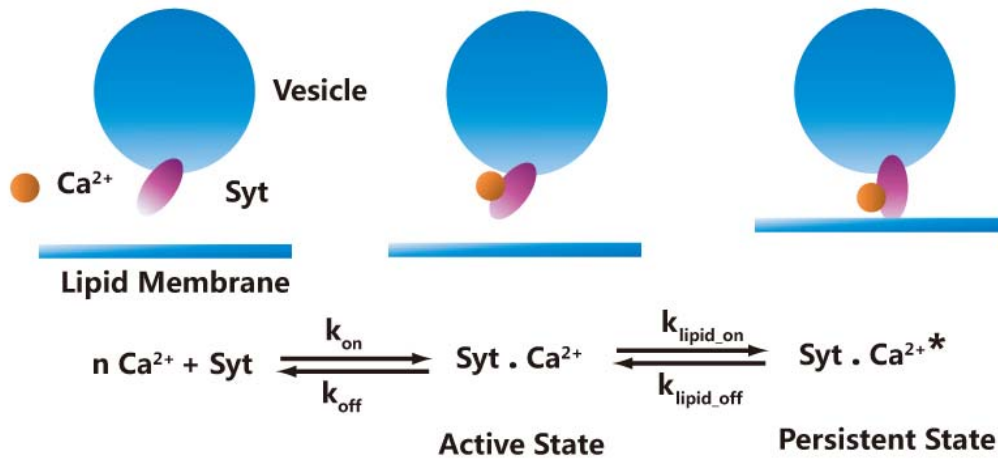


Figure-3.4: Schematic view of the persistent binding model state diagram. The active state corresponds to synaptotagmin with at least two Ca^{2+} ions bound but not interacting with the lipid membrane. The persistent state corresponds to active synaptotagmin interacting with lipid membrane.

To determine values for k_{lipid_on} and k_{lipid_off} that would satisfy our constraints (i)-(vii), we conducted a parameter sweep. As shown in Table-2, increasing k_{lipid_on} while keeping k_{lipid_off} fixed increased vesicle release and reduced paired pulse facilitation (PPF). On the other hand, increasing k_{lipid_off} led to a strong reduction in PPF. Using values for k_{lipid_on} and k_{lipid_off} of $2000 s^{-1}$ and $10 s^{-1}$, respectively, our persistent binding model agreed well with most of our constraints. The number of released vesicles per action potential and AZ during a single stimulus was 0.47 and the histogram of release latencies was narrow and in good agreement with experimental data (Figure-3.5B). The computed CRR was 5.12 (Figure-3.5A) and thus close to – albeit slightly larger than - the

experimentally observed value of 4.2 (Dittrich et al., 2013). Importantly, our persistent binding model showed a significant increase in facilitation in response to a series of stimuli (Figure-3.5A) albeit somewhat slower than observed experimentally. Further, this model also captured the experimentally observed decay in PPF as a function of the interstimulus interval (Figure-3.5D). However, as the interstimulus interval was increased, the PPF of our model decreases less steeply than measured experimentally (Figure-3.5D). Nevertheless, given the simplicity of our persistent binding model, the observed agreement was remarkably good.

$k_{\text{lipid_off}} [\text{s}^{-1}]$	0.2		2		10		20		100		200		2000	
	n_r	PPF	n_r	PPF	n_r	PPF	n_r	PPF	n_r	PPF	n_r	PPF	n_r	PPF
2×10^5	1.95	1.36	1.95	1.36	1.95	1.33	1.92	1.33	1.84	1.17	1.73	1.04	0.81	0.85
2×10^4	1.78	1.38	1.83	1.32	1.78	1.32	1.79	1.31	1.73	1.2	1.67	1.12	1.08	1.06
1×10^4	1.52	1.38	1.5	1.4	1.49	1.43	1.48	1.39	1.48	1.27	1.46	1.16	1	1.07
2×10^3	0.68	1.68	0.6	1.58	0.46	1.48	0.4	1.66	0.41	1.4	0.38	1.24	0.21	1.16

Table-2: Average number of released vesicles (n_r) and PPF for a range of persistent binding site models with different values for $k_{\text{lipid_on}}$ and $k_{\text{lipid_off}}$. Values shown in bold face font best match our experimental constraints.

Our determined value for $k_{\text{lipid_off}}$ (10 s^{-1}), is in good agreement with the experimental data for lipid unbinding by synaptotagmin (12 s^{-1}) (Hui et al., 2005). Since our value for $k_{\text{lipid_on}}$ is an effective rate constant which implicitly contains the (unknown) concentration of lipids at the presynaptic membrane it is not straightforward to compare its value with experimental binding data obtained in the presence of a well defined lipid concentration.

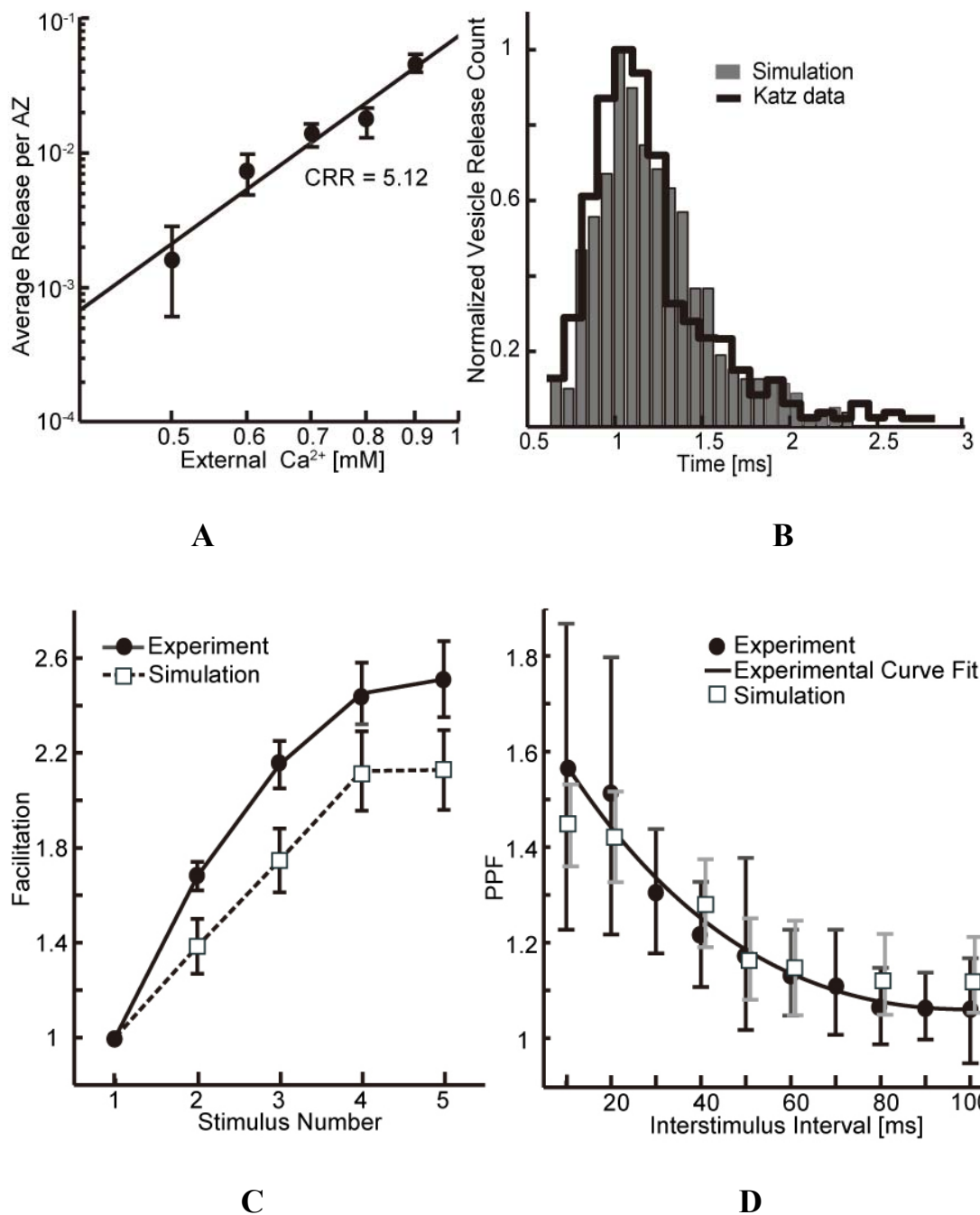


Figure-3.5: Persistent binding site model. **A.** CRR of the persistent binding model. Shown is a log-log plot of average vesicle release versus external $[Ca^{2+}]$ and a linear regression with a slope of 5.12 for the CRR. **B.** Histogram of computed vesicle release latencies in the persistent binding model together with the experimentally measured values from Katz (Katz and Miledi, 1965a). **C.** Experimental and modeled facilitation growth during a 5 pulse train of stimuli at 100 Hz. **D.** Experimental and modeled decay of PPF at different inter-stimulus intervals. The solid line is a double exponential fit to the experimental data.

To investigate the effects of exogenous Ca^{2+} buffer on synaptic transmission in our persistent binding model, we added increasing concentrations of BAPTA and EGTA to our model (in mM: 0.1, 0.5, 1.0, 2.0) in addition to the 2 mM of endogenous buffer. As shown in Figure-3.6A, vesicle release decreased quickly as the BAPTA concentration was increased. In contrast, the PPF remained constant up to 0.5 mM of BAPTA and decreased slowly at higher concentrations. In particular, at a BAPTA concentration of 0.5 mM at which release was reduced by $\sim 70\%$, we did not observe any significant reduction in PPF in our model in contrast to experimental observations (see above). Further, with increasing concentrations of EGTA (Figure-3.6B), our simulations showed a slow decrease in vesicle release and basically unchanged PPF, with exception of the data point at 1 mM EGTA, which exhibited a small, but statistically significant drop in PPF. Thus, while our persistent binding site model showed significant facilitation and also agreed well with most of our previous single pulse constraints, it only exhibited a limited ability to reproduce the experimentally measured effect of exogenous Ca^{2+} buffers BAPTA and EGTA on synapse function. Also, the CRR of our model was slightly higher (5.12) than the one measured experimentally (4.2). We therefore wondered if we could find another extension of our basic excess-calcium-binding site model that would yield facilitation in agreement with all our experimental constraints.

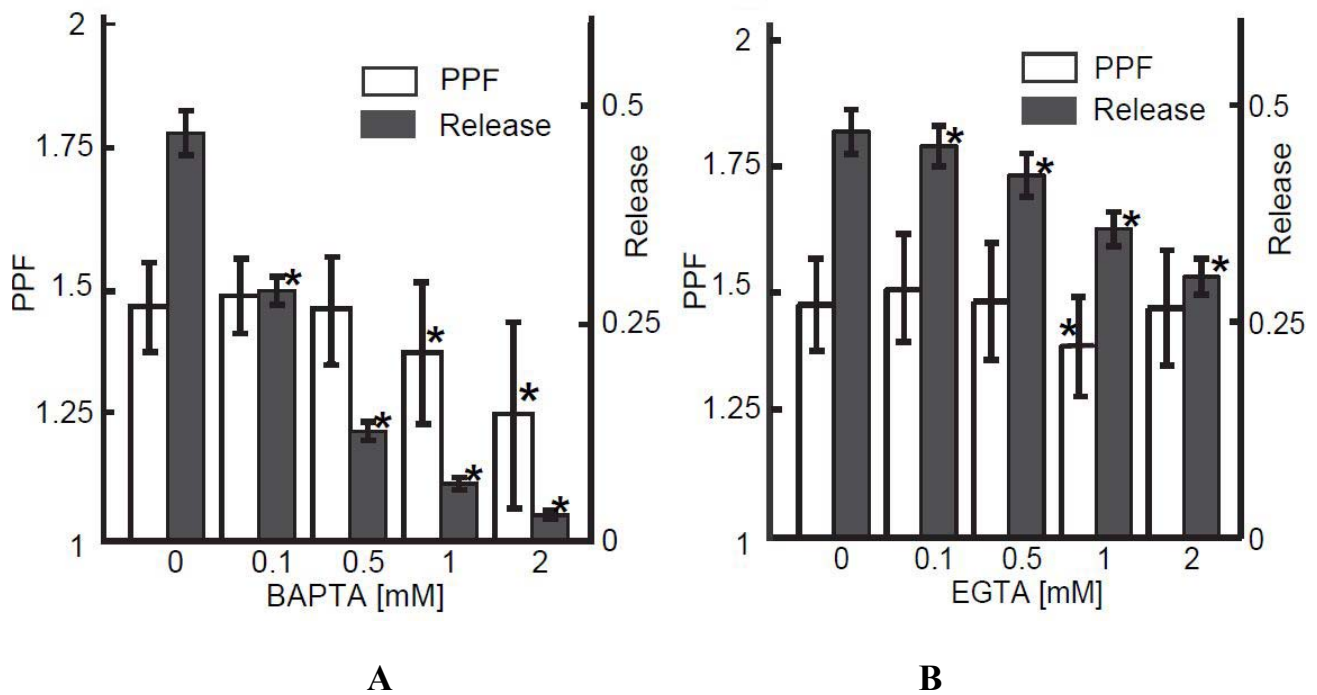


Figure-3.6: Effects of exogenous buffer on persistent binding site model. A. PPF and average vesicle release (n_r) under varying BAPTA concentrations. **B.** PPF and vesicle release (n_r) under varying EGTA concentrations. (*) indicates statistically significant values (one-way ANOVA followed by Tukey's post-hoc test, p -value<0.01).

3.3.4 A model with additional second sensors sites shows facilitation and agrees well with all our constraints

The involvement of multiple, spatially and kinetically distinct Ca^{2+} binding sites that participate in triggering vesicle fusion and facilitation, respectively, has been proposed previously (Yamada and Zucker, 1992; Tang et al., 2000; Bennett et al., 2004; Matveev et al., 2006). However, very little is known about the detailed molecular nature and number of potential second sensor sites involved in facilitation. Thus we wondered if, based on our excess-calcium-binding-site model, we could both

confirm the viability of this mechanism and also shed light on its molecular nature. To this end, we added to each vesicle a second set of binding sites (Y sites) (Tang et al., 2000) in addition to the 40 existing sites on synaptotagmin. The newly introduced Y binding sites were placed in an annular region on the bottom of synaptic vesicles directly above the synaptotagmin sites (Figure-13). The Ca^{2+} binding kinetics of the second sensor sites were modeled based on literature values for the crayfish NMJ, $k_{\text{on}_Y} = 6 \times 10^6 \text{ M}^{-1} \text{ s}^{-1}$, $k_{\text{off}_Y} = 36 \text{ s}^{-1}$ (Matveev et al., 2006). Compared to synaptotagmin, the second sensor sites had a higher Ca^{2+} binding affinity and featured slower Ca^{2+} unbinding kinetics with a dwell time of ~ 30 ms. In particular, in our model we had $k_{\text{on_BAPTA}} > k_{\text{on_syt}} > k_{\text{on}_Y}$, and $k_{\text{on_syt}} > k_{\text{on_EGTA}} > k_{\text{on}_Y}$ (Table-1).

We then proceeded to determine viable numbers of second sensor sites, n_Y , on synaptic vesicles, as well as a vesicle *fusion mechanism*. Here, a fusion mechanism specifies the manner in which synaptotagmin and second sensor sites had to bind Ca^{2+} for vesicle fusion to be triggered. The initial fusion mechanism we chose was a straightforward extension of the one used in our previous excess-calcium-binding-site model. A synaptotagmin molecule was activated once at least two of its five Ca^{2+} binding sites were simultaneously occupied by at least two Ca^{2+} ions. Similarly, second sensor sites were activated as soon as they bound a single Ca^{2+} ion. Vesicles were released once a total of N synaptotagmin and/or second sensor sites were active simultaneously. In particular, both types of Ca^{2+} binding sites could in principle contribute to fusion and facilitation and their fractional contribution to either process was mainly determined by their Ca^{2+} binding and unbinding kinetics.

To determine a viable fusion mechanism we needed to determine both n_Y and N . We simulated a range of models with different numbers of second sensor sites, n_Y , and values for N (see Table-3). Similar to our previous study (Dittrich et al., 2013) we considered synaptotagmin models with two

different k_{on} values ($k_{on} = 1 \times 10^8 \text{ M}^{-1}\text{s}^{-1}$ and $4 \times 10^8 \text{ M}^{-1}\text{s}^{-1}$). Initially, we focused on models which could reproduce the average number of released vesicles per AZ and action potential as well as the PPF using a 10 ms interstimulus interval. As shown in Table-3, for a given number of second sensor sites, an increase in N led to a decrease in the number of released vesicles and a corresponding increase in the PPF. On the other hand, for fixed values of N , an increase in n_Y led to a steep increase in the number of released vesicles while leaving the PPF largely unaffected. This nicely illustrates the interplay between the number of available second sensor sites and the required number of active sites N . As N was increased, synaptotagmin and Y sites continued to be activated but fewer vesicles were released during the first pulse leading to increased release during the second pulse thus enhancing the PPF. For fixed N , an increase in n_Y enhanced the number of activated second sensor sites, increasing both the initial release magnitude as well as the PPF.

Table-3 shows that a model with a moderate number of second sensor sites, $n_Y = 28$ (Figur-3.7), and $N = 4$ fit our initial constraints well and also exhibited the proper narrow distribution of release latencies (Figure-3.8A). In addition, this 28-Y-site-model showed significant tetanic facilitation during a train of stimuli albeit at a somewhat lower rate than what we measured experimentally (Figure-3.8B). Similarly, our model simulations showed the expected relationship between PPF and ISI, however, PPF decayed at a slightly steeper rate as the ISI was increased as compared to our experimental observations (Figure-3.8C). Further, the computed CRR of 5.16 was slightly higher than the experimentally observed value of 4.2 (Figure-3.8D). When examining the model's response to exogenous buffer we found that adding BAPTA significantly reduced the magnitude of vesicle fusion during a single action potential (Figure-3.8E) and also lowered PPF significantly (e.g. using our 70% criterion for block of initial vesicle fusion, PPF was reduced by 70%). Furthermore, adding EGTA to the model only moderately (compared to BAPTA) reduced the magnitude of vesicle fusion and significantly decreased

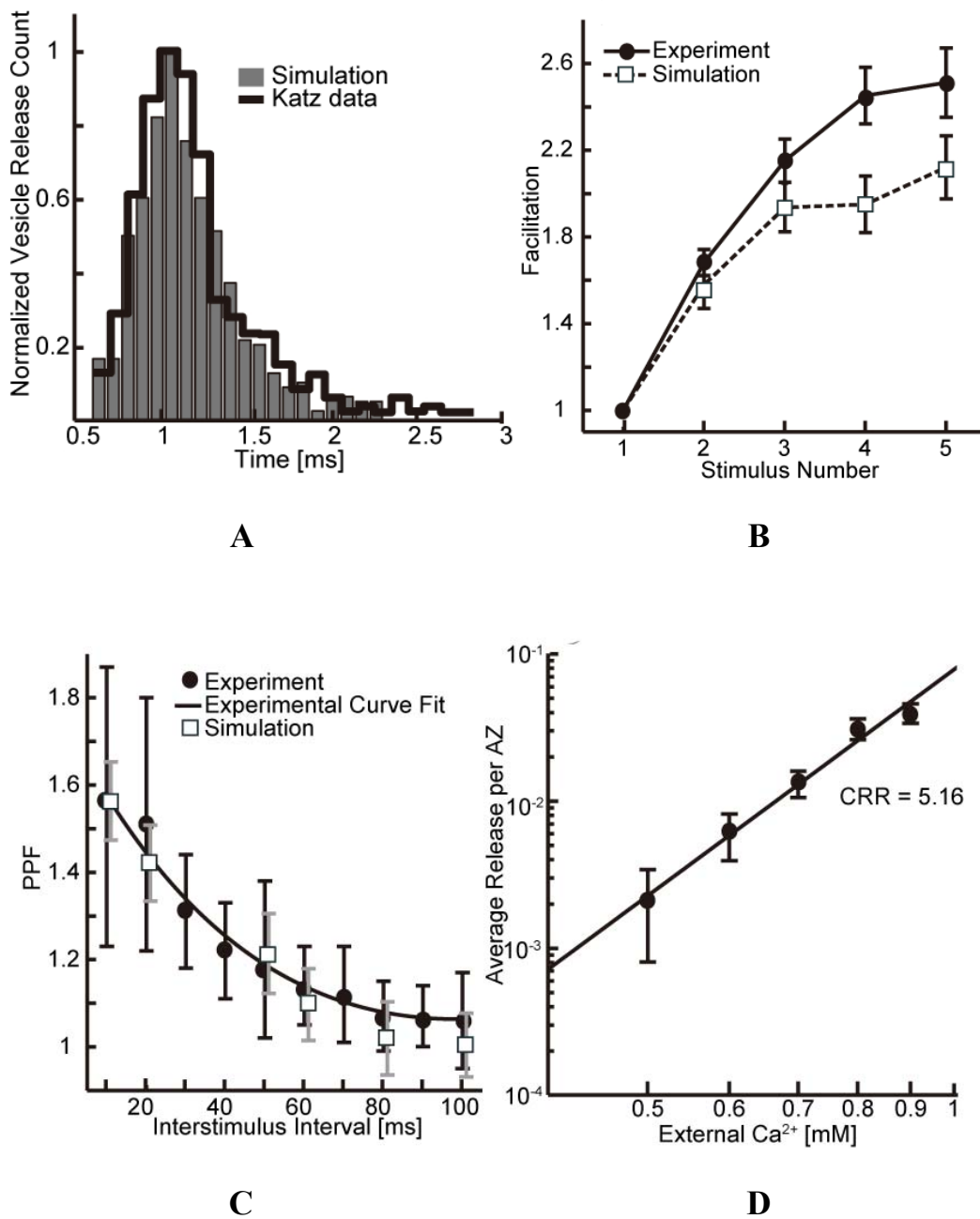
PPF (Figure-3.8F). These results suggested that the 28-Y-site-model satisfied most experimental constraints, with the exception of the slightly elevated value for the CRR. In particular, the introduction of second sensor sites greatly enhanced the model's sensitivity to exogenous Ca^{2+} buffer. While this finding was quite satisfactory we wondered if we could improve the model further to decrease its sensitivity toward external Ca^{2+} and thus lower the value of the CRR.



Figure-3.7: Schematic view of the bottom of a synaptic vesicle showing the 28 Y binding sites (small black colored triangles forming a ring around the synaptotagmin molecules). The arrangement of synaptotagmin molecules is identical to our original excess-calcium-binding-site model (Figure-3.2). The depicted vesicle is considered released according to a release mechanism with $N=4$ since three synaptotagmin and one second sensor (Y) site are active.

N_Y	$k_{on}[M^{-1}s^{-1}]$	N=3		N=4		N=5	
		N_s	PPF	N_s	PPF	N_s	PPF
16	1×10^8	1.0	1.24	0.2	1.59	0.1	1.82
28	1×10^8	1.4	1.48	0.5	1.57	0.2	2.21
68	1×10^8	2.8	1.23	1.4	1.62	0.7	1.93
144	1×10^8	3.7	1.19	3.2	1.36	1.9	1.75
16	4×10^8	1.9	1.18	0.6	1.33	0.2	1.66
28	4×10^8	2.5	1.21	1.0	1.48	0.3	1.68
68	4×10^8	4.0	1.22	2.1	1.54	1.0	1.86

Table-3: Average number of released vesicles (\bar{n}) and PPF for a range of second sensor models for different choices of parameters: Y binding site number (N_Y), k_{on} for synaptotagmin, and the total number of active synaptotagmin and Y binding sites required to trigger fusion (N). Values shown in bold face font best match our experimental constraints.



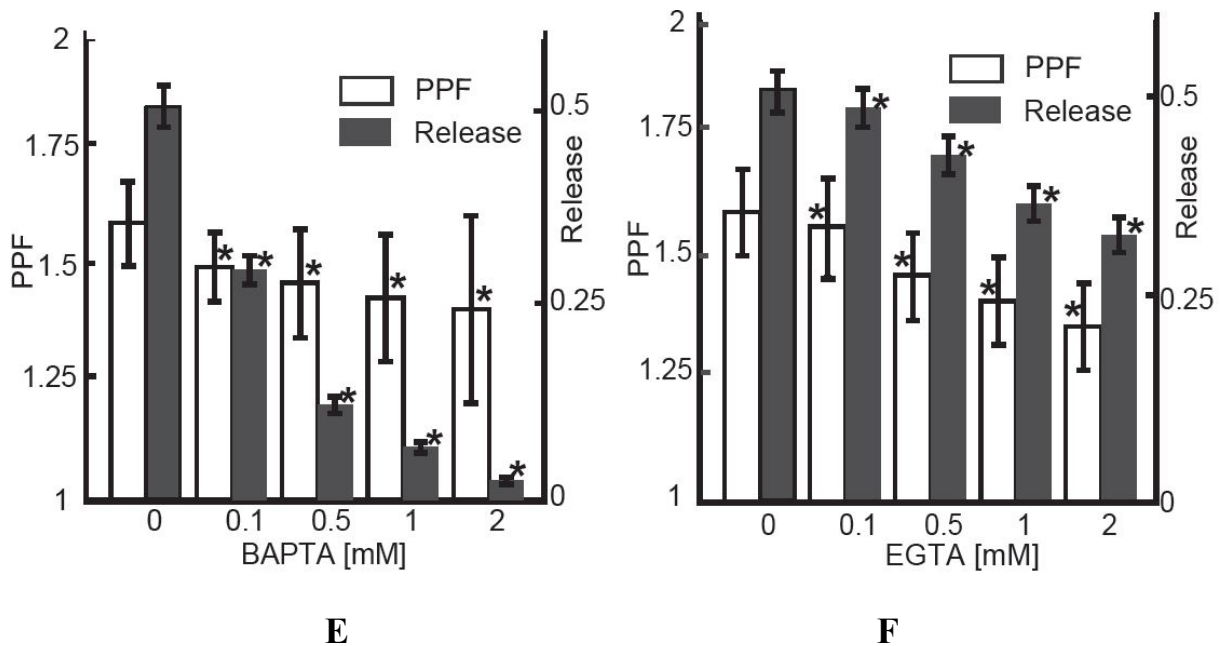


Figure-3.8: 28-Y-site model. A. Histogram of computed vesicle release latencies in the 28-Y-site model together with the experimentally measured values from Katz (Katz and Miledi, 1965a). **B, C,** and **D.** show facilitation growth, PPF decay, and CRR predicted by the 28 Y site model (c.f. Figure 2 for notational details). **E,** **F.** depict the effects of different concentrations of exogenous buffer BAPTA and EGTA on PPF and average vesicle release (n_r). (*) indicates statistically significant values (one-way ANOVA followed by Tukey’s post-hoc test, p-value < 0.01).

3.3.5 Second sensor model with energy based fusion mechanism further improves agreement with experimental constraints

Previous studies have suggested that to initiate fusion with the plasma membrane, the vesicle membrane needs to overcome an energy barrier of roughly $40 k_B T$ (Li et al., 2007a; Martens et al., 2007). Further, Ca^{2+} bound synaptotagmin has been hypothesized to contribute to lowering this energy barrier (Martens et al., 2007; Malsam et al., 2008; Sørensen, 2009; Wiederhold and Fasshauer, 2009;

Young and Neher, 2009; Gao et al., 2012). Our second-sensor model introduced above assumed that activated synaptotagmin and second sensor sites contributed equally to vesicle fusion. However, since the second sensor sites are assumed to be biochemically distinct from synaptotagmin, and also occupy spatially distinct locations on vesicles, we hypothesized that active synaptotagmin and second sensor sites might contribute differently to vesicle fusion. In particular, in our energy based fusion mechanism we hypothesized that activated synaptotagmin and second sensor sites each lowered the fusion barrier by increments ΔE_S and ΔE_Y . To determine if and when a particular vesicle fusion event occurred during a given simulation run, we computed the time series of total energies for all instantaneously active synaptotagmin (ΔE_S) and second sensor (ΔE_Y) sites and then used the Metropolis-Hastings algorithm (Metropolis et al., 1953; Hasting, 1970) to decide if vesicle fusion took place or not (Figure-3.9).

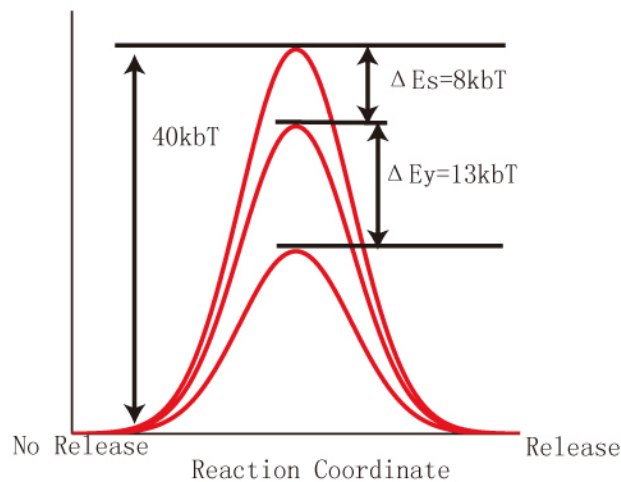


Figure-3.9: Illustration of energy sampling. Activation of synaptotagmin and second sensor sites after Ca^{2+} binding lowers the fusion energy barrier ($40 \text{ k}_B\text{T}$). Shown is the barrier reduction for a model with $\Delta E_S = 8 \text{ k}_B\text{T}$ and $\Delta E_Y = 13 \text{ k}_B\text{T}$.

We first considered a 28-Y-site-energy-model (described above) in which both synaptotagmin and second sensor sites contributed equally to vesicle fusion ($\Delta E_S = \Delta E_Y = 10 \text{ k}_B\text{T}$). This model

corresponded closely to our previous 28-Y-site-model with $N=4$, with the exception that due to the Metropolis sampling, release was now possible even for an occupancy of less than four, albeit with low probability. As shown in Table-4, the results for both models were very similar, as one would have expected. In particular, the CRR of the 28-Y-site-energy-model was 5.14 and thus still larger than our experimental constraints (4.2).

We next turned to models with lower (8, 12, and 16) and higher (68 and 144) numbers of second sensor sites over a range of values for both ΔE_S and ΔE_Y . Similar to our earlier approach, we initially selected models based on two experimental constraints: the average number of released vesicles per AZ and action potential, and the PPF with a 10 ms interstimulus interval. The simulation results are shown in Table-4 and several general trends are apparent. Overall, the number of fused vesicles per action potential and AZ increased as either ΔE_S or ΔE_Y were increased. On the other hand, an increase in ΔE_S or ΔE_Y led to a decrease in PPF with the latter being significantly more sensitive to changes in ΔE_S compared to ΔE_Y . As shown in Table 4, several models provided good agreement based on average number of fusion events and PPF. In particular, using $k_{on} = 1 \times 10^8 \text{ M}^{-1}\text{s}^{-1}$ for synaptotagmin's Ca^{2+} binding sites, models with $n_Y = 16$ ($\Delta E_S/\Delta E_Y = 10/14 \text{ k}_B\text{T}$) (Figure-3.10A and B), $n_Y = 28$ ($\Delta E_S/\Delta E_Y = 10/9 \text{ k}_B\text{T}$; $\Delta E_S/\Delta E_Y = 10/10 \text{ k}_B\text{T}$), and $n_Y = 68$ ($\Delta E_S/\Delta E_Y = 10/5 \text{ k}_B\text{T}$) fit our two initial constraints (Figure-3.10C and D, see also Figure-3.12). On the other hand, for models with $n_Y = 8, 12$ and 144 binding sites, we could not find suitable ΔE_S and ΔE_Y values which led to agreement with our experimental constraints. We also examined models with a synaptotagmin k_{on} value of $4 \times 10^8 \text{ M}^{-1}\text{s}^{-1}$. Here again, models with $n_Y = 16$ ($\Delta E_S/\Delta E_Y = 8/13 \text{ k}_B\text{T}$; $\Delta E_S/\Delta E_Y = 9/12 \text{ k}_B\text{T}$; $\Delta E_S/\Delta E_Y = 9/13 \text{ k}_B\text{T}$), $n_Y = 28$ ($\Delta E_S/\Delta E_Y = 9/8 \text{ k}_B\text{T}$), and $n_Y = 68$ ($\Delta E_S/\Delta E_Y = 9/4 \text{ k}_B\text{T}$), provided good agreement with our two initial experimental constraints. Interestingly, when including the CRR as a constraint, only the 16-Y-site-energy-model with $k_{on} = 4 \times 10^8 \text{ M}^{-1}\text{s}^{-1}$ for synaptotagmin and $\Delta E_S/\Delta E_Y = 8/13 \text{ k}_B\text{T}$ provided a good match

with a CRR value of 4.60 (Figure-3.11C). This model also satisfied all of our additional constraints, namely, the narrow vesicle release latency (Figure-3.11D), experimentally observed tetanic facilitation (Figure-3.11A), and PPF decay as ISI was increased (Figure-3.11B). Similar to our 28-Y-site-model above, the tetanic facilitation magnitude was slightly lower compared to our experimental measurements, and the PPF decayed more rapid as the ISI was increased. The 16-Y-site-energy-model also showed the expected sensitivity toward addition of exogenous Ca^{2+} buffer (Figure-3.11E and F): addition of BAPTA reduced vesicles release rapidly (Figure-3.11E) and also lowered PPF significantly (e.g. using our 70% criterion for block of vesicle fusion during a single action potential). Similarly, addition of EGTA only moderately reduced vesicle release (compared to BAPTA) and PPF (Figure-3.11F).

Thus, among all models examined here, the 16-Y-site-energy-model with $k_{\text{on}} = 4 \times 10^8 \text{ M}^{-1} \text{ s}^{-1}$ for Ca^{2+} binding sites on synaptotagmin and energy contributions $\Delta E_S / \Delta E_Y = 8/13 \text{ k}_B\text{T}$ toward overcoming the energy barrier for vesicle fusion matched our experimental constraints best. Together with the 28-Y-site-model above, our results indicate that within the context of a second sensor model, the number of Y binding sites may be on the order of the number of available synaptotagmin Ca^{2+} binding sites or less. Table-5 summarizes the main properties of all viable models examined in this study.

$N_Y=8, k_{on}=1 \times 10^8 M^{-1} s^{-1}$					$N_Y=12, k_{on}=1 \times 10^8 M^{-1} s^{-1}$					$N_Y=16, k_{on}=1 \times 10^8 M^{-1} s^{-1}$				
ΔE_s	ΔE_y	n_r	PPF	CRR	ΔE_s	ΔE_y	n_r	PPF	CRR	ΔE_s	ΔE_y	n_r	PPF	CRR
9	14	0.17	1.63	N/A	9	14	0.27	1.63	N/A	7	13	0.18	2.10	3.59
9	15	0.19	1.52	N/A	9	15	0.29	1.60	N/A	8	13	0.28	1.76	3.38
10	15	0.25	1.52	N/A	10	14	0.35	1.55	N/A	9	13	0.36	1.64	2.89
10	16	0.33	1.42	N/A	10	15	0.42	1.47	N/A	9	14	0.41	1.69	2.64
11	14	0.35	1.39	N/A	10	16	0.51	1.40	N/A	9	15	0.50	1.57	2.75
11	15	0.38	1.37	N/A	11	14	0.49	1.41	N/A	9	16	0.59	1.48	2.68
12	14	0.55	1.28	N/A	11	15	0.54	1.38	N/A	10	13	0.46	1.60	2.82
12	15	0.56	1.25	N/A						10	14	0.54	1.66	2.80
$N_Y=28, k_{on}=1 \times 10^8 M^{-1} s^{-1}$					$N_Y=68, k_{on}=1 \times 10^8 M^{-1} s^{-1}$					$N_Y=144, k_{on}=1 \times 10^8 M^{-1} s^{-1}$				
ΔE_s	ΔE_y	n_r	PPF	CRR	ΔE_s	ΔE_y	n_r	PPF	CRR	ΔE_s	ΔE_y	n_r	PPF	CRR
10	10	0.50	1.57	5.14	10	4	0.36	1.58	5.39	10	1	0.15	1.41	N/A
10	9	0.47	1.66	5.64	10	5	0.49	1.68	5.29	10	2	0.31	1.56	N/A
10	8	0.40	1.54	5.87	10	6	0.65	1.76	4.23	10	3	0.51	1.85	N/A
9	9	0.38	1.67	5.56						10	4	0.83	1.99	N/A
9	8	0.25	1.66	5.97						10	5	1.18	1.98	N/A
$N_Y=16, k_{on}=4 \times 10^8 M^{-1} s^{-1}$					$N_Y=28, k_{on}=4 \times 10^8 M^{-1} s^{-1}$					$N_Y=68, k_{on}=4 \times 10^8 M^{-1} s^{-1}$				
ΔE_s	ΔE_y	n_r	PPF	CRR	ΔE_s	ΔE_y	n_r	PPF	CRR	ΔE_s	ΔE_y	n_r	PPF	CRR
7	15	0.45	1.86	3.17	9	8	0.47	1.52	5.79	8	4	0.32	1.66	6.76
8	13	0.45	1.63	4.60	9	9	0.62	1.59	5.20	8	5	0.45	1.86	5.20
8	14	0.51	1.75	3.89	10	8	0.81	1.38	5.97	9	4	0.48	1.58	5.16
8	15	0.59	1.74	3.20	10	9	0.93	1.46	4.35	9	5	0.65	1.67	4.83
9	12	0.51	1.51	4.46						10	5	0.83	1.55	4.58
9	13	0.54	1.65	3.77										
9	14	0.62	1.69	3.56										
9	15	0.64	1.71	3.39										

Table-4: Average number of released vesicles (n_r), PPF, and CRR for a range of second sensor energy models for different choices of parameters: Y binding site number (N_Y), k_{on} of synaptotagmin, and the energy contributions toward fusion for active synaptotagmin (ΔE_s) and second sensor sites (ΔE_y). Values shown in bold face font best match our experimental constraints.

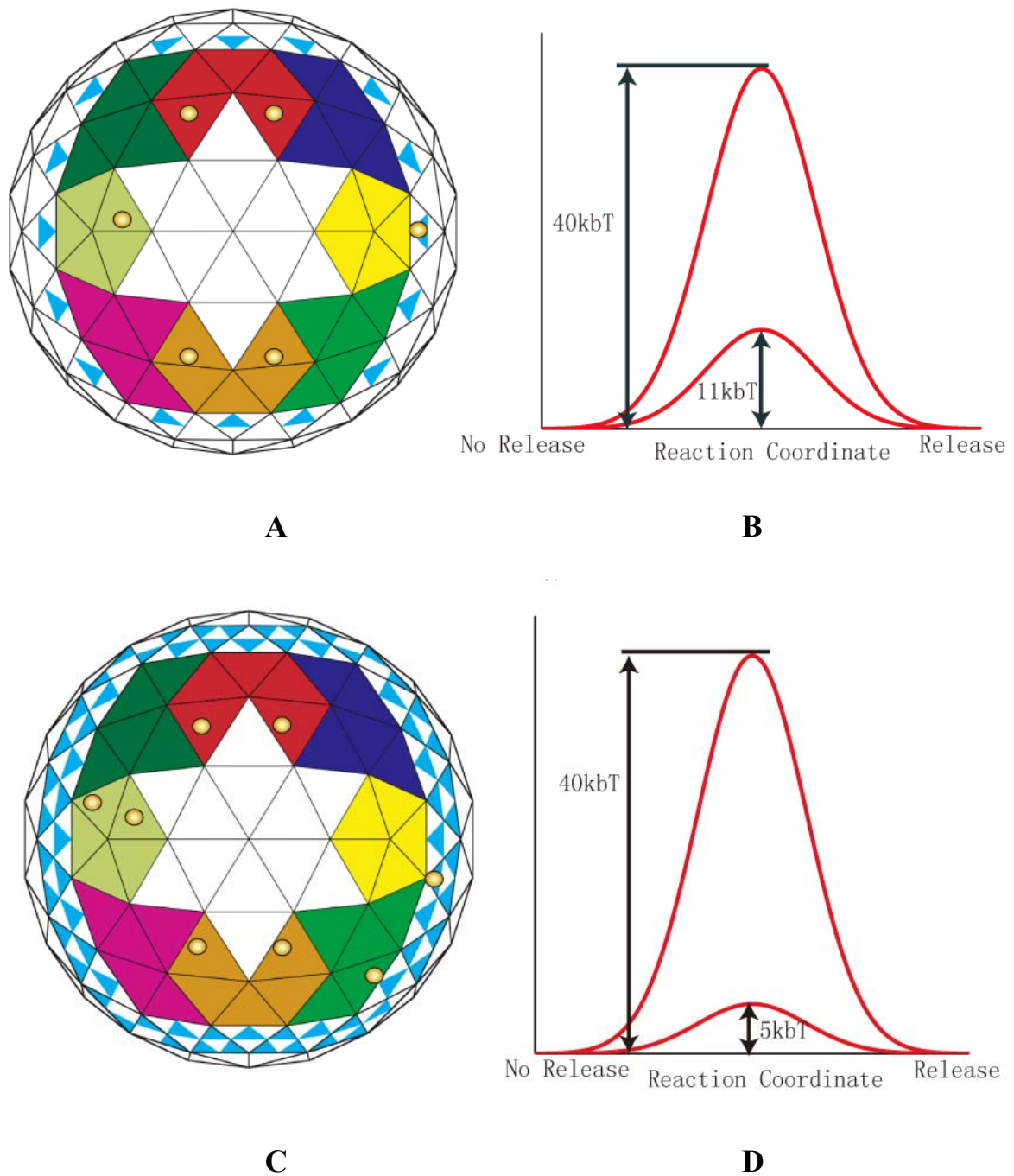
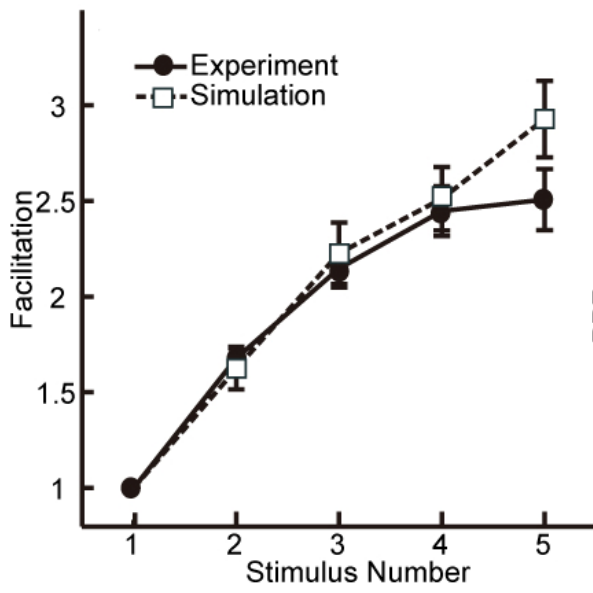
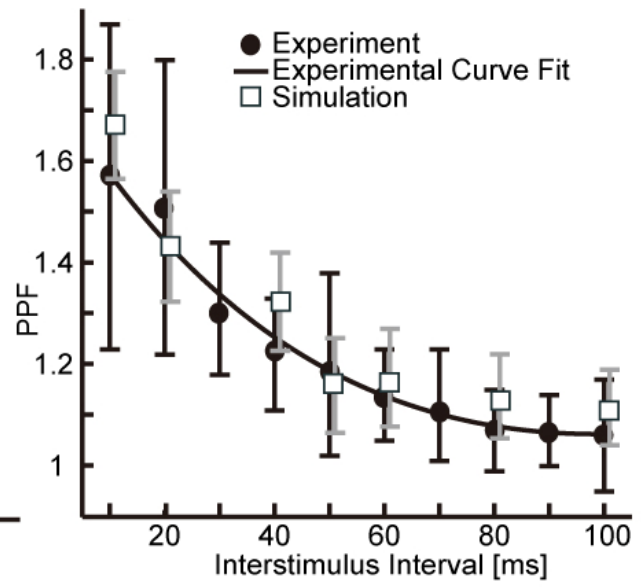


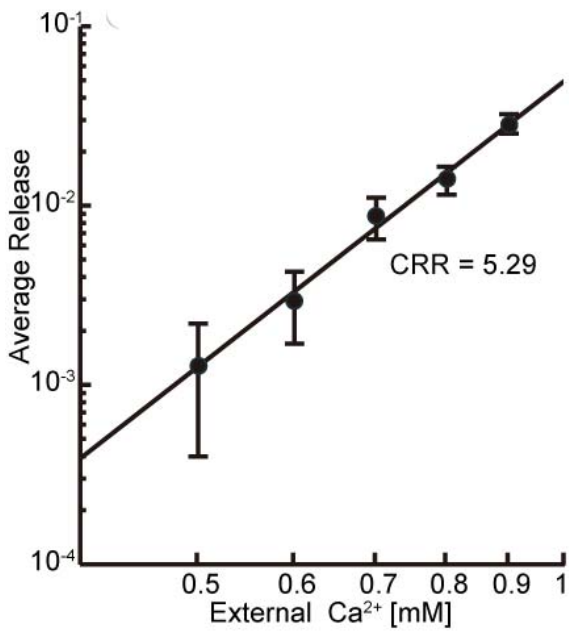
Figure-3.10: Schematic view of the bottom of a synaptic vesicle showing the 16 and 68 Y binding sites. A. Arrangement of synaptotagmin (sets of 5 gray triangles) and second sensor (small black triangles) Ca^{2+} binding sites on a 16-Y-site-energy model. The vesicle shown here has two active synaptotagmin and one active second sensor (Y) site. **B.** Fusion energy barrier for 16-Y-site-energy model with $\Delta E_s=8 \text{ k}_B\text{T}$ and $\Delta E_Y=13 \text{ k}_B\text{T}$ is reduced to $11 \text{ k}_B\text{T}$. **C.** Arrangement of synaptotagmin and Y sites in a 68-Y-site-energy model. Vesicle shown has two active synaptotagmin and three active second sensor (Y) sites. **D.** Fusion energy barrier for 68-Y-site-energy model with $\Delta E_s=10 \text{ k}_B\text{T}$ and $\Delta E_Y=5 \text{ k}_B\text{T}$ is reduced to $5 \text{ k}_B\text{T}$.



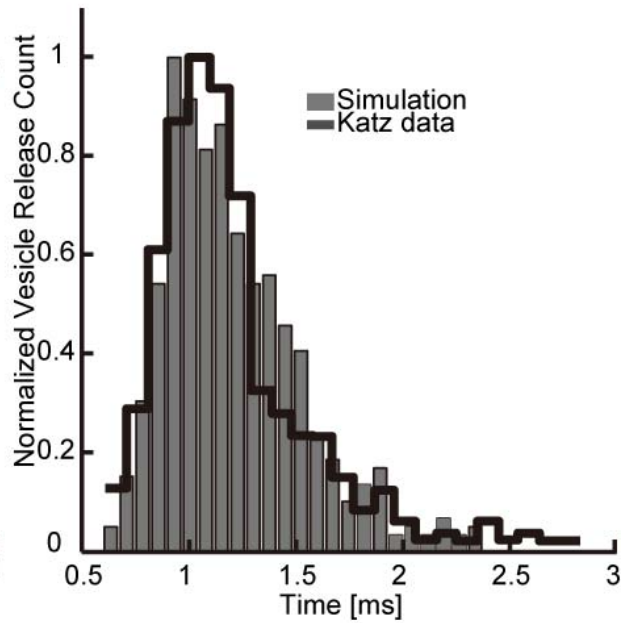
A



B



C



D

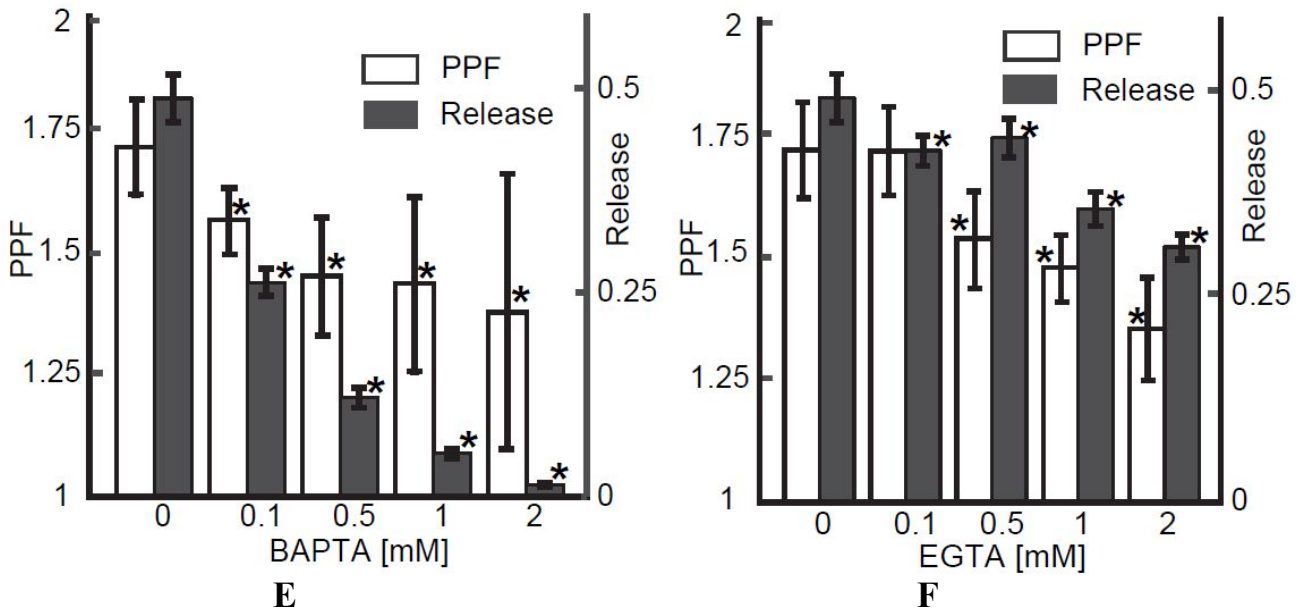
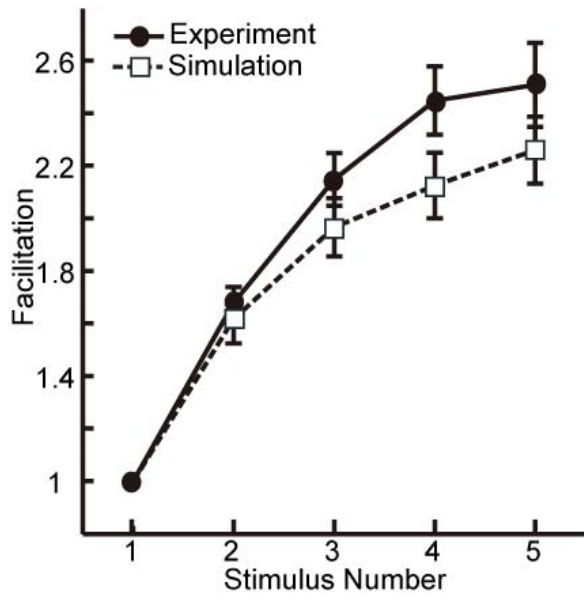


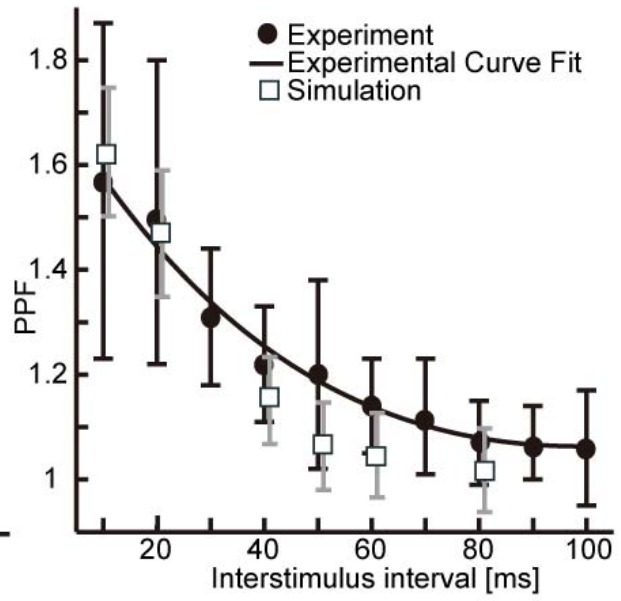
Figure-3.11: Summary of 68-Y-site-energy model. A. Facilitation growth, **B.** PPF decay, **C.** CRR, and **D.** histogram of vesicle release latencies predicted by this model. **E,** **F.** depict the effects of different concentrations of exogenous buffer BAPTA and EGTA on PPF and average vesicle release (n_r). (*) indicates statistically significant values (one-way ANOVA followed by Tukey's post-hoc test, p -value < 0.01).

Model	ΔE_s	ΔE_Y	$k_{on} [M^{-1}s^{-1}]$	n_r	PPF	CRR
<i>Persistent Binding Site Model</i>	N/A	N/A	1×10^8	0.47	1.45	5.12
28-Y-site-model	N/A	N/A	1×10^8	0.51	1.56	5.16
28-Y-site-energy-model	10 $k_B T$	10 $k_B T$	1×10^8	0.51	1.58	5.14
68-Y-site-energy-model	10 $k_B T$	5 $k_B T$	1×10^8	0.49	1.67	5.29
16-Y-site-energy-model	9 $k_B T$	15 $k_B T$	1×10^8	0.51	1.57	2.75
16-Y-site-energy-model	8 $k_B T$	13 $k_B T$	4×10^8	0.45	1.63	4.60

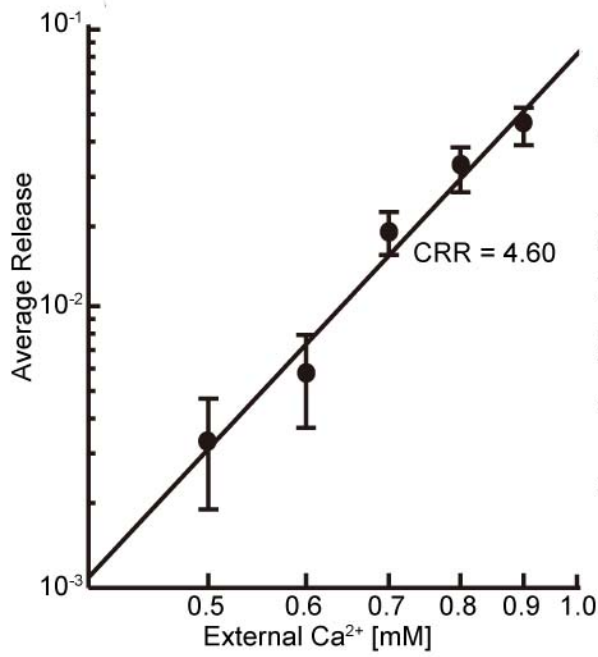
Table-5: Comparison of models matching our experimental n_r and PPF (k_{on} , Ca^{2+} on-rate of synaptotagmin; n_r , average number of released vesicles).



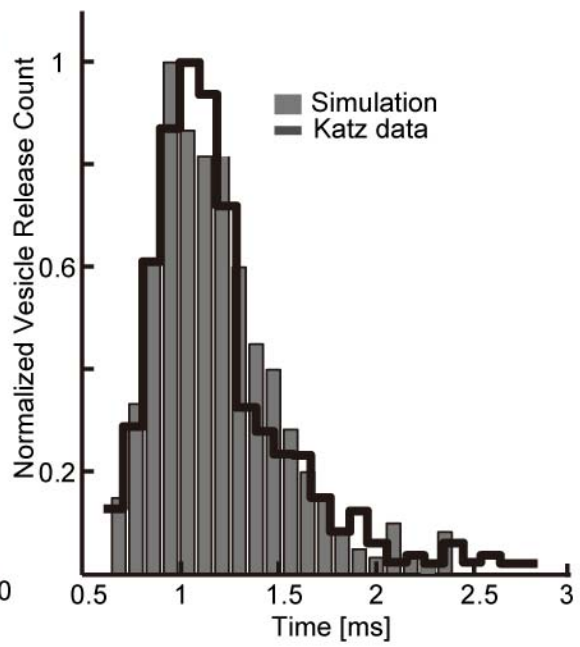
A



B



C



D

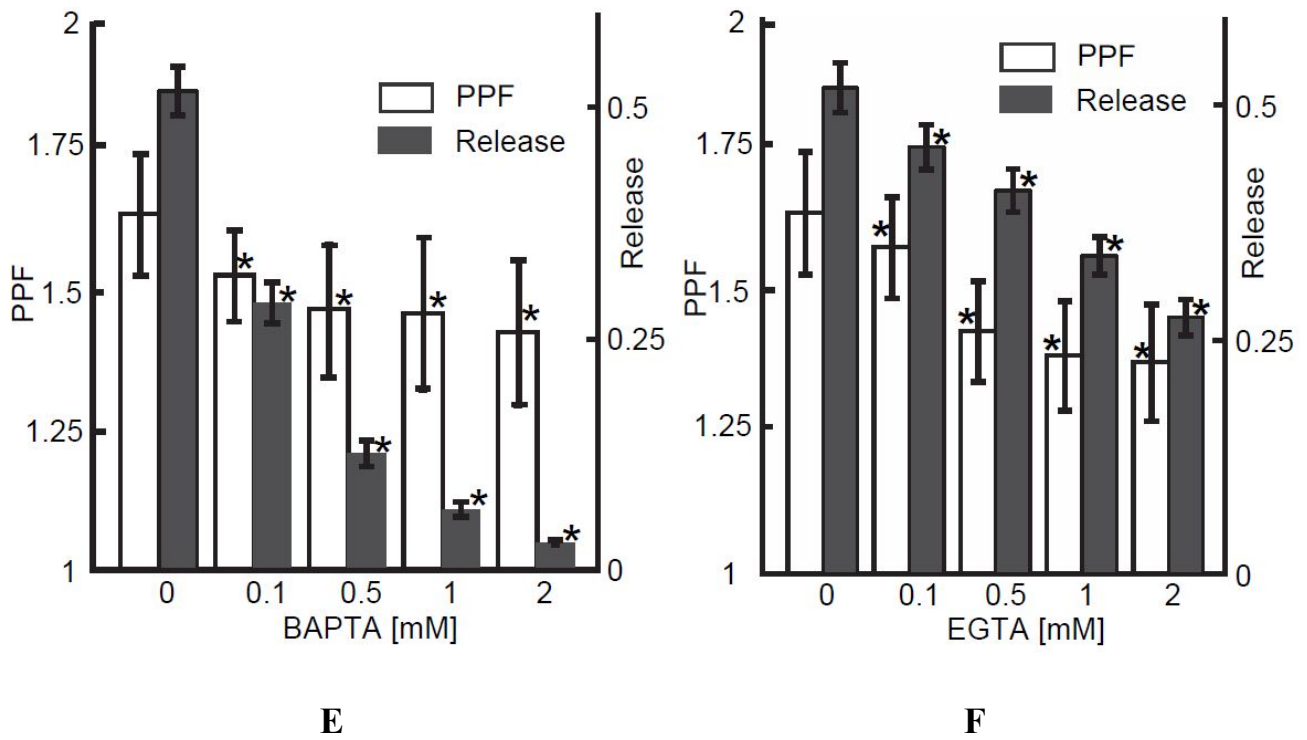


Figure-3.12: Summary of the 16-Y-site-energy-model with $k_{on}=4\times 10^8 \text{ M}^{-1}\text{s}^{-1}$ for synaptotagmin. A. Facilitation growth, B. PPF decay, C. CRR, and D. histogram of vesicle release latencies predicted by this model (c.f. Figure 2 for notational details). E, F. depict the effects of different concentrations of exogenous buffer BAPTA and EGTA on PPF and average vesicle release (n_r). (*) indicates statistically significant values (one-way ANOVA followed by Tukey's post-hoc test, p-value<0.01).

3.3.6 Facilitation is enhanced under low external calcium conditions

With our second sensor model in hand, we wondered how variations in the external Ca^{2+} concentration would affect PPF within our models. We reduced the external Ca^{2+} concentration in our 16-Y-site-energy-model and then determined the PPF in each case. The results are depicted in Figure-3.13 and show that PPF increases significantly as the external Ca^{2+} concentration is lowered. A similar behavior was observed in earlier studies using experimental and computational methods (Magleby and Zengel, 1982; Holohean and Magleby, 2011). Fundamentally, this is due to a dramatic decrease in

initial vesicle fusion under low Ca^{2+} conditions during the first stimulus, and correspondingly enhanced release during the second and subsequent pulses due to the effects of residual Ca^{2+} .

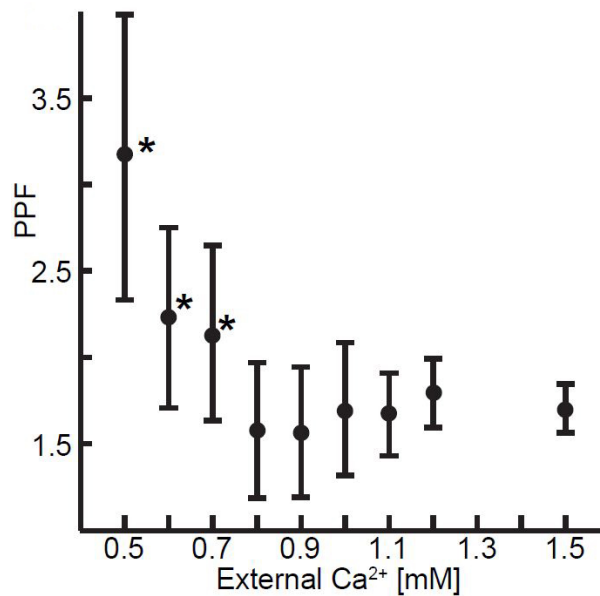


Figure-3.13: PPF as a function of external $[\text{Ca}^{2+}]$ shows an increase in PPF as $[\text{Ca}^{2+}]$ is decreased. (*) indicate values statistically significant from 1.5 mM (one-way ANOVA followed by Tukey's post-hoc test, p-value<0.01).

3.3.7 Nanodomain coupling of VGCCs to synaptic vesicles persists during repeated stimuli

Due to the particle-based nature of our MCell simulations we were able to track which and how many VGCCs contributed to the release of individual vesicles during repeated stimulation. To this end, Figure-3.14 depicts the fractional contribution of different numbers of Ca^{2+} channels to the release of individual synaptic vesicles during a five-pulse tetanic stimulation event using our 16-Y-site-energy-model. As we observed previously (Dittrich et al., 2013), during the first stimulus the majority of vesicle release events were triggered by Ca^{2+} ions from a single (29%) or two (44%) VGCCs, and only

a smaller fraction (27%) were derived from three channels or more. No release events were triggered by more than five channels. On average, 2.06 channels contributed to each vesicle fusion event during the first stimulus, in agreement with our previous results (Dittrich et al., 2013) and values reported in the literature (Shahrezaei et al., 2006). This suggests that at the frog NMJ only a small number of nearby channels are responsible for vesicle release in a nanodomain fashion (Tarr et al., 2013). During repeated stimulation, the number of channels contributing to vesicle fusion increased as shown in Figure-3.14. For example, the fraction of vesicles triggered to fuse by Ca^{2+} from only one or two VGCCs dropped from 73% during the first pulse to 44% during stimulus number five. Correspondingly, the contribution to fusion of three or more channels grew from 27% in the first stimulus to 56% during the fifth stimulus. Therefore, on average, more VGCCs contributed to vesicle release during later stimuli in the train (from 2.06 during the first stimulus to 2.69 during the fifth). However, this increase was mainly due to more complete sampling of available nearby channels during repeated stimuli as opposed to recruitment of more distant channels. Thus, vesicle release continued to be triggered by Ca^{2+} ions from one to four VGCCs and nanodomain coupling was retained during a short train of five stimuli.

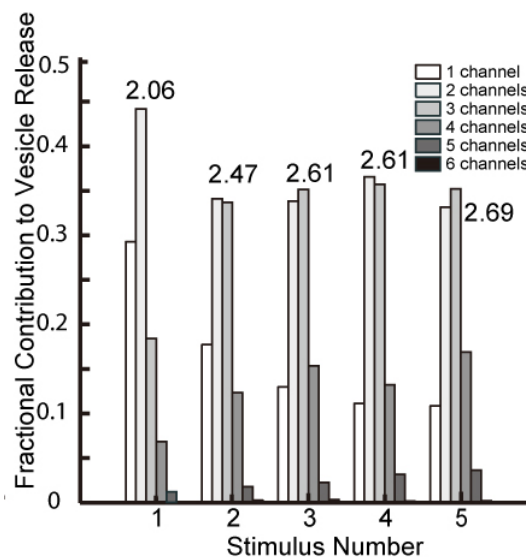


Figure-3.14: Fractional contribution of increasing numbers of VGCC to release during repeated stimuli. Numbers on top of bars for each stimulation event are the average number of VGCCs contributing to vesicle release during that stimulus.

3.3.8 The effect of exogenous buffer on Ca²⁺ binding to synaptotagmin and the second sensor site

In our simulations, BAPTA significantly reduced binding of Ca²⁺ to both synaptotagmin and second sensor sites (Fig-3.15A and B, for 16-Y-site-energy model), while EGTA mainly reduced Ca²⁺ binding to second sensor sites but not to synaptotagmin (Fig-3.15C and D, for 16-Y-site-energy model). This was due to the competition of Ca²⁺ binding to exogenous buffer or binding sites on vesicles. Since BAPTA is a fast buffer ($k_{on} = 4 \times 10^8 \text{ M}^{-1}\text{s}^{-1}$), large concentrations outcompeted Ca²⁺ for binding to both synaptotagmin ($k_{on} = 4 \times 10^8 \text{ M}^{-1}\text{s}^{-1}$) and second sensor sites ($k_{on} = 1 \times 10^6 \text{ M}^{-1}\text{s}^{-1}$), thus reducing both vesicle release and facilitation. On the other hand, the slow buffer EGTA ($k_{on} = 1 \times 10^7 \text{ M}^{-1}\text{s}^{-1}$) competed effectively only with second sensor sites and thus affected facilitation significantly more than initial release. Based on this observation our model suggests that the k_{on} for Ca²⁺ binding to the as of yet unknown second sensor sites is likely to be lower than or on the order of the k_{on} of EGTA ($1 \times 10^7 \text{ M}^{-1}\text{s}^{-1}$).

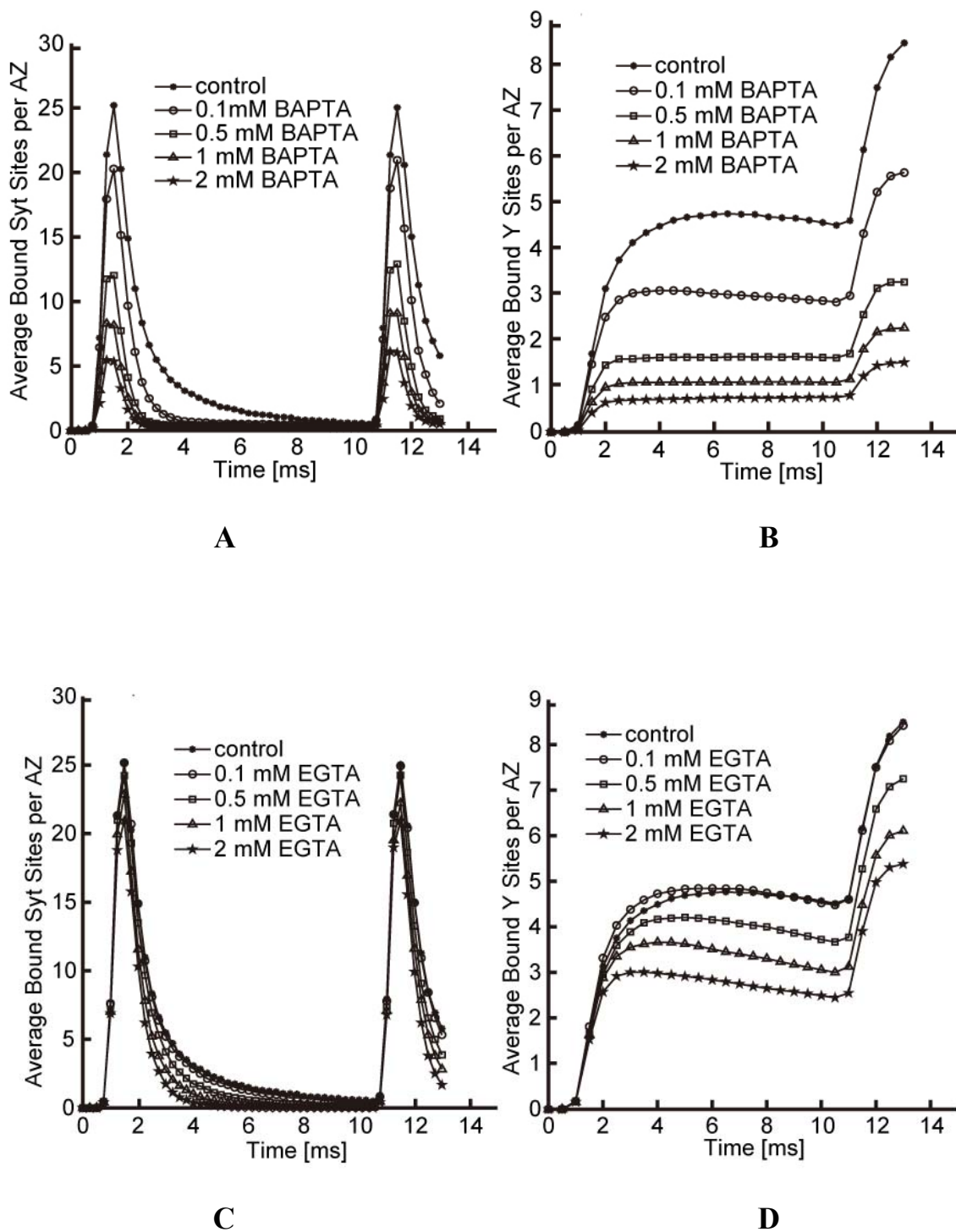


Figure-3.15: Effects of Exogenous buffer on binding sites. A, B. Average number of bound synaptotagmin and Y sites per vesicle as a function of time under control conditions and in the presence of different BAPTA concentrations (average over $n=260000$ vesicles). C, D. Average number of bound synaptotagmin and Y sites per vesicle as a function of time under control conditions and in the presence of different EGTA concentrations (average over $n=260000$ vesicles).

3.4 Discussion

Synaptic facilitation is a key element of neural activity and underlies many important physiological processes. At the frog NMJ, the synaptic response typically grows several-fold during repeated stimulation over the course of several tens to hundreds of milliseconds (Figure-3.3A). A wide range of possible mechanisms have been hypothesized to underlie short-term synaptic facilitation (summarized in (Zucker and Regehr, 2002)) but none has so far been conclusively identified to underlie this important aspect of synaptic function. In fact, different synapses (in different organisms) may employ different facilitation mechanisms altogether (Dittman et al., 2000; Atwood and Karunanithi, 2002; Pan and Zucker, 2009). We do know, however, that facilitation primarily arises pre-synaptically (Zucker, 1989; Fisher et al., 1997; Worden et al., 1997) and that Ca^{2+} ions play a critical role. Several proposed facilitation mechanisms derive from this key insight, most prominently perhaps the so called residual calcium hypothesis which posits that Ca^{2+} remaining in the terminal after a stimulation event contributes productively to future vesicle release events (Delaney and D.W., 1994; Tank et al., 1995; Bennett et al., 1997; Zucker and Regehr, 2002; Matveev et al., 2006). At the calyx of Held, there is mounting evidence that Ca^{2+} triggered facilitation of P/Q type VGCCs might underlie facilitation of transmitter release (Catterall and Few, 2008; Mochida et al., 2008; Catterall et al., 2013). However, since the NMJ features N-type VGCC, the relevance of Ca^{2+} triggered channel facilitation is unclear.

3.4.1 Residual free Ca^{2+} does not lead to facilitation

One facilitation mechanism proposed early on relies on an increase in the presynaptic background free Ca^{2+} concentration due to the accumulation of Ca^{2+} ions from previous stimuli. The idea was that this residual free Ca^{2+} concentration would combine with the Ca^{2+} ions entering the AZ through VGCCs during subsequent stimuli, act on the synaptotagmin sensors that trigger vesicle fusion (Katz and Miledi, 1968; Bennett et al., 1997), and lead to increased vesicle fusion during repeated trials. We could

test this hypothesis directly with our excess-calcium-binding-site model (Dittrich et al., 2013) previously developed under a single pulse paradigm by applying a repeated number of stimuli. However, as shown in Figure-3.3A, our simulations showed no facilitation at all, and instead exhibited minor depression caused by the decrease in numbers of available synaptic vesicles due to prior fusion events. We could trace the lack of facilitation to two fundamental underlying causes. First, the accumulation of residual Ca^{2+} ions in the terminal was too small to contribute productively to subsequent release events. This observation is consistent with previous modeling efforts, which found that accumulation of free residual Ca^{2+} in the AZ was insufficient for facilitation (Blundon et al., 1993; Zucker and Regehr, 2002). As shown in Figure-3.3D, in a model in which Ca^{2+} ions were removed when they encountered the edge of the AZ, the residual Ca^{2+} concentration quickly saturated at around $0.07 \mu\text{M}$. Interestingly, using the peak Ca^{2+} concentration after the first pulse ($[\text{Ca}]_{\text{loc}}$), the residual Ca^{2+} ($[\text{Ca}]_{\text{res}}$) measured in our simulations (Figure-3.3D) and the relationship $([\text{Ca}]_{\text{loc}} + [\text{Ca}]_{\text{res}})^4 / [\text{Ca}]_{\text{loc}}^4$ proposed by Zucker and coworkers (Magleby and Zengel, 1982; Zucker and Regehr, 2002) to estimate facilitation predicted values of 1.8 during the 5th stimulus while none was observed in our simulations. This discrepancy between predicted facilitation based on whole terminal residual Ca^{2+} and the observed lack of facilitation in our actual simulations emphasizes the need for a highly localized Ca^{2+} nanodomain to productively contribute Ca^{2+} ions to vesicle fusion (Dittrich et al., 2013). In fact, in our simulations we did not observe any significant local accumulation of residual free Ca^{2+} near Ca^{2+} sensors (Figure-3.3B) despite the presence of free Ca^{2+} across the whole terminal. Such a nanodomain is established by the VGCCs closely associated with synaptic vesicles. In contrast, the residual Ca^{2+} ions distributed across the whole terminal at the concentrations observed in our simulations are not effective in contributing to this nanodomain and thus vesicle fusion.

A second factor in the observed lack of facilitation in our excess-calcium-binding-site model was

the binding kinetics of Ca^{2+} ions to synaptotagmin on synaptic vesicles. In particular, the dwell time required to keep the latency distribution narrow (Dittrich et al., 2013) was too short for a significant number of ions to remain bound to synaptotagmin during a typical interstimulus interval and thus to contribute to subsequent release events. In principle, increasing the dwell time of Ca^{2+} ions on synaptotagmin could enhance facilitation. Indeed, previous work (Atluri and Regehr, 1996) reported a single Ca^{2+} binding site model with high binding affinity (167 nM), which generated facilitation. However, such a large value for the Ca^{2+} binding affinity does not match the reported values for the high affinity synaptotagmin Ca^{2+} binding site ($\sim 60 \mu\text{M}$) (Radhakrishnan et al., 2009). Our results suggest that facilitation likely derives from a more complex scenario than is provided by a simple accumulation of free Ca^{2+} acting on synaptotagmin.

3.4.2 Facilitation via a second Ca^{2+} sensor on synaptic vesicles

The involvement of multiple, spatially and kinetically distinct Ca^{2+} binding sites in triggering vesicle fusion and facilitation has been proposed previously (Yamada and Zucker, 1992; Tang et al., 2000; Bennett et al., 2004; Matveev et al., 2006). One early facilitation model (Bertram et al., 1996) used four independent Ca^{2+} binding sites with distinct binding affinities ranging from 100 nM to over 1000 μM , and suggested that residual Ca^{2+} existed in bound rather than free form. A similar conclusion was reached based on a different model (Matveev et al., 2006) also with four Ca^{2+} binding sites (two with high and two with low unbinding rates). A series of computational studies on the crayfish NMJ using a finite-difference method (Tang et al., 2000; Matveev et al., 2002), and on the amphibian NMJ via a Monte Carlo approach (Bennett et al., 2004) also used four Ca^{2+} binding sites (three with high and one with low unbinding rates). In the latter study the two types of Ca^{2+} binding sites were segregated in space ($>150 \text{ nm}$) to avoid saturation of the high affinity binding site. Given a typical vesicle diameter

of 50 nm this would place the high affinity Ca^{2+} sensor sites significantly away from the fusing vesicle and at least for the frog NMJ it is not clear what the structural correlate would be. A more recent publication reported a model of vesicle release and facilitation, which included vesicle mobilization, priming and two release pools in addition to the Ca^{2+} binding/unbinding kinetics (Pan and Zucker, 2009). Despite this model's more comprehensive nature, its Ca^{2+} binding/unbinding kinetics were similar to earlier models (Millar et al., 2005; also adopted in Nadkarni et al., 2010) in which all five cooperative binding sites needed to bind Ca^{2+} to trigger fusion. In these models, addition of bound Ca^{2+} ions reduces the dissociation rate which gradually turns the synaptotagmin binding sites into sites similar to the second sensor sites in our model. All the above models rely on a cooperative scheme for Ca^{2+} binding. In contrast, our second sensor model assumes no ad-hoc cooperativity and builds on our previously developed excess-calcium-binding site model (Dittrich et al., 2013) by explicitly accounting for the spatial arrangement of Ca^{2+} sites on synaptic vesicles. Our model includes distinct second sensor sites in close vicinity to synaptotagmin molecules on synaptic vesicles (Figure-3.10). Similar to our synaptotagmin model, these second sensor sites bound Ca^{2+} with simple on and off kinetics ($K_D = 6 \mu\text{M}$, $k_{\text{on}} = 6 \times 10^6 \text{ M}^{-1}\text{s}^{-1}$, $k_{\text{off}} = 36 \text{ s}^{-1}$) chosen to be similar to previous models (Matveev et al., 2006). We found that a model with 16-28 second sensor sites agreed well with our experimental constraints, including short-term facilitation and response to the addition of exogenous buffer BAPTA and EGTA. Interestingly, while the main role of the second sensor sites within our model was in facilitation they also contributed to the initial fusion event. In fact, during a train of five stimuli at 100 Hz the average number of second sensor sites which contributed to fusion increased from 1.3 during the first pulse to 1.9 during the last. These data show that the need for an excess of Ca^{2+} binding sites on both synaptotagmin and second sensor sites (only a small subset of which have to bind Ca^{2+} for release to take place) continues to underlie our model's Ca^{2+} binding dynamics. Thus, while the precise molecular nature of the second Ca^{2+} sensor sites is currently unknown, our simulations predict their numbers to be

on the order of the number of Ca^{2+} sites present on synaptotagmin.

3.4.3 Persistent binding of synaptotagmin leads to facilitation

Recent biochemical and structural studies indicate that Ca^{2+} bound synaptotagmin associates with the lipid membrane and engages in a longer-lived persistent state (~80ms) (Bai et al., 2002; Hui et al., 2006; Lynch et al., 2007; Paddock et al., 2011). We reasoned that such a persistent state could provide the “memory” required for facilitation that was lacking from our original excess-calcium-binding-site model (Dittrich et al., 2013). Indeed, adding such a persistent state to our model led to facilitation in good agreement with our experimental constraints. This is to our knowledge the first model correlating synaptotagmin/membrane interactions with short-term facilitation. While a reaction scheme which included activation of a bound Ca^{2+} sensor had been proposed earlier (Atluri and Regehr, 1996), the authors did not actually implement and test their scheme. Given the simplicity of our persistent binding model it is rather remarkable that it agrees so well with most of our experimental constraints. Nevertheless, due to a lack of Ca^{2+} exchange once in the persistent state our model did not fully capture the effect of exogenous Ca^{2+} buffer such as BAPTA on facilitation. More complex persistent binding schemes, which are outside the scope of the current investigation, will likely be required to faithfully model buffer effects.

3.4.4 Conclusions

Having shown that both the second sensor and persistent binding model are good candidates for mediating facilitation at the frog NMJ, it is conceivable -- indeed likely -- that in biological systems facilitation is due to a combination of both mechanisms and others not considered here. In fact, experiments have revealed distinct phases of short-term facilitation (F1 and F2 facilitation, Magleby,

1979; Zucker and Regehr, 2002). Figure-3.12B showed that facilitation predicted by the second binding site model decayed a little faster than the experimental data, while Figure-3.5 showed the opposite for the persistent binding site model, which suggested that the two models together may underlie combined distinct facilitation mechanisms. In the current study we did not consider facilitation mechanisms, which have been shown to be important at synapses other than the NMJ. Examples are facilitated Ca^{2+} entry through P/Q type VGCCs at the calyx of Held (Mochida et al., 2008; Catterall et al., 2013) or saturation of local buffer (Blatow et al., 2003). Detailed investigation of these mechanisms within the context of our modeling approach will require additional experimental data at the NMJ and may be the subject of a future study.

§ Chapter 4. Comparative analysis of frog and mouse

NMJ models reveals the structure and function

relationship

Given a vesicle release model that predicts short-term plasticity in frog NMJ, in this chapter, I will construct a mouse NMJ model using the same release mechanism, and investigate the remarkable functional differences between frog and mouse NMJs through comparative modeling analysis. My results supported the hypothesis of common active zone building blocks across synapses and revealed how synaptic functions were affected by spatial organization of these building blocks.

4.1 Introduction and motivation

As discussed in Chapter 3, the synaptic quantal release is subject to modulation from repetitive action potential stimuli, which is a phenomenon known as short-term plasticity. The release changes in short-term plasticity can either decrease (depression) or increase (facilitation, augmentation, and post-tetanic potentiation depending on time course) the magnitude of transmitter release during high frequency stimuli (Zucker and Regehr, 2002). Although in Chapter 3 shows significant facilitation at the frog NMJ, short-term plasticity has a broader range of changes at different synapses. Along with short-term plasticity, the synaptic strength which is the magnitude of vesicle release during the initial action potential stimulus, also diverges across different synapses (Atwood and Karunanithi, 2002). Therefore in this chapter I use *synaptic function* to refer to both short-term plasticity and synaptic strength at the synapse. Although synaptic functional diversities may seem obvious from neuron to neuron due to their differences in morphology, electrical and molecular properties (Sherman and Atwood, 1972; Atwood and Karunanithi, 2002; Millar et al., 2002), different branches of axon

originating the same neuron or different presynaptic neurons targeting on the same postsynaptic cell may also evoke distinct responses. One example are the “tonic” and “phasic” synapses in crustacean NMJ (Wiersma, 1961; Nguyen et al., 1997; Msghina et al., 1998). The “tonic” synapse features low synaptic strength but strong facilitation under repetitive stimuli, while the “phasic” synapse features stronger synaptic strength but shows depression under repetitive stimuli (Lnenicka, 1991; Msghina et al., 1998; Pan and Zucker, 2009). Such branch specific functional diversification is also seen in the mammalian CNS. For example within the cerebellar Purkinje cells, the climbing fiber stimulates depression while the parallel fiber stimulates facilitation (Markram et al., 1998; Gupta et al., 2000; Thomson, 2000). These examples demonstrated that even in neurons with similar origin and perhaps with also similar electrical and molecular properties, there is a wide range of synaptic function diversifications. The factors accounting for such synaptic function diversification can be at least either morphological (e.g., active zone size, number of docked vesicle, (Atwood and Karunanithi, 2002)) or molecular (e.g., vesicle priming, mobilization (Pan and Zucker, 2009), and VGCC subtypes), while which factor actually dominates the synaptic function might be case by case. To see that, previous studies in crayfish NMJ revealed no significant correlations between active zone morphological features and their functional differences (Bradacs et al., 1997; Msghina et al., 1998), however studies in frog NMJ clearly show a correlation between active zone size and synaptic strength (Propst, 1985).

Based on recent studies from Dr. Meriney’s and Dr. Dittrich’s lab hypothesized that many synapses in both peripheral and central nervous system are build using a similar building block called *unreliable single vesicle release site* (Figure-4.2), where the *unreliable* means that one action potential stimulus triggers release of a particular vesicle at low probability (Tarr et al., 2013). One model synapse is the frog NMJ studied in Chapter 3. The frog NMJ presynaptic active zone is on average 800 nm in length, 50 nm in width (Pawson et al., 1998), composed of two rows of docked synaptic vesicles on each side of the middle trough (Heuser and Salpeter, 1979; Heuser et al., 1979; Pawson et al., 1998;

Harlow et al., 2001). Between the two rows docked vesicles, there are about 200-250 intramembraneous particles arranged in two parallel rows, where a fraction of these particles are thought to be VGCCs (Pumplin et al., 1981) (see also Figure-4.1). Previous studies suggested that on average each single vesicle release site is associated with only one single VGCC, such that the individual release site with its release machinery, and one tightly associated VGCC together form the *unreliable single vesicle release site*, building block of the active zone (Luo et al., 2011).

A question is whether such *unreliable single vesicle release site* can participate in building an active zone at another synapse. To answer this question, we turned to active zones in mouse NMJ which as shown by EM-imaging, are organized very differently. These active zones are smaller (100 nm in length, 50 nm in width) with on average two docked synaptic vesicles, where about 20 intramembraneous particles (including VGCCs) are arranged on both sides of the two vesicles (Nagwaney et al., 2009) (see also Figure-4.1). If assuming the same percentage of VGCC among intramembraneous particles, each active zone in mouse NMJ would have 4-5 VGCCs.

Functionally, as presented in Chapter 3, synapses in frog NMJ facilitates significantly in response to repetitive action potential stimuli (Tanabe and Kijima, 1989; Suzuki et al., 2000; Ma et al., 2014a). In contrast, synapses in mouse NMJ show depression in response to the same repetitive stimuli. Is it possible that such synaptic function divergence between frog and mouse NMJ is morphologically caused by different organization of the active zone building blocks? In order to rule out possible molecular differences in the two synapses, ideally to test this hypothesis one need construct artificial active zones using the same building blocks (docked vesicle and VGCC). However experimental manipulation of these nanometer scale components is not easy, although recent advances of super-resolution imaging (Heilemann et al., 2002; Rust et al., 2006; Hein et al., 2008; Galbraith and Galbraith, 2011) combined with artificial lipid bilayer system (Shi et al., 2012) might provide future possibilities.

Here in this chapter I again employed realistic computer modeling, which has been proved powerful in studies of synaptic vesicle release (Coggan et al., 2005; Pan and Zucker, 2009; Nadkarni et al., 2010; Dittrich et al., 2013; Ma et al., 2014a).

Chapter 3 presented a comprehensive computer model of vesicle release that predicts short-term plasticity at frog NMJ, incorporating active zone ultrastructure, buffered Ca^{2+} reaction-diffusion, and multiple vesicle-dwelling Ca^{2+} sensors (Dittrich et al., 2013; Ma et al., 2014a). Here I applied the same vesicle release model to mouse NMJ by rearranging the active zone building blocks according to EM imaging data, and found the synaptic functional divergences faithfully predicted by the two models. With further computational analysis, my results not only revealed how active zone ultrastructure organization changes synaptic function, but also strongly supported the proposed hypothesis of active zone building blocks.

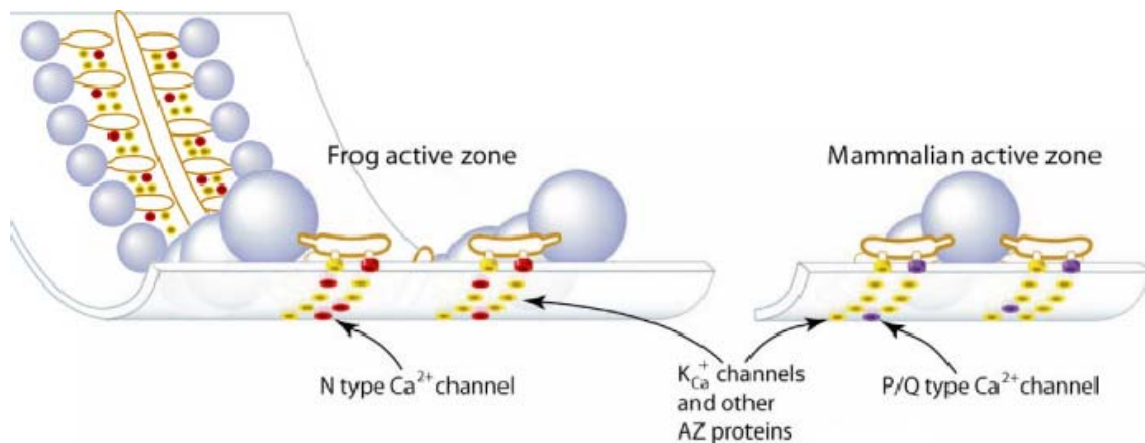


Figure-4.1: Active zone organization in frog and mouse NMJs. Blue spheres represent synaptic vesicles docked with release proteins, red circles represent N-type Ca^{2+} channels, purple circles represent P/Q-type Ca^{2+} channels, and yellow circles represent other AZ proteins. Frog and mouse organization differs in the position of synaptic vesicles within the AZ, number of AZ transmembrane proteins, organization of Ca^{2+} channels relative to synaptic vesicles, and number of single-vesicle release sites that are adjacent to one another. Adapted from (Urbano et al., 2003)

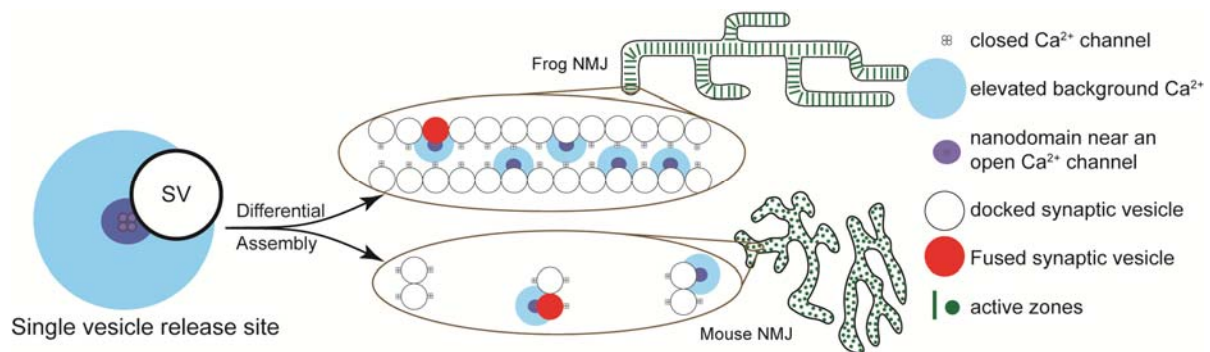


Figure-4.2: Assembly of a basic building block of synaptic active zone (“the single-vesicle release site”) into different types of active zones. Adapted from (Tarr et al., 2013)

4.2 Results

4.2.1 Distinct synaptic function observed at frog and mouse NMJ

We first estimated the average vesicle release per action potential stimulus per active zone using methods mentioned in our previous work (Wachman et al., 2004; Dittrich et al., 2013; Ma et al., 2014a). Under physiological conditions, the average vesicle release per stimulus per active zone, a measurement of synaptic strength, is 0.51 ± 0.09 in frog NMJ, and 0.1 ± 0.01 in mouse NMJ. When considering release probability for individual docked vesicles, it is around 0.019 in frog NMJ (on average about 30 docked vesicles in the active zone), and around 0.05 in mouse NMJ (on average 2 docked vesicles in the active zone).

We then measured the short-term plasticity with repetitive stimuli at 100 Hz. At the frog NMJ, the vesicle release magnitude during the 2nd stimulus immediately rose up to over 1.5 times the 1st vesicle

release magnitude and it continued to reach around 2.5 times the 1st vesicle release magnitude during the 5th stimulus (Figure-4.6A). In the mouse NMJ, no such increase of vesicle release was seen, instead, there was slight but steady decrease (depression) in response to the repeated stimuli (Figure-4.6B).

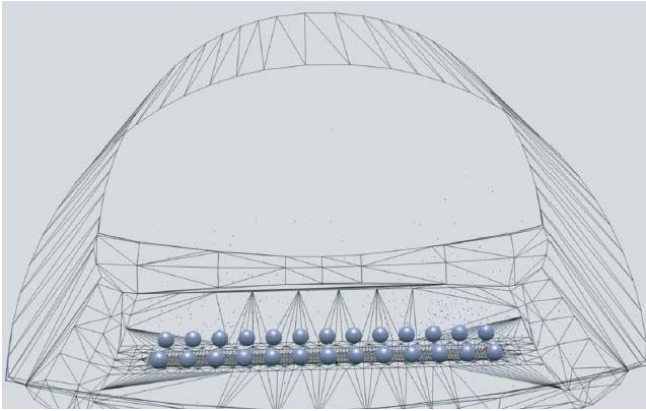
These observations suggest that the frog NMJ has relatively lower probability of release per docked vesicle, and shows strong facilitation under repeated stimuli, whereas the mouse NMJ has higher probability of release per docked vesicle, but shows depression under repeated stimuli. In the next step, we will use computer modeling to explore underlying mechanisms of such synaptic function differences.

4.2.2 A comprehensive mouse NMJ vesicle release model constructed by reassembling active zone building blocks of frog NMJ model

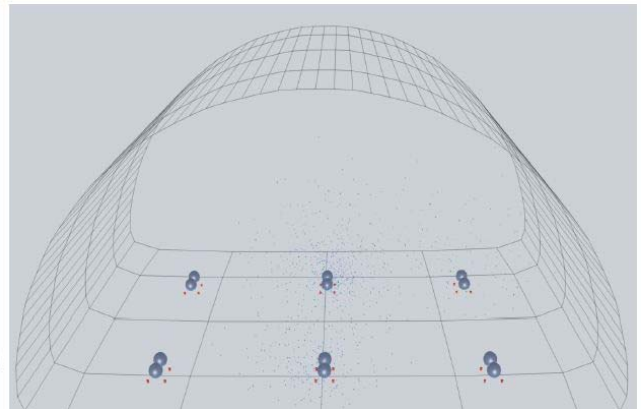
In Chapter 3, we developed a presynaptic vesicle release model at the frog NMJ using the particle-based diffusion-reaction simulation tool MCell (Dittrich et al., 2013; Ma et al., 2014a). The model included a realistic geometry of the presynaptic terminal based on EM tomography (Harlow et al., 2001), along with molecular components including VGCCs, free Ca²⁺ ions, endogenous Ca²⁺ buffer, and Ca²⁺ binding sensors. The model contained one complete frog NMJ active zone with 26 docked vesicles placed in two rows on both sides of the active zone (Figure-4.3A, C, E), where each vesicle was closely associated with one VGCC. Meshes on the bottom of the vesicle were populated with two types of calcium binding sensors, 40 synaptotagmin binding sensors in the middle, and 16 Y binding sensors with low unbinding rates on the periphery (Figure-4.3G). Our previous work show that such a vesicle release model successfully predicted a number of physiological observations of frog NMJ including: VGCC currents, average vesicle release per active zone, 4th order calcium release

relationship (CRR), and release latency (Dittrich et al., 2013). In addition, the model also predicted facilitation growth during repeated stimuli, paired-pulse facilitation (PPF) decay with increased stimulus interval, and exogenous Ca^{2+} buffer's influence on synaptic function (Ma et al., 2014a).

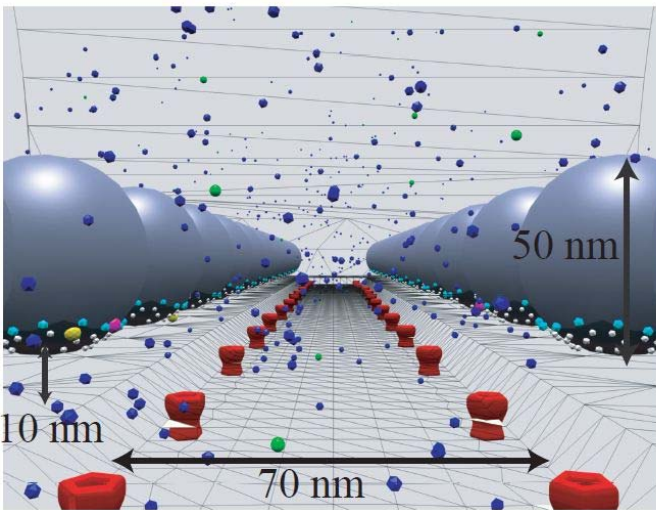
According to mouse NMJ EM-tomography data (Nagwaney et al., 2009), we constructed the mouse NMJ vesicle release model using individual model components from the frog NMJ model without alteration. Since the active zone in the mouse NMJ is much smaller, as depicted by Figure-4.3B, our mouse NMJ model contains six active zones placed in a 2×3 matrix (size is $1000 \text{ nm} \times 1500 \text{ nm}$) on the presynaptic membrane, with a distance of 500 nm between the closest active zone pairs. Each active zone had two docked synaptic vesicles that were identical to those in frog NMJ models (Figure-4.3D, F, H). On each side of the single row of vesicles, EM-tomography data indicated two rows of intramembraneous particles corresponding to VGCCs (Nagwaney et al., 2009). Since the precise VGCC number and location within mouse active zones is unknown, we determined the shown VGCCs in an active zone after trials of several possibilities as described in the later section. In addition, the presynaptic terminal of mouse NMJ model (Figure-4.3B) does not have a wide trough as the frog NMJ model (Figure-4.3A), according to EM-tomography data. To sum up, the mouse NMJ model included a grid of six active zones, with a total number of 12 vesicles and 24 VGCCs (Figure-4.3B, H).



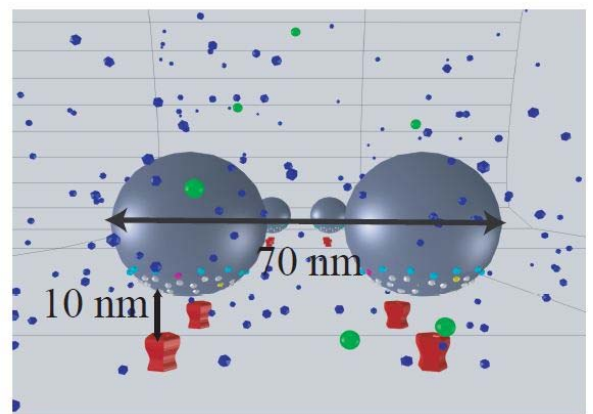
A



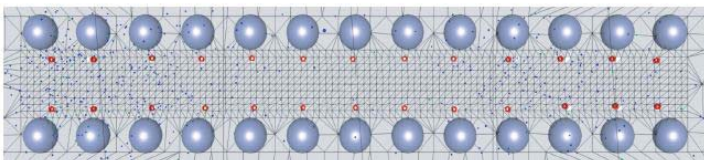
B



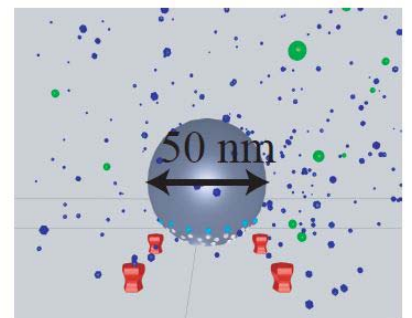
C



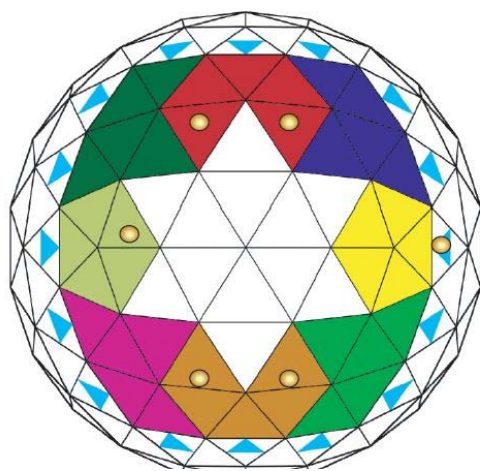
D



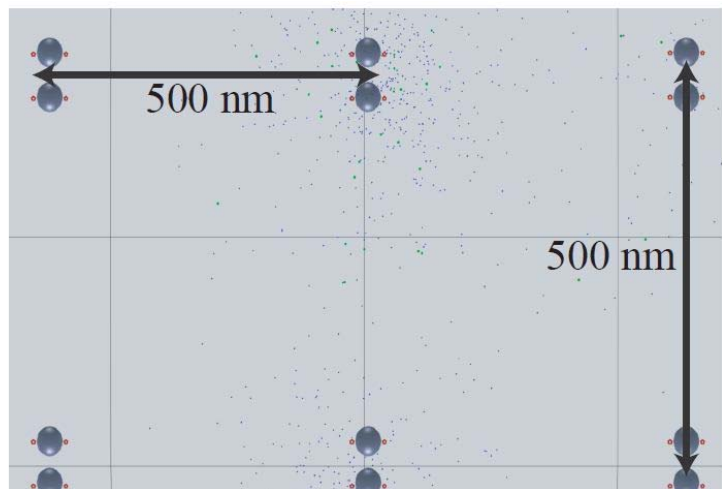
E



F



G



H

Figure-4.3: Comparison of geometric in the frog and mouse NMJ models. Whole terminal view of **A.** frog containing one active zone and **B.** mouse NMJ model containing 6 active zones. Front view (**C**) and top view (**E**) of the active zone at frog NMJ model, side view (**D**), and front view (**F**) of active zone at mouse NMJ model. Here they show docked vesicles (blue sphere), voltage-gated-calcium-channels (VGCC, red), Ca^{2+} ions (green), synaptotagmin Ca^{2+} sensors (white), bound synaptotagmin Ca^{2+} sensors (yellow), Y Ca^{2+} sensors (cyan), bound Y Ca^{2+} sensors (purple), and bound Ca^{2+} buffer (blue). **G** shows binding sensors on bottom of a vesicle. Colored large triangular meshes in the middle represent synaptotagmin binding sensors (40 in total, grouped in 5 to reflect the 5 binding sites of synaptotagmin molecule). The smaller cyan triangular meshes are the 2nd binding sites (16 in total). The orange circles are bound Ca^{2+} ions. **H** shows top view of the 2×3 grid of active zones in mouse NMJ.

The action-potential-dependent transition kinetics of VGCC in the mouse NMJ model are the same as in frog NMJ model (see Chapter 3, (Dittrich et al., 2013; Ma et al., 2014a)), while VGCCs in the open state released Ca^{2+} ions at time-dependent rates calculated from the driving force dependent on extracellular Ca^{2+} concentration. Here we assumed no significant kinetic differences between the used N-type VGCC found in frog NMJ (Kerr and Yoshikami, 1984) and the P/Q-type VGCC found in mouse NMJ (Weber et al., 2010) based on previous studies (Li et al., 2007b).

On bottom of the docked vesicles, there are two types of Ca^{2+} binding sensors, one for normal vesicle release, and one contributing to facilitation at frog NMJ (Ma et al., 2014a). At center of the vesicle bottom there are 40 synaptotagmin binding sensors each placed in a triangular mesh (Fig-24G), where the quantity of synaptotagmin is based on previous biochemical estimates of synaptotagmin copy number per vesicle (Takamori et al., 2006). At the peripheral ring near synaptotagmin there were Y binding sensors (Figure-4.3G), which feature low Ca^{2+} dissociation rates to account for facilitation and are similar to those proposed previously (Tang et al., 2000; Matveev et al., 2006). We have shown that 16 such Y binding sensors were adequate to satisfy all experimental constraints (Ma et al., 2014a).

The synaptotagmin and Y binding sensors are stochastically bound with Ca^{2+} ions during the stimulus in our model. To determine whether a vesicle release event occurred, we used a Monte Carlo energy sampling method. The model assumes that a vesicle needs to cross an energy barrier ($40 k_B T$) before its fusion with presynaptic membrane (Li et al., 2007a; Martens et al., 2007), while binding of Ca^{2+} ions to Ca^{2+} sensors accumulatively reduces the energy barrier. In previous work, we determined that every active synaptotagmin (with at least two out of its five sensors bound by Ca^{2+} ions) could reduce the energy barrier by $8 k_B T$, and every Ca^{2+} bound Y sensor reduced the barrier by $13 k_B T$ (Ma et al., 2014a). The reduced fusion energy barrier on a specific vesicle thus increased fusion probability (sampled using Metropolis-Hasting method assuming Boltzmann distribution, see Chapter 3 for details) of that vesicle.

4.2.3 Frog and mouse NMJs are distinguished by individual vesicle release probability after a single action potential stimulus

The experimentally observed average vesicle release per active zone at the mouse NMJ is 0.1 ± 0.01 . Our first step was to use this constraint to determine quantity and location of VGCCs in the mouse NMJ active zone. To narrow down the parameter search space, we tried VGCC configurations with the following considerations: (1) As suggested by EM-tomography studies, on each side of the two docked vesicles there are two rows of intramembraneous particles, some of which are thought as VGCC (called inner row and outer row in respect to active zone). Thus VGCCs can only be placed at possible locations as shown in Figure-4.1. (2) We assumed the same tight coupling within the *unreliable single vesicle release site* as the frog NMJ, so that any VGCC must be placed close to a docked vesicle. Given these two considerations, after trying several configurations of VGCCs, Figure-4.4 shows that placing one VGCC at the inner row on each side of the vesicle resulted in average release (0.104 ± 0.007) that agrees best with experimental observations (0.1 ± 0.01).

Remember that the average vesicle release per active zone in frog NMJ is 0.51 ± 0.09 (0.45 ± 0.04 predicted by our model). Unsurprisingly frog NMJ has higher release amount per active zone than mouse since the frog NMJ has a larger active zone with more docked vesicles. On the other hand, release probability of an individual vesicle in the frog NMJ is 0.017 (0.45 divided by 26 vesicles), lower than the 0.05 in the mouse NMJ (0.104 divided by 2 vesicles). This is because an individual vesicle in the mouse NMJ is associated with two VGCCs instead of one in the frog NMJ.

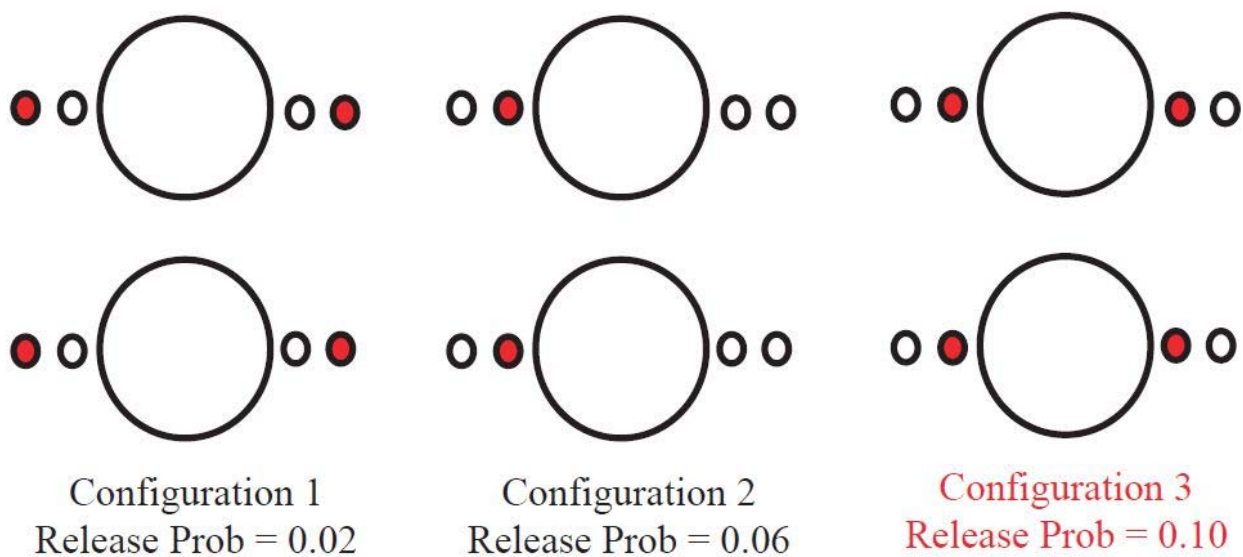
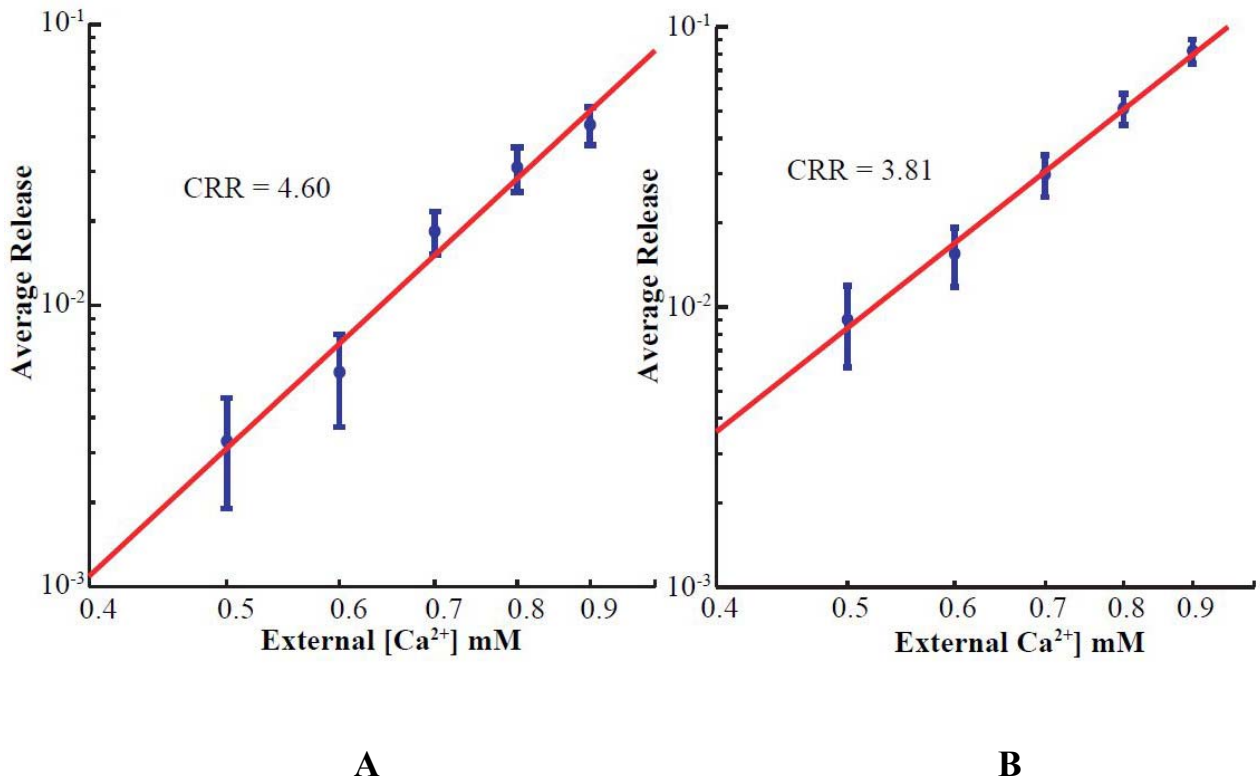


Figure-4.4: Different configurations of VGCCs in mouse active zone. In each configuration, the large spheres are docked vesicles; the small red spheres indicate location of VGCC and open small spheres are potential VGCC locations. Release probability refers to average vesicle release per active zone. Configuration 3 is closest to the experimental observation.

The other two observations we measured and modeled are the calcium release relationship (CRR) and release latency, which are not significantly distinct between the frog and mouse NMJ, but still provided good experimental constraints to validate our models.

The vesicle release at frog NMJ follows a 4th order relationship when external calcium concentration is varied (Katz and Miledi, 1965b; Dodge and Rahamimoff, 1967), while in the mouse NMJ, such relationship is between 3rd and 4th order (Smith, 1988). Although our model has many more binding sensors than previously proposed models, as shown here in Figure-4.5A and B, our model still correctly predicted CRR in both frog and mouse NMJ (4.6 in frog NMJ, and 3.8 in mouse NMJ).

To compare the release latency, we recorded the simulation time point for the occurrence of every vesicle release event. The histogram of these time points as shown in Figure-4.5C and D also matches their experimental observations in both frog and mouse NMJ.



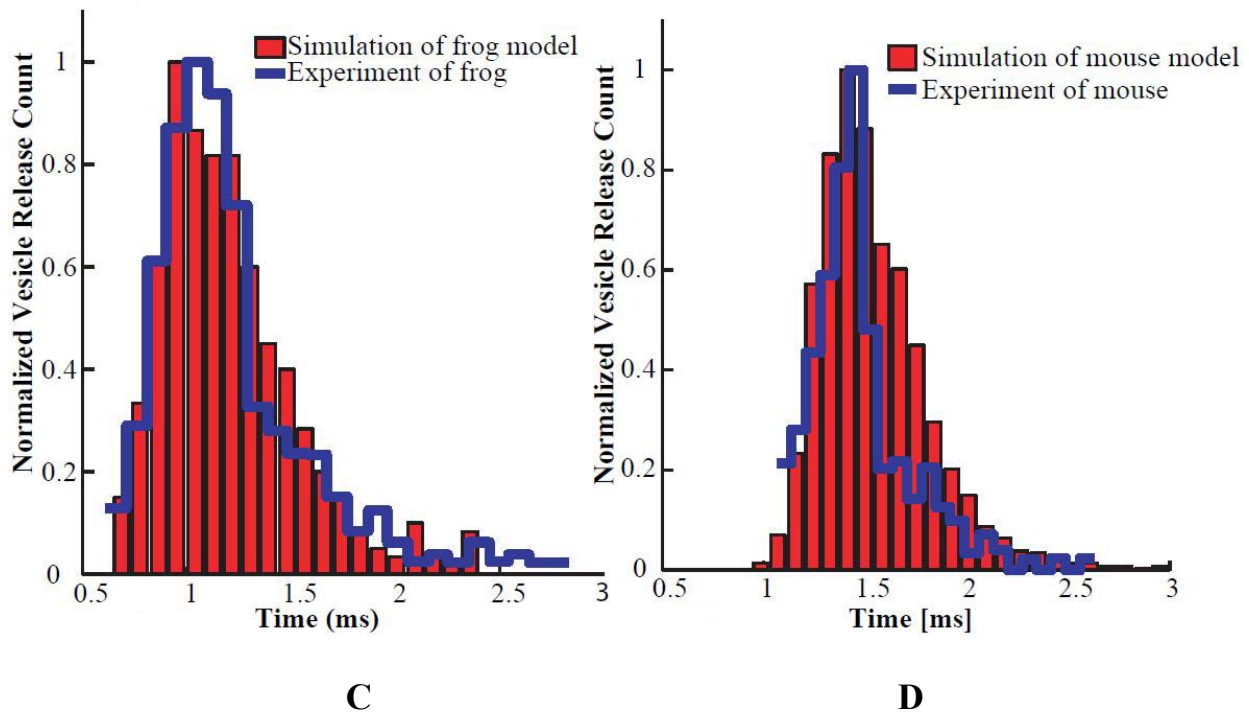


Figure-4.5: CRR and release latency of frog and mouse NMJ. Log-log plot of vesicle release versus external Ca^{2+} concentration at frog NMJ (A) and mouse NMJ (B). Blue dots show simulation data points, and red line shows the regression, where its slope equals to CRR. The release latency of frog NMJ (C) and mouse NMJ (D). Red bars are simulation data, and blue lines are the experimental data (Katz and Miledi, 1965a, 1965b).

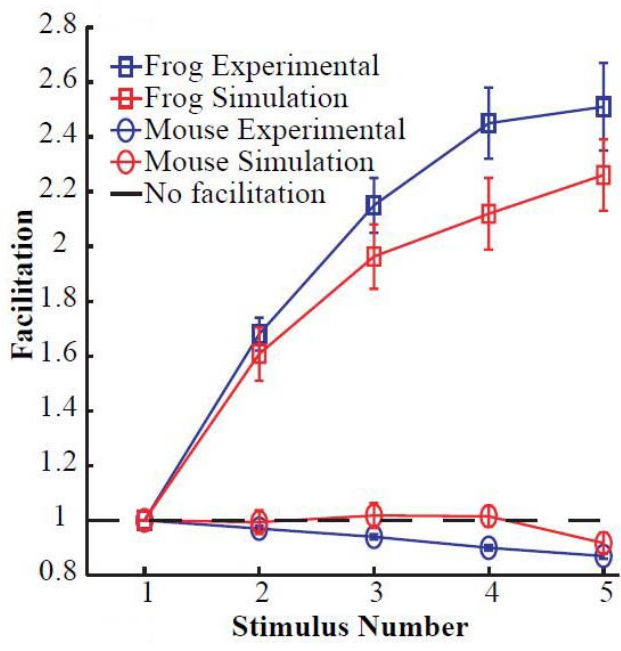
4.2.4 Frog and mouse NMJs are distinguished by short-term plasticity

When the frog NMJ was stimulated by repeated action potentials at 100 Hz, the vesicle release facilitated from 1.6 times of the size of the 1st vesicle release at the 2nd stimulus, and to over 2.5 times at the 5th stimulus. Our frog NMJ model successfully captured such a facilitation increase when action potentials were applied sequentially at also 100 Hz, although the modeled facilitation was not as strong as experimentally observed (Figure-4.6A, Ma et al., 2014a). Our frog NMJ model also predicted the

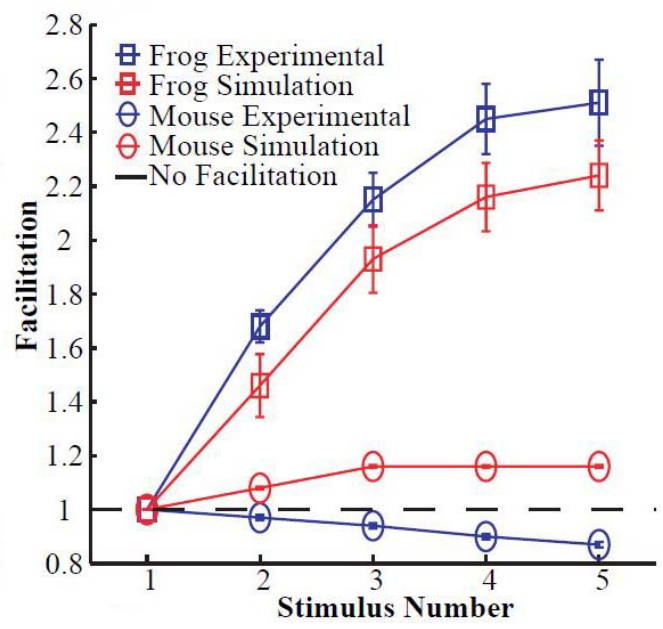
experimentally observed paired pulse facilitation decrease with increased inter stimulus interval, although the modeled facilitation decays a little faster than experimentally observed (Figure-4.6C).

In contrast, instead of showing any signs of facilitation, the vesicle release in the mouse NMJ did not show any sign of facilitation in response to the 100 Hz action potential stimuli. As shown in Figure-4.6B, our mouse NMJ model successfully predicted the short-term plasticity in the form of depression, which lags a little behind experimentally observed values. Like the experimental observations, our model did not predict any paired pulse facilitation decay, but the modeled values fluctuate more as compared to the experimentally observed values (Figure-4.6D).

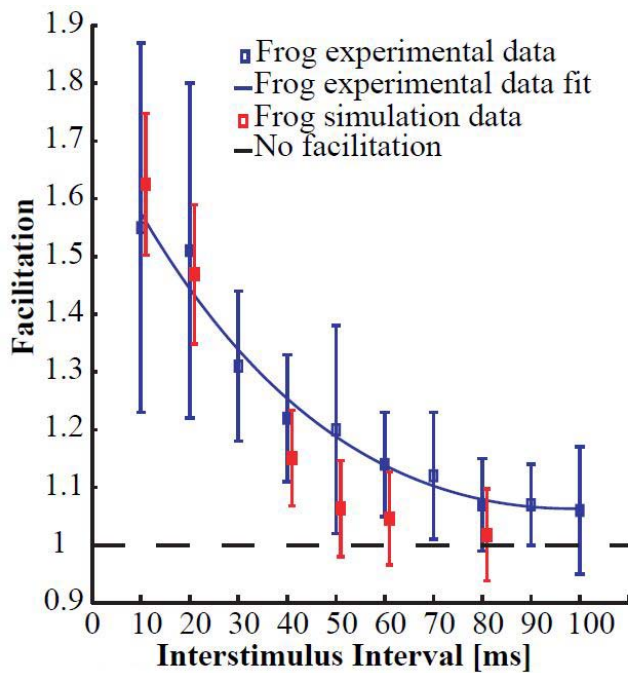
These results show that our models constructed simply by differential assembly of active zone building blocks indeed were capable of predicting short-term plasticity differences between frog and mouse NMJ.



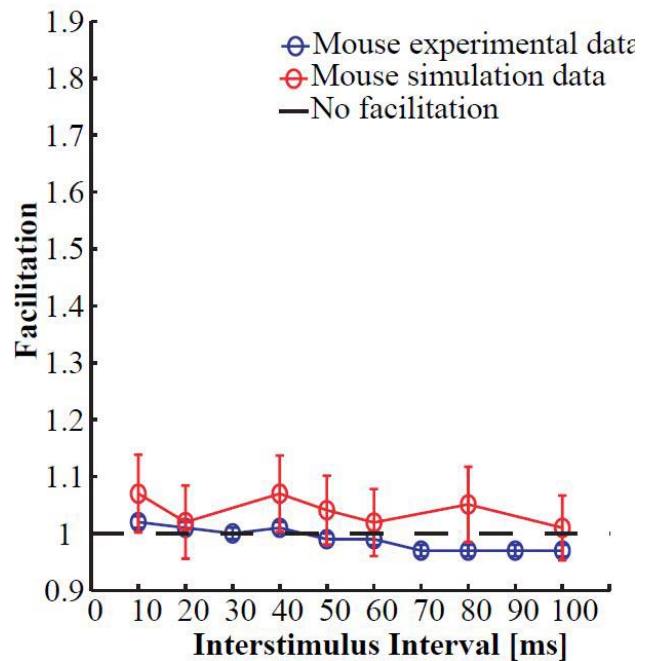
A



B



C



D

Figure-4.6: Comparison of frog and mouse NMJ in terms of short-term plasticity. A. Facilitation at each stimulus, with square box showing data from frog NMJ, and circle showing data from mouse NMJ, also showing both simulation using the two binding site vesicle release model (red) and experimental data (blue). **B.** The same as A except that simulation was using the persistent binding site model. **C and D,** using the two binding site model, show paired-pulse facilitation decay with increasing interstimulus interval at frog NMJ (**C**), and the peer observations at mouse NMJ (**D**). Simulation data are shown in red and experimental data are shown in blue.

4.2.5 The short-term plasticity differences are insensitive of the modeled release mechanism

Next we wondered whether such divergences in short-term plasticity seen in our two models are relevant to the specific way the vesicle release mechanism was modeled. To examine this question, we tested the two models using a different release mechanism.

We have previously tested a persistent binding site release model (see Chapter 3) for facilitation without using the Y binding sensors (Ma et al., 2014a). Motivated by the lipid membrane/synaptotagmin interactions (Paddock et al., 2011), this model assumes a persistent state of the synaptotagmin that keeps residual Ca^{2+} bound long enough to contribute to the next stimulus evoked vesicle release (Figure-3.4). In this model, vesicle release was triggered only when at least three synaptotagmins are persistent on a vesicle. Although the persistent binding site model at the frog NMJ did not appropriately predict its sensitivity to exogenous calcium buffer (Yamada and Zucker, 1992; Tang et al., 2000; Matveev et al., 2006; Ma et al., 2014a), it may still distinguish short-term plasticity between the frog and mouse.

Indeed when applying the persistent binding sensor model to both frog and mouse NMJ, similar divergence in short-term plasticity was observed (Figure-4.6B). Since the persistent binding site model, and the model with two types of bind sensors both predicted the divergence in short-term plasticity between frog and mouse NMJ, I suggest that such synaptic function divergence is not sensitive to the specific release mechanism.

4.2.6 Vesicle release is triggered by nanodomain coupling between VGCC and Ca^{2+} sensors

Previous studies suggested that VGCCs and Ca^{2+} sensors in the same active zone became functionally coupled when they are close in position (< 100 nm), which is usually called nanodomain coupling (Simon and Llinás, 1985; Stanley, 1993; Eggermann et al., 2012). Vesicle release under the influence of nanodomain coupling is triggered primarily by one or very few close VGCC(s) (Stanley, 1993; Wachman et al., 2004). In contrast, vesicle release controlled by microdomain coupling (distance

between VGCC and vesicle > 100 nm) usually depends on a Ca^{2+} cloud built up by Ca^{2+} flux through several nearby VGCCs (Eggermann et al., 2012; Vyleta and Jonas, 2014).

The distances between a vesicle and its closest VGCC(s) in frog and mouse NMJ presynaptic active zones are less than 100 nm, implying nanodomain coupling is possible in these active zones. Previous research demonstrated that Ca^{2+} from one or two channels controlled fusion of a single vesicle at the frog NMJ, and the channel cooperativity depends mainly on geometrical relationship (Shahrezaei et al., 2006). The particle-based stochastic simulation allowed us to track every Ca^{2+} ion that existed in our model, and made it possible to find a relationship of geometrical distance and VGCC's influence over vesicle fusion. We then tracked the origin of all Ca^{2+} ions bound to a vesicle at the time of the vesicle's fusion in response to the 1st stimulus, and found that 72.2% of Ca^{2+} ions came from the VGCC closely associated with each vesicle (AC, see Figure-4.7), 6-7% from each of the two next-door-neighbor VGCCs (NDC, see Figure-4.7), about 4% from the cross-street-neighbor VGCC (CSC, see Figure-4.7), and about 10% from all other VGCCs.

These results are consistent with our previous results (Dittrich et al., 2013), supporting the hypothesis that vesicle release in the frog NMJ is primarily triggered by the closest VGCC, while several nearby VGCCs also make minor contributions.

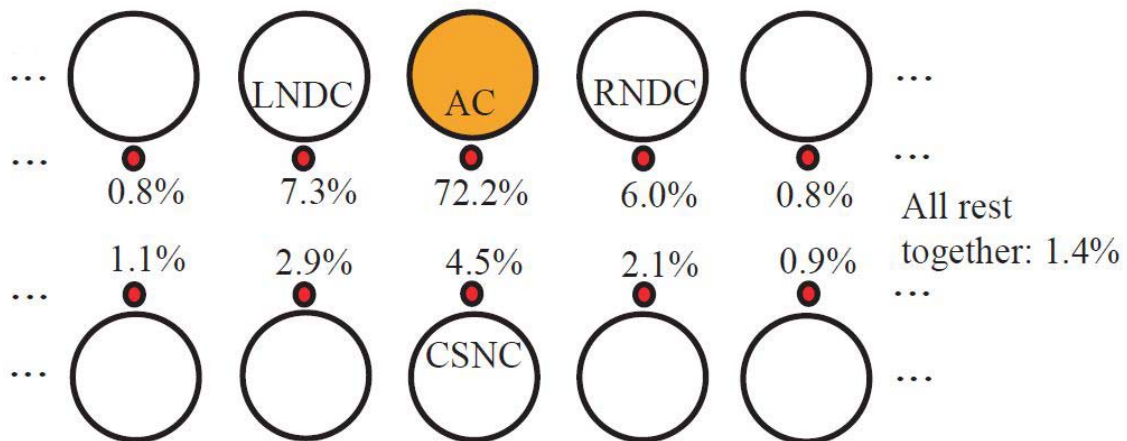
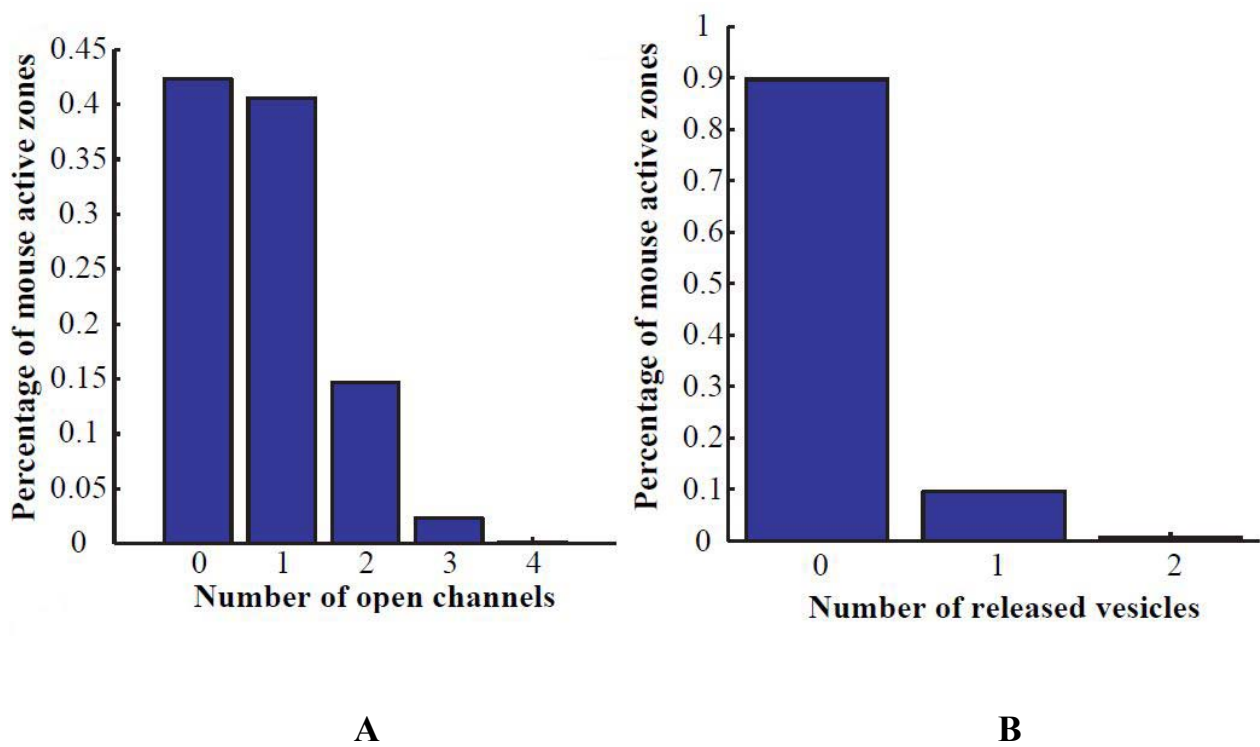
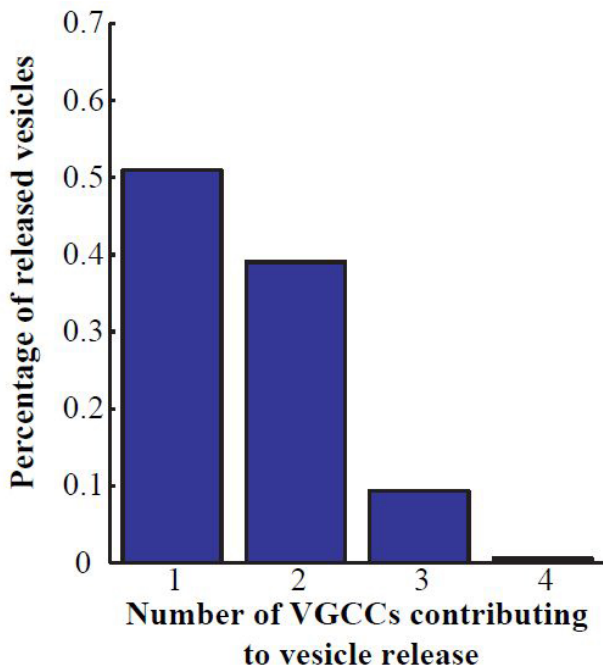


Figure-4.7: VGCC contributions to vesicle release at frog NMJ. Illustrated here is a fraction of frog NMJ active zone. Large blank spheres represent docked synaptic vesicles, and the large orange sphere is the released vesicle. The smaller red spheres represent VGCCs. VGCCs that are close to the released vesicle (in orange) are named as the following. AC stands for associated channel, LNDC stands for left next-door-neighbor channel, RNDC stands for right-next-door-neighbor channel, and CSNC stands for cross-street-neighbor channel. Number besides a VGCC indicates the averaged percentage of Ca^{2+} bound to the released vesicle that came from that individual VGCC.

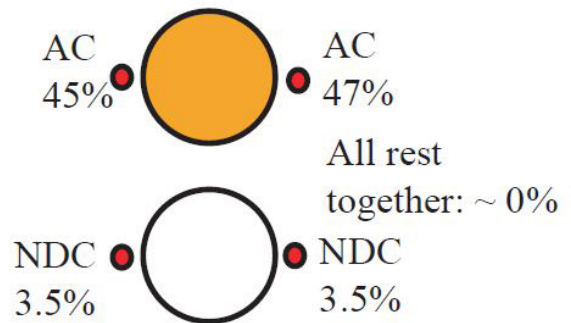
The mouse NMJ has smaller active zones, separated around 500 nm from each other, and each active zone is packed with only two vesicles and four VGCCs in our model. In response to a single stimulus, 42% of active zones have no open VGCCs at all, 40% of active zones have one and 14% have two open VGCCs, whereas only a few active zones have three or all four VGCC openings (Figure-4.8A). Vesicle release is even rarer than VGCC openings. Again in response to a single stimulus, almost 90% of active zones do not have any vesicle release events after the stimulus, 9% of them have one of the two vesicles released, and less than 1% of them have two vesicles released (Figure-4.8B). A detailed analysis showed vesicle release probabilities after VGCC opening conditions of varying open numbers and positions within the active zone (Figure-4.9). A general trend is that more open VGCCs close to a vesicle result in increased release probability. However, considering the rare chance of multiple VGCC openings, vesicle release is mostly triggered by opening of the one nearest VGCC.

We also tracked the origin of all Ca^{2+} ions bound to a vesicle at the time of fusion, and found that 45-47% of Ca^{2+} ions came from each of the two VGCCs closely associated with the vesicle (AC, see Figure-4.8D), and around 7% from the other two next-door-neighbor VGCCs (NDC, see Figure-4.8D). Almost no Ca^{2+} contribution was found from VGCCs in another active zone, suggesting that these small active zones are functioning independently. On the other hand, within an active zone, the two associated channels (AC) provided over 92% Ca^{2+} ions, higher than the 72% Ca^{2+} ions provided by associated channels (AC) in frog NMJ. As shown in Figure-4.8C, over 50% vesicle release events in the mouse NMJ were triggered by one VGCC and 40% by two VGCCs. These results suggest that vesicle release in the mouse NMJ is strongly nanodomain coupled.



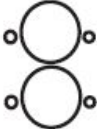
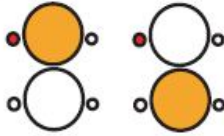
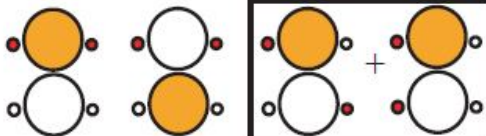
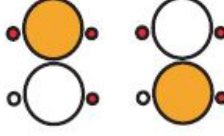



C



D

Figure-4.8: Analysis of mouse NMJ under single action potential. **A.** Histogram of number of open VGCCs within a mouse NMJ active zone during one action potential. **B.** Histogram of number of released vesicles within a mouse NMJ active zone during one action potential. **C.** Histogram of number of VGCCs contributing to vesicle release within a mouse NMJ active zone during one action potential. “Contributing” means having Ca^{2+} bound to vesicle at the moment of release. **D.** VGCC contributions to vesicle release at mouse NMJ active zone. Large blank spheres represent docked synaptic vesicles, and the large orange sphere is the released vesicle. The smaller red spheres represent VGCCs. AC stands for associated channel; NDC stands for next-door-neighbor channel. Number besides a VGCC indicates the averaged percentage of Ca^{2+} bound to the released vesicle that came from that VGCC.

P(number of open VGCCs)	Vesicle release probabilities for open VGCC patterns
P(0)=42.4%	 0%
P(1)=40.3%	 14.84% 0.11%
P(2)=15.0%	 51.04% 0.46% 30.22%
P(3)=2.2%	 61.30% 27.09%
P(4)=0.1%	 66.43%

4.2.7 Short-term plasticity is affected by the spatial organization of VGCCs

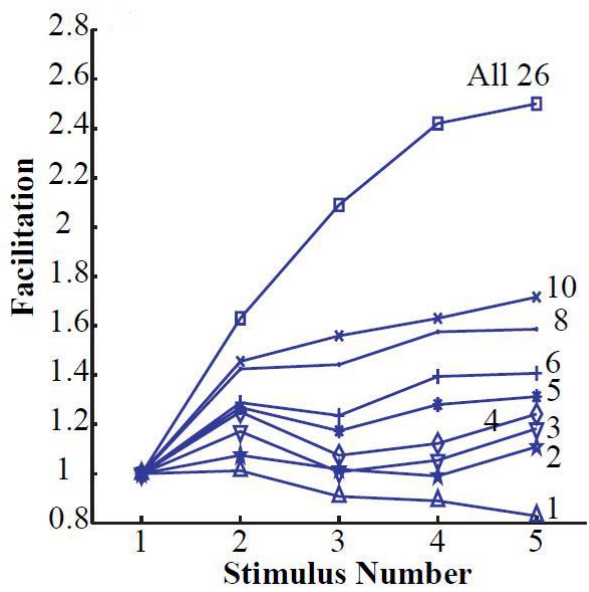
When simulating the vesicle release model with multiple action potential stimuli, we observed significant vesicle release facilitation in the frog NMJ model, whereas in the mouse NMJ model, we observed almost constant vesicle release with minor depression. Since our mouse NMJ model was built by spatially rearranging the active zone release building blocks from the frog NMJ model, the following analysis sought to understand in detail how such spatial organization affected short-term plasticity.

In the frog NMJ release model, Ca^{2+} ions entered the presynaptic terminal through 26 VGCCs. If we reduced the number of available VGCCs within the active zone, which corresponds to experimentally blocking VGCCs using neurotoxins, we then observed a sharp decrease of facilitation. As shown in Figure-4.10A (see also Figure-4.11), when there was only one associated VGCC left, the facilitation completely vanished and was replaced by depression, similar to that seen in the mouse NMJ. When increasing the number of available VGCCs in a stepwise fashion, the facilitation slowly recovered to its full level in the presence of all 26 VGCCs. Such short-term plasticity transitions highlighted the importance of active zone size and spatial organization in determining function.

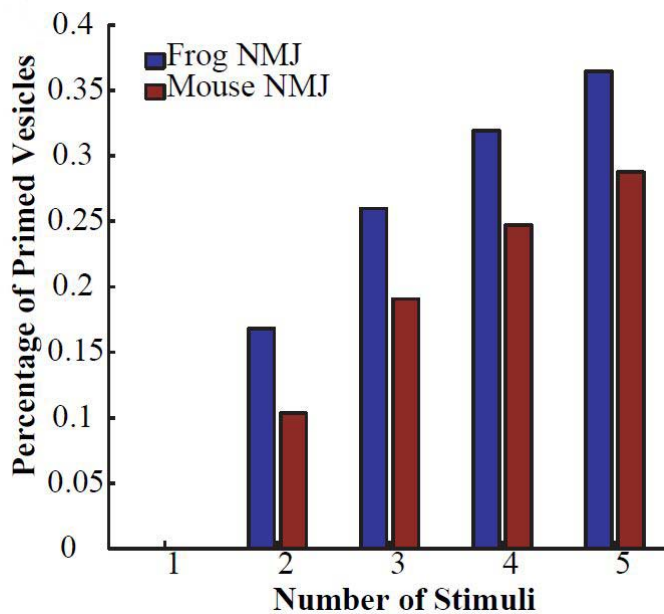
According to the release mechanism in our model, vesicles that are already bound with Ca^{2+} ions from previous stimuli are more likely to release in the future, since they need fewer bound Ca^{2+} ions to reach a release triggering condition. We call these vesicles *primed* vesicles, in contrast to the *unbound* vesicles which are not bound by any Ca^{2+} ions. Thus the proportion of *primed* vesicles is a good indicator of facilitation intensity. As shown in Figure-4.10B, from stimulus 2 to 5, the frog NMJ always has a higher proportion of *primed* vesicle than observed in the mouse NMJ. More strikingly, we found that release probability of *primed* vesicles is almost 8 times that of *unbound* vesicles at frog NMJ (Figure-4.10C), whereas at the mouse NMJ the release probability of *primed* vesicles is at most 2.5

times that of *unbound* vesicle (Figure-4.10D), albeit even though that the mouse NMJ has higher absolute release probability per vesicle. Combining the two factors (proportion of *primed* vesicles, and the release probability ratio between *primed/unbound* vesicles), we see in Figure-4.10E that primed vesicles made more prominent contributions to vesicle release at the frog NMJ, and subsequently lead to significantly more facilitation than the mouse NMJ (Figure-4.10F).

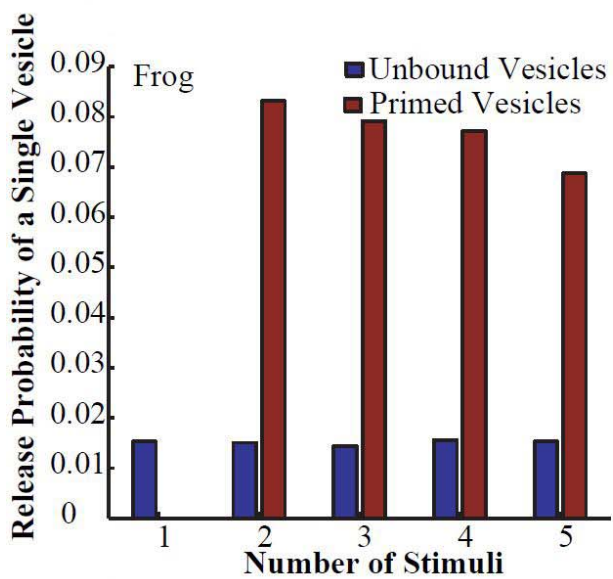
We then tracked the contribution of individual VGCC's to the formation of *primed* vesicles. As shown in Figure-4.12A, in the frog NMJ at the 5th stimulus, only about 54% of Ca²⁺ ions bound to *primed* vesicles came from the closely associated channel (AC). Compared to Figure-4.7, in which about 72% of Ca²⁺ ions bound to released vesicle during single action potential came from the closely associated channel, we found a wider range of VGCCs were contributing to formation of the *primed* vesicles (more than 10 VGCCs) in the frog NMJ. On the other hand in the mouse NMJ, Ca²⁺ ions bound to primed vesicles at the 5th stimulus almost exclusively came from VGCCs within the small active zone (4 VGCCs, Figure-4.12B). In summary, these data show active zone spatial organization affects formation of *primed* vesicles, which in turn affects the short-term plasticity.



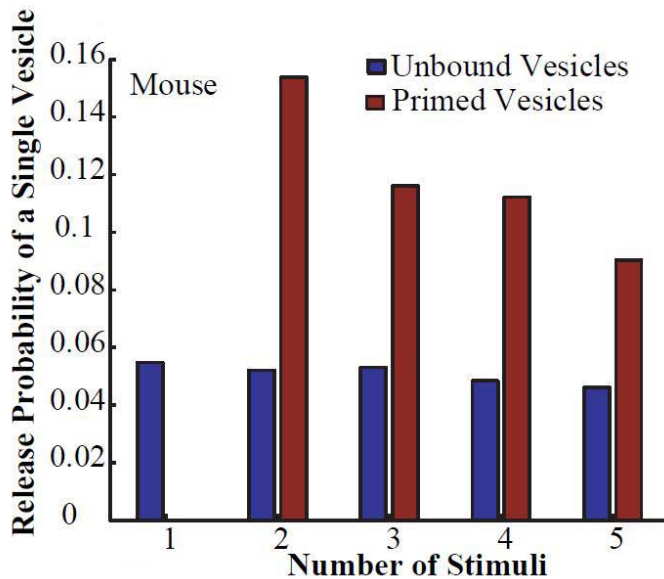
A



B



C



D

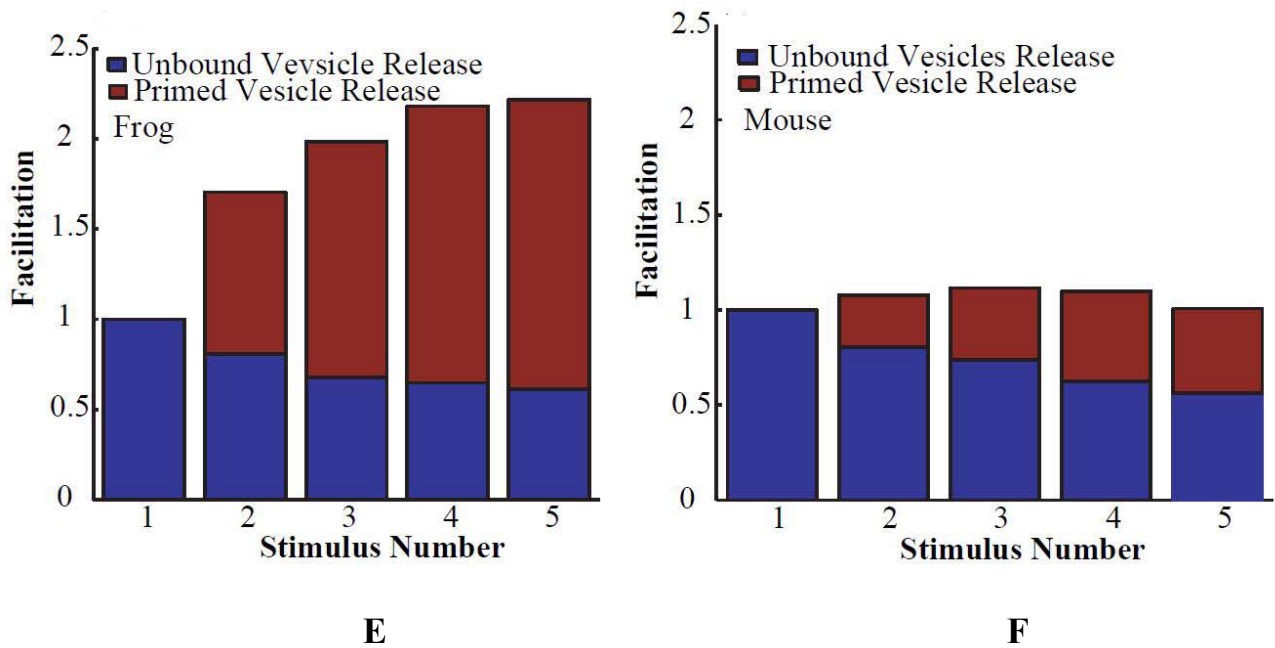


Figure-4.10: Analysis of short-term plasticity. **A.** Facilitation of frog NMJ active zone with different number of available VGCCs. Number besides each curve indicates number of VGCCs, where detailed VGCC configurations are shown in Figure-XX. **B.** At different stimulus, percentage of primed vesicles in frog (blue) and mouse (red) NMJ. **C** and **D**, Release probability of primed (red) and unbound (blue) vesicles at frog (**C**) and mouse (**D**) NMJ. **E** and **F**, facilitation decomposition, showing fraction of contribution from primed (red) and unbound (blue) vesicles at frog (**E**) and mouse (**F**) NMJ.

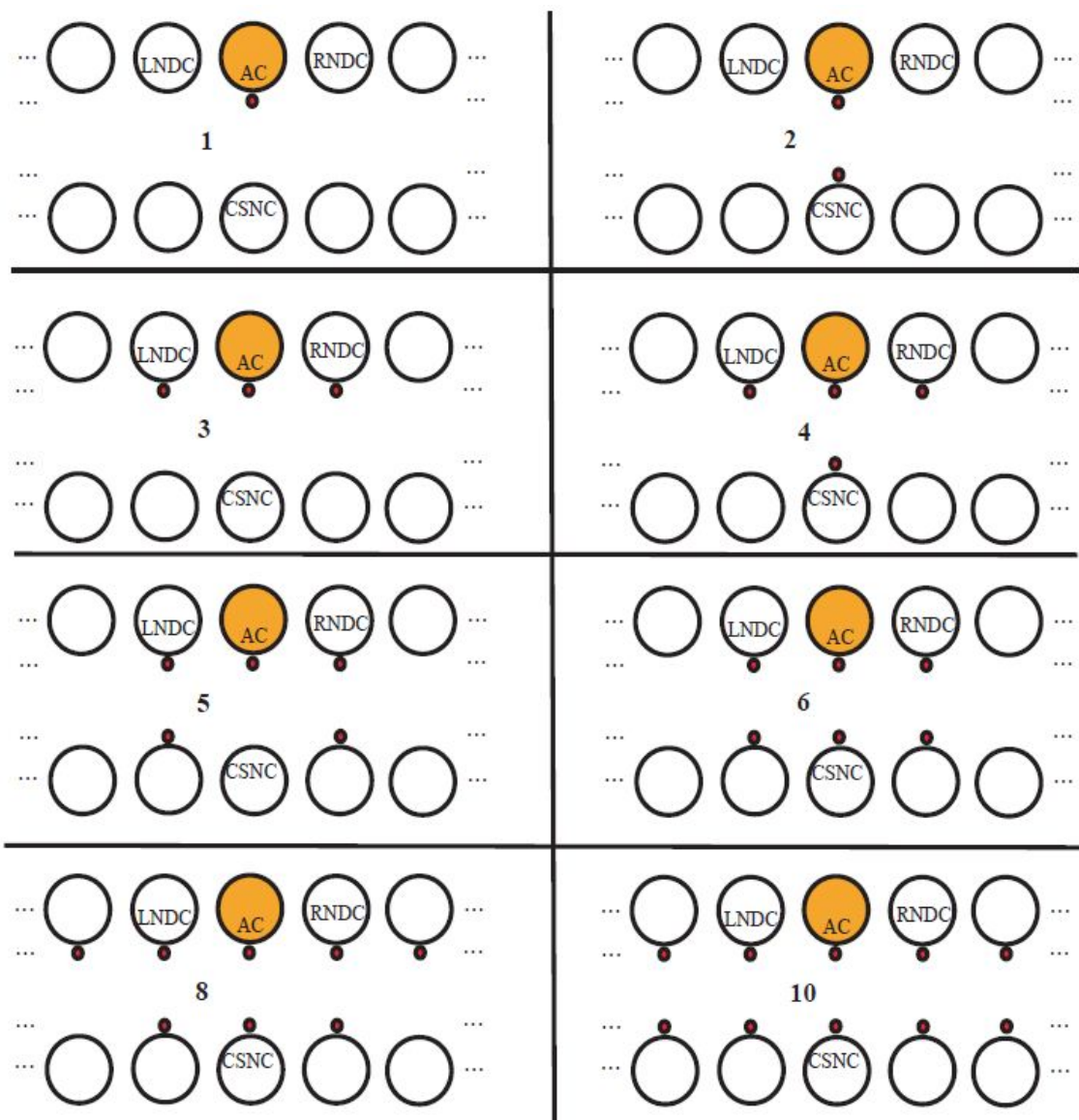
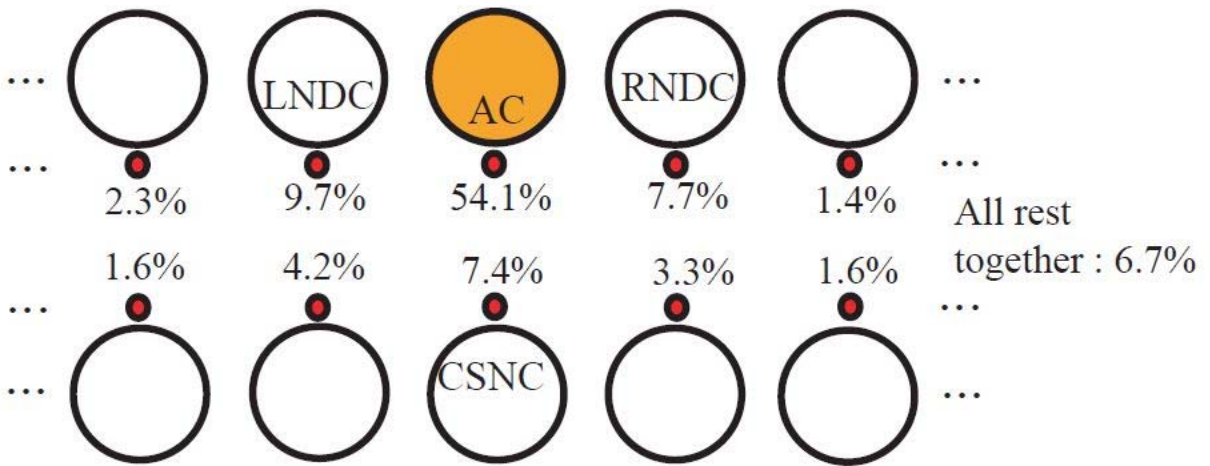
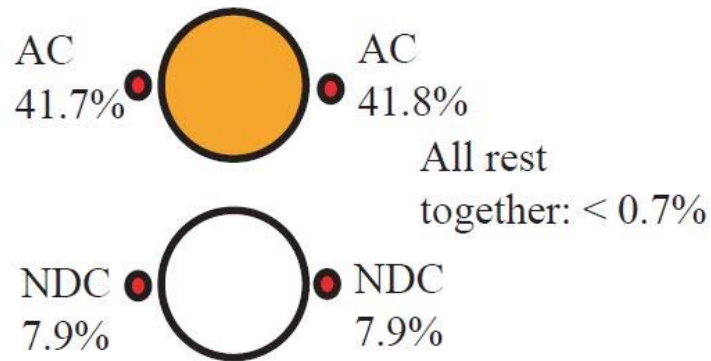


Figure-4.11: Configurations of VGCCs in frog NMJ for plot shown in Figure-4.10A. Orange sphere is the released vesicle. Red spheres are available VGCCs. Number in each block indicates available VGCC quantity, corresponding to Figure-4.10A.



A



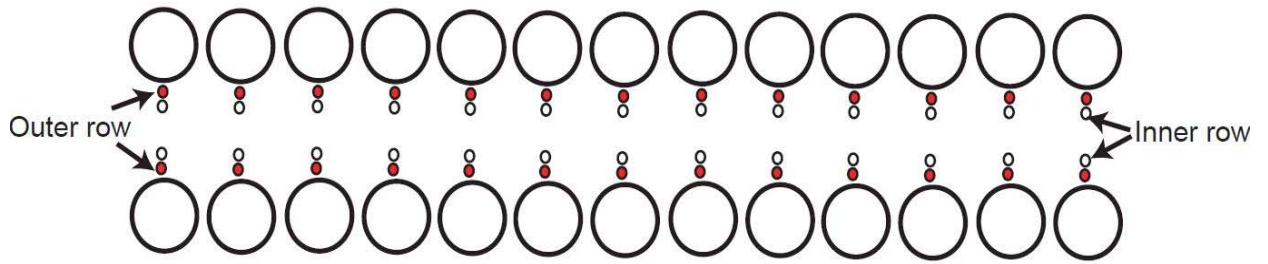
B

Figure-4.12: Contribution from VGCCs to primed vesicle. Here is showing percentage of Ca^{2+} ions bound to primed vesicle (orange) from individual VGCCs at frog (**A**) and mouse (**B**) NMJ.

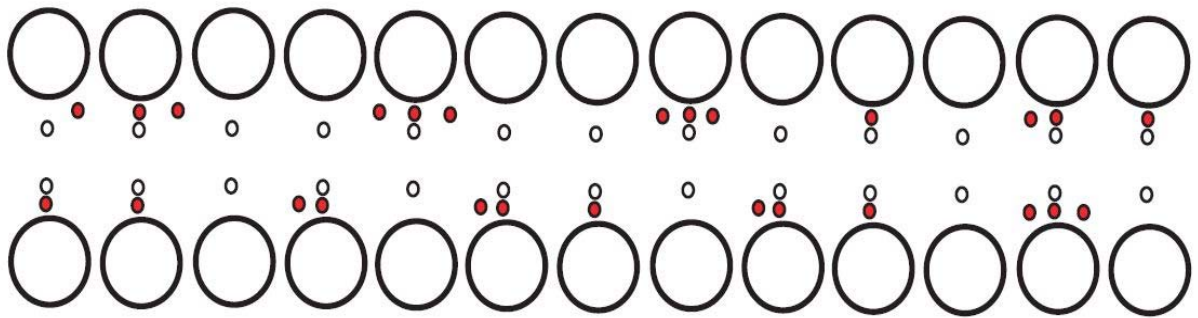
4.2.8 Short-term plasticity at the frog NMJ is affected by distance between associated VGCC and the docked vesicle

Intracellular recordings at the frog NMJ showed significant quantal content variations between individual synapses, which correlated with variations of active zone number across nerve terminals. However, there is no large difference in the size of individual active zones, or the number of intramembraneous particles across active zones as observed by freeze-fracture EM (Pawson et al., 1998). Thus it is possible that these sub active zone variations derived from heterogeneity in organization of the VGCCs within the active zone.

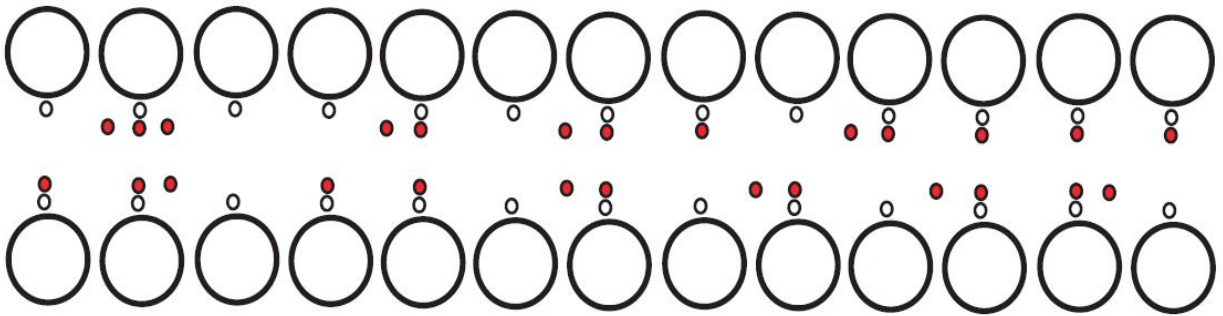
In fact, preliminary simulation data at the frog NMJ already supported this hypothesis. While keeping the total number of VGCCs fixed as 26, there was no significant vesicle release reduction (from 0.5 to 0.486) when randomizing VGCC locations within the outer row of intramembraneous particles (Figure-4.13A and B). However, when all 26 VGCC positions are randomized at the inner rows which are further away from vesicles, there is a significant drop of vesicle release from 0.5 to 0.14 (Figure-4.13A and C). Randomizing VGCC position at both inner and outer row also yielded a significant drop of vesicle release from 0.5 to 0.25 (Figure-4.13A and D). Thus it seems the longitudinal VGCC position variations (in the same direction as active zone length) do not affect vesicle release as much as variations in the width direction of active zone. Indeed, moving the entire rows of VGCCs from their original position towards middle of active zone (away from vesicles) resulted in dramatic decrease of vesicle release and increase of facilitation (Figure-4.14).



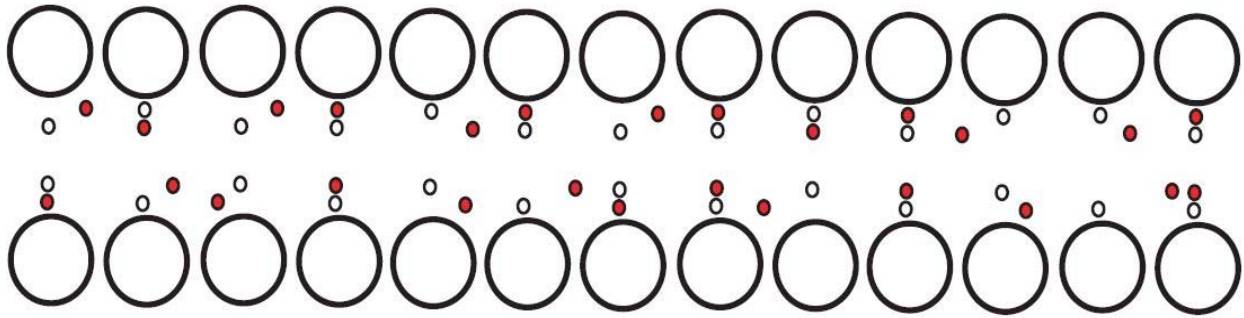
A



B

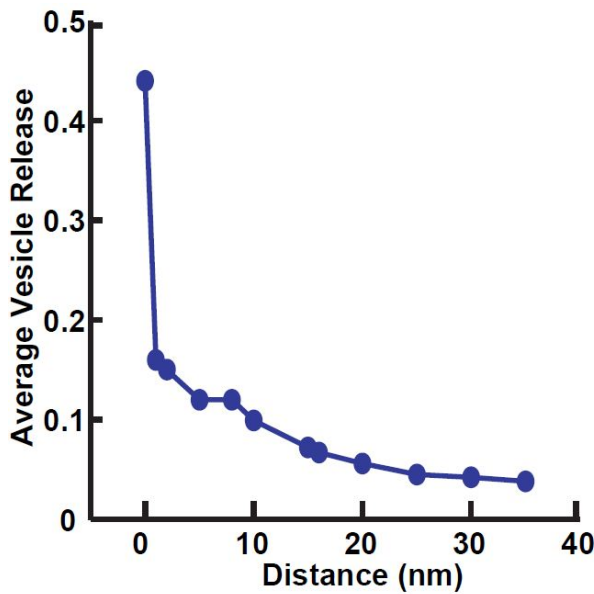


C

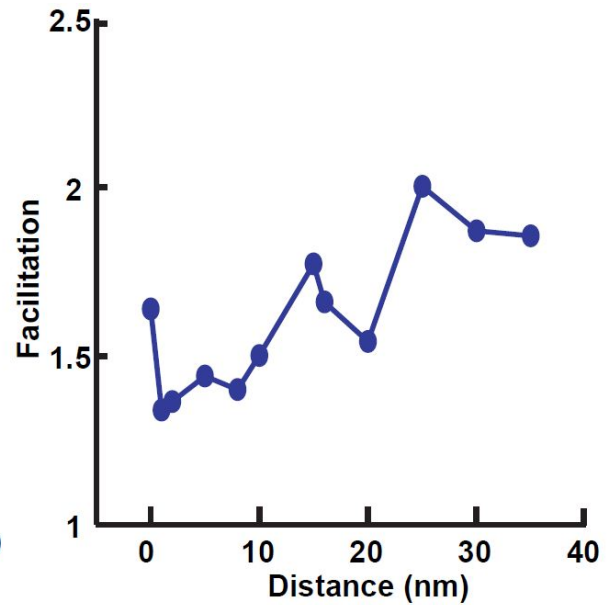


D

Figure-4.13: Illustration of VGCC location randomization. Large spheres are docked vesicles. Small red spheres are VGCCs, and small blank spheres are non-VGCC intramembraneous particles. Illustration is not draw in real scale. **A.** Control, showing inner and outer rows. **B, C, D.** Examples of VGCC location randomization at outer (**B**), inner (**C**) and both inner/outer rows (**D**).



A



B

Figure-4.14: Synaptic function affected by VGCC-vesicle distance at frog NMJ.
A. Average vesicle release predicted by models when two entire rows of VGCCs are moved towards the active zone center. Distance 0 nm indicates their original positions.
B. Facilitation predicted by models at the same conditions as **A**.

4.3 Discussion

Ever since the early characterization and studies of synapses, researchers began to realize the functional diversification among synapses. Giant synapses in frog and squid NMJ reliably release many vesicles in response to an action potential, whereas most synapses in CNS have smaller size packed with single active zone, and do not release vesicles so often. In addition to these obvious differences, synapses of the same neuron type may show branch-specific differences, or synapses with the same target cell may evoke different postsynaptic responses. One good example in crustacean NMJ demonstrated that tonic and phasic motor axons can both form synaptic contacts with the same target cell. A single stimulus in phasic synapses produces much higher postsynaptic responses than tonic synapses; on the other hand, multiple stimuli produces strong facilitation in tonic synapses but depression in phasic synapses (Msghina et al., 1999). Similar diversification was also characterized in cerebellar Purkinje cells in mammalian CNS and other types of neurons, e.g, hippocampal CA3 pyramidal cells.

The origin of synaptic function diversification can be contributed from a number of factors which may also vary among synapses. Postsynaptic factors such as small PSD area, receptor desensitization could lead to depression in short-term plasticity. Presynaptic factors encompasses more variations, including VGCC number, quantal size, number of docked vesicles, VGCC types, proteins regulating Ca^{2+} sensitivity and so on. Although studies found no significant active zone size or docked vesicle differences between tonic and phasic active zones in crustaceans, recent studies in rat hippocampus suggested that synaptic strength scaled linearly with the active zone size (Holderith et al., 2012), and both synaptic strength and plasticity is influenced by VGCC number in the active zone of rat calyces (Sheng et al., 2012).

From our experimental measurements, vesicles in the frog NMJ have lower release probability than the mouse NMJ, and produce much more prominent facilitation than the mouse NMJ. Studies using EM imaging also revealed detailed active zone ultrastructure organized quite differently in the two NMJs. Although these differences might seem obvious across species, and they may potentially rely on a number of differences between the synapses, the active zone's ultrastructure might play an important role in determining synaptic function. We recently hypothesized the *unreliable single vesicle release unit* consisting of docked synaptic vesicle and associated VGCC(s) organized differently at synapses to build active zones (Tarr et al., 2013). We further propose that such organization differences may have deep impact on the synaptic function. Indeed, when applying a previously developed vesicle release model in the frog NMJ directly to mouse NMJ by rearranging the building blocks (docked vesicles and VGCCs) according to the EM imaging data, the models immediately show the striking functional divergences between the two NMJs. This finding directly supported our hypothesis that different active zone organizations using the same building blocks may regulate the synaptic function.

Why would building block arrangements within an active zone affect the synaptic function, especially short-term plasticity? One common observation is that synapses with high initial release are more likely to show depression than facilitation, which sometimes can be explained by depletion of ready-to-release-vesicles in those synapses (Atwood and Karunanithi, 2002; Zucker and Regehr, 2002). In our models, in response to one single action potential, vesicles of frog NMJ indeed show lower average release (0.017) than mouse NMJ (0.104) due to the number of associated VGCCs. However, as shown in Figure-31B most (90%) active zones in mouse NMJ did not have any vesicle release events after the initial stimulus, which suggested no significant vesicle depletion in the terminal. In the frog NMJ, reducing the number of VGCCs near a vesicle surely reduces its vesicle release probability since distant VGCCs contributed to the initial release probabilities (Figure-4.7). However the corresponding facilitation drops in our models' prediction, which is contrary to the common observation. Therefore

high initial release combined with vesicle depletion cannot explain the lack of facilitation in mouse NMJ.

During repetitive stimuli, if a vesicle in the model was already bound by Ca^{2+} from previous stimuli, according to our fusion model, this vesicle (*primed* vesicle) already has a lower fusion energy barrier. Such a vesicle is more likely to release than vesicles clear of any bound Ca^{2+} (*unbound* vesicle). Among all released vesicles, we found a higher percentage of *primed* vesicles in the frog NMJ than in the mouse NMJ (Figure-4.10E and F). This is caused by two observations: (1) the frog NMJ has higher percentage of *primed* vesicles formation than the mouse NMJ (Figure-4.10B); and (2) release probability ratio of *primed*/unbound vesicles is higher in the frog NMJ than in the mouse NMJ (Figure-4.10C and D).

How do these observations correlate to active zone's spatial organization? Ca^{2+} bound to frog NMJ *primed* vesicles came from more than 10 VGCCs whereas Ca^{2+} bound to mouse NMJ *primed* vesicles came from only around 4 VGCCs. Obviously, such differences arise from spatial distribution of VGCCs around vesicles. Firstly, vesicles in frog NMJ model are associated with only one VGCC compared to two VGCCs in mouse NMJ. This leads to lower vesicle release probability in frog despite of its larger active zone size. Secondly, VGCCs in the frog NMJ are approximately spaced linearly from each vesicle, thus a number of neighboring VGCCs can contribute to form *primed* vesicles without triggering release initially, while these neighboring VGCCs can still influence vesicle release later. On the other hand, with two associated VGCCs per vesicle packed in a small active zone, vesicles in mouse NMJ are triggered to release more effectively, leaving less formation opportunities for the *primed* vesicles. In addition, VGCCs from other active zones in mouse NMJ are too far away to influence both formation and release of the *primed* vesicles. As a consequence, not enough *primed*

vesicle formation and not enough enhanced *primed* vesicle release (compared to *unbound* vesicle) together lead to the lack of facilitation in mouse NMJ.

Our findings revealed how spatial organization of these *unreliable vesicle release unit* affected synaptic function, suggesting the importance of organization rather than merely active zone morphological features such as size, number of docked vesicles, etc. Studies show that short-term plasticity intensities may vary among individual axons of the frog NMJ, while freeze-fracture EM imaging presented frog NMJ active zone with fluctuating vesicle-VGCC distances (Propst, 1985). Thus it is possible that such short-term plasticity diversification within frog NMJ originates from subtle variations of these active zone building blocks, which provides homeostatic regulations within NMJ.

After a single action potential stimulus, we found in the frog NMJ model that most Ca^{2+} bound to a released vesicle came from the associated VGCC (Figure-4.7). This finding is consistent with previous studies (Stanley, 1993; Shahrezaei et al., 2006) that vesicle release in frog NMJ follows the nanodomain coupling. However, under repetitive stimuli, Ca^{2+} ions from more VGCCs can bind to released vesicles especially the *primed* vesicles, presenting the trend of a transition from nanodomain into microdomain coupling (Figure-4.12A). The mouse NMJ has similar scenario under single stimulus, when vesicle release is mostly triggered by the two associated VGCCs, and hardly influenced by majority of VGCCs in other active zones distant away (Figure-4.8D). However, unlike frog NMJ, the nanodomain coupling in mouse NMJ barely changes under repetitive stimuli (Figure-4.12B).

In summary, here we show how spatial organization of active zones may affect synaptic function using two models with differently organized active zone building blocks. Beyond that, there is still no clear answer whether the widely observed synaptic function diversification originates from molecular or morphological variations. While the EM imaging can only provide static morphological information within active zones, the *in.vivo* single active zone level details of vesicle release revealed by new

techniques such as super-resolution imaging, along with computer modeling, may shed light on our further understandings.

§ Chapter 5. Discussion

In this chapter, I will discuss findings from my thesis work and address possible future directions.

My thesis consists of two major goals:

1. Construct a vesicle release model at the frog NMJ that predicts short-term plasticity.
2. Investigate the structure-function relationship in synaptic active zone via MCell simulations of the frog and mouse NMJ.

Since I have successfully built such a model satisfying Goal 1, in section 5.1, I will discuss how we can gain further insights into the vesicle fusion and short-term plasticity mechanisms from this model. Also I will address a few concerns regarding the model. Section 5.2 will focus on how to gain deeper understanding of the active zone structure-function relationship following our modeling paradigm. Finally, section 5.3 concludes all the thesis work.

5.1 Exploration of short-term plasticity mechanisms

A range of mechanisms have been proposed to underlie the short-term plasticity (Zucker and Regehr, 2002), however so far none of them have been conclusively identified. As a first step in my thesis work, I found that there were insufficient free residual Ca^{2+} ions in the modeled frog NMJ terminal accounting for facilitation due to Ca^{2+} buffering; in the meanwhile I found the highly localized Ca^{2+} domain at frog NMJ also limited the effects of residual Ca^{2+} ions. In addition, my results suggested that the dwell time of Ca^{2+} ion on synaptotagmin was too low for facilitation, and thus facilitation likely derives from a more complex scenario.

Motivated by biochemical evidences of Ca^{2+} bound synaptotagmin/lipid membrane interactions (Lynch et al., 2007), I added a persistent state to the model and successfully predicted the facilitation observed in frog NMJ. Although due to its simplicity, the persistent binding site model did not fully capture the effects of exogenous buffer, it is still a very interesting model that for the first time to our knowledge correlates synaptotagmin/membrane interaction with short-term plasticity.

The involvement of multiple, spatially and kinetically distinct Ca^{2+} binding sensors have been proposed earlier (Zucker and Regehr, 2002), unfortunately no molecule candidate of the second binding sensor accounting for facilitation has been identified yet. Here I developed a vesicle release model with a second type of binding sensor accounting for short-term plasticity observed in frog NMJ. The modeled synaptic vesicle has 40 synaptotagmin binding sensors, corresponding to 8 synaptotagmin molecules. I have shown that 16 second binding sensors with low dissociation rates suffice to account for the observed facilitation at frog NMJ, suggesting a relative low number of the second binding sensors compared to the synaptotagmin binding sensors. The second binding site vesicle release model also included a novel stochastic energy sampling process, in which additional Ca^{2+} binding to a vesicle resulted in reduced fusion energy barrier and lead to increased release probability.

Both persistent binding site model and the second binding sensor model inherited the majority components from the original excess binding site model (Dittrich et al., 2013) including the 40 synaptotagmin binding sites with unanimous kinetics. On the other hand, biochemical studies suggested kinetic heterogeneity among the five Ca^{2+} binding sites dwelling on C2A and C2B domains of synaptotagmin (Radhakrishnan et al., 2009). To further complicate the matter, Ca^{2+} binding kinetics might be cooperative between individual binding sites. Specifically, if one binding site is occupied by Ca^{2+} ion, kinetics of others might be affected. Therefore it might be interesting see how kinetic

heterogeneity of synaptotagmin binding sites may bring additional effects on vesicle release using our models.

Given the morphological and functional diversification among synapses, it is likely that different short-term plasticity mechanisms may dominate at different synapses. One such mechanism suggests that facilitation is caused by saturation of local endogenous buffer (Blatow et al., 2003; Matveev et al., 2004). If buffer molecules are static, captured Ca^{2+} ions will later be released in the same region. On the other hand if buffer molecules are mobile, bound Ca^{2+} ions will be moved via buffer diffusion and released away from where they bound. Since real synapses are filled with both static and mobile buffer molecules (Eggermann et al., 2012), the diffusion constant of endogenous buffer is an important factor influencing residual Ca^{2+} level. My current model included 2 mM of static endogenous buffer which is an approximation of the reality. Since we don't know the exact concentration for either static and mobile buffer at the modeled NMJs, a tentative simulation adding the same concentration of mobile and static buffer (2 mM) turns out too expensive for practical computing, as MCell at each iteration has to update positions for large amount of newly added mobile buffer molecules. Since most mobile buffer in the terminal never binds to a Ca^{2+} ions during an entire simulation, it is possible to restrict mobile buffer within regions close to vesicles. This would approximate the effects of adding mobile buffer into terminal without involving large numbers of additional molecules in simulation.

Another short-term plasticity mechanism that I did not consider is VGCC facilitation. Studies in the calyx of Held suggested that facilitation may be mediated by Ca^{2+} binding to neuronal- Ca^{2+} -sensor proteins (NCS) which directly enhance Ca^{2+} flux through P/Q type VGCCs during repeated stimuli (Catterall and Few, 2008; Mochida et al., 2008; Catterall et al., 2013). Therefore a future MCell model involving VGCC facilitation mechanism would incorporate details of Ca^{2+} binding with NCS and in addition, how NCS affects VGCC conductance through molecular interactions.

Finally, it is likely that facilitation *in vivo* is triggered by the simultaneous action of a variety of mechanisms. As discussed in Chapter 3, it might be possible that persistent binding site added additional facilitation effects to the second Ca^{2+} sensor, which leads to a hybrid model of persistent binding and second binding sensors better explaining the gap between simulated and experimental facilitation. It is also possible that any of our facilitation model collaborated with buffer saturation mechanism may explain those gap. On the other hand, physiological studies suggested multiple time scale of short-term plasticity enhancement including augmentation and potentiation which has longer time scale than facilitation, whereas facilitation itself also consists of F1 and F2 components with distinct time scale (Zucker and Regehr, 2002). Thus a mixture model with kinetics of multiple time scale may also be required to explain these short-term plasticity phenomena.

Besides exploration of short-term plasticity mechanisms, an improvement of MCell functions enabling conditional activities would be beneficial. The conditional activities refers to changing simulation setup (e.g., reaction rates) when certain conditions (eg., quantity of some molecules reaches some value) are satisfied during the simulation. With conditional activities it is easier to model cooperatively between molecules compared to current version of MCell which only has pre-determined reaction rates. Its direct advantage on my thesis work is that persistent binding transitions can be implemented in MCell simulation instead of using an *ad-hoc* post-simulation analysis as shown in Chapter 3, which in turn makes development of the hybrid model straight-forward.

5.2 Exploration of structure-function relationship in active zone

In my thesis, I constructed a mouse NMJ model by rearranging the unreliable *single vesicle release site* (docked vesicle and VGCC) used in frog NMJ model, and successfully predicted the synaptic function diversifications between two NMJs. I also show that spatial organization of VGCCs influenced formation and release of *primed* vesicles, which in turn influenced short-term plasticity at synapses. In this section, I will discuss how to further explore the structure-function relationship in active zone using our model.

5.2.1 Refining the model with emerging new experimental data

Although freeze-fracture EM imaging indicated possible VGCC locations at the sites of intramembraneous particles, it does not provide direct evidence of the quantity of VGCCs' and their exact positions with respect to docked synaptic vesicles. The frog NMJ vesicle release model in my thesis features fixed VGCC sites regularly laid beside the row of docked vesicles, while the number of VGCCs is determined by a 1:1 vesicle-VGCC stoichiometry predicted by previous work (Luo et al., 2011). With the power of emerging super-resolution imaging, it now becomes possible to directly determine density and distribution of VGCCs within the active zone at high resolution. Therefore one can refine the frog NMJ model with better constraints on VGCC number and location, and make more faithful predictions using the model.

5.2.2 Presynaptic homeostatic regulation of structure and function within active zones of frog NMJ

Previous studies show that when muscle fiber changes its size, the nerve terminal adjusts its size accordingly with increased number of active zones, which ensures nerve terminal releases sufficient neurotransmitter to effectively activate muscle fiber (Slater, 2008; Chen et al., 2012). Intracellular recordings from Dr. Meriney's lab suggested significant variations within the quantal content and short-term plasticity within the frog NMJ. Since size of individual active zones do not seem to be different from EM imaging studies (Pawson et al., 1998), it is possible that these variations between active zones originates from heterogeneity in the organization of individual *single vesicle release sites*. In fact, as shown in section 4.2.8, varying the VGCC/vesicle distance indeed affected the short-term plasticity. Thus it is possible that synapses carefully regulate the number of VGCCs and where the VGCCs are positioned to modulate the synaptic efficacy in a homeostatic manner.

5.2.3 Presynaptic changes in active zone structure in a mouse model of LEMs

The Lambert-Eaton Myasthenic Syndrome (LEM) is a neurological disease that disrupts the organized active zone structure with reduced number of intramembrane particles (Fukunaga et al., 1983; Nagel et al., 1988; Vincent et al., 1989). The type of VGCCs is also changed in LEMs active zones. In the normal mouse NMJ, only P/Q-type VGCC is the major contributor to vesicle release, whereas in LEMs model mice, the literature suggested that both P/Q and N-type VGCC are available (Szabo et al., 2006) due to the reported homeostatic plasticity (Xu et al., 1998; Urbano et al., 2003; Pagani et al., 2004). These changes (Figure-5.1) lead to decreased Ca^{2+} ion influx into the terminal, and

consequently decreased vesicle release and increased facilitation (Tarr et al., 2013). Combining the existing mouse NMJ model developed in my thesis work, and new physiological and super resolution imaging data obtained from LEMS model mice, we may gain deep understanding of how synaptic function is affected by active zone organization, as well as channel type variations, leading to a better understanding of the disease.

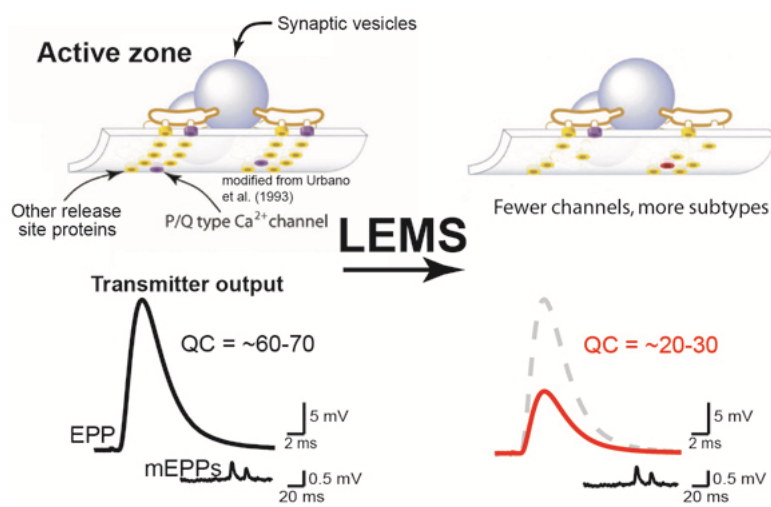


Figure-5.1: Effect of LEMS on the active zone and vesicle release. At the top, the mammalian active zone in control (left) and LEMS conditions (right). In the LEMS condition, there are fewer VGCC and the AZ organization is disrupted. On the bottom, the effect of LEMS on transmitter output (quantal content; QC) is diagramed. LEMS reduces the magnitude of vesicle released during action potential stimuli (EPPs) without changing spontaneous transmitter release (mEPPs).

5.2.4 Unreliable single vesicle release sites at CNS synapses

Although my thesis work is all based on synapses at NMJs, it is also possible that *unreliable single vesicle release sites* are active zone building blocks at the central nervous system (CNS). One possible example is the mature rat calyx of Held synapse (~P14 or older), which is a popular model

system due to easy accessibility of its presynaptic terminal. The probability of vesicle fusion at this synapse is very low (~ 0.13) (Taschenberger et al., 2002) and possibly there only a small number of VGCCs contributed to release (Fedchyshyn and Wang, 2005; Kochubey et al., 2009). Interestingly the immature rat calyx of Held synapse ($\sim P8$ - $P10$) seems to have more VGCCs triggering vesicle release (Borst and Sakmann, 1999; Fedchyshyn and Wang, 2005), indicating a transition from microdomain to nanodomain as the synapse matures (Tarr et al., 2013).

Another example is the dentate gyrus basket cell-granule cell (BC-GC) synapse. Active zones in this synapse appear to have a release probability of ~ 0.5 and estimated releasable vesicles at around 50 at each active zone (Kraushaar and Jonas, 2000), so that each vesicle has a very low release probability. Ultrastructural studies also show a short distance between VGCC and docked vesicle (Bucurenciu et al., 2008), suggesting a nanodomain coupling within the single vesicle release site.

Given the low release probability and nanodomain coupling, active zones these CNS synapses are likely to be built by the *unreliable single vesicle release sites*. Additional insights into these synapses still rely on further experimental studies along with computational modeling.

5.3 Conclusions

In my thesis work, I successfully built an experimentally constrained vesicle release model at the frog NMJ that predicts short-term plasticity, where new insights of vesicle fusion and short-term plasticity are provided during the model development. Further, by rearranging active zone building blocks within the frog NMJ model, I successfully constructed a mouse NMJ model that predicted functional divergence between the two synapses. By tuning active zone organization and tracking Ca^{2+} , I was able to show how active zone organization could affect synaptic function.

My thesis work provided a foundation for future investigations. In particular, starting from my thesis work, it is possible to investigate various short-term plasticity mechanisms at different synapses. Also, the structural and functional relationship at both normal and LEMs active zones can be systematically studied using my model combined with new experimental data. While fully understanding vesicle release and active zone function remains challenging for the neuroscience community, my thesis work stands as an example of collaboration efforts between experimental and theoretical expertise. For the biological modeling community, my thesis work also makes a good example illustrating how spatial-realistic modeling collides with experimental hypothesis.

Bibliography

Adesnik H, Scanziani M. Lateral competition for cortical space by layer-specific horizontal circuits.

Nature 464: 1155–60, 2010.

Andrews SS, Addy NJ, Brent R, Arkin AP. Detailed simulations of cell biology with Smoldyn 2.1.

PLoS Comput. Biol. 6: e1000705, 2010.

Aradi I, Erdi P. Multicompartmental modeling of neural circuits in the olfactory bulb. [Online]. *Int. J.*

Neural Syst. 7: 519–27, 1996. <http://www.ncbi.nlm.nih.gov/pubmed/8968843> [12 Mar. 2014].

Atluri PP, Regehr WG. Determinants of the time course of facilitation at the granule cell to Purkinje cell synapse. [Online]. *J. Neurosci.* 16: 5661–5671, 1996.

<http://www.ncbi.nlm.nih.gov/pubmed/8795622>.

Atwood HL, Karunanithi S. Diversification of synaptic strength: presynaptic elements. *Nat. Rev.*

Neurosci. 3: 497–516, 2002.

Bai J, Wang P, Chapman ER. C2A activates a cryptic Ca²⁺-triggered membrane penetration activity within the C2B domain of synaptotagmin I [Online]. *Proc. Natl. Acad. Sci. U. S. A.* 99: 1665–1670, 2002.

<http://www.pubmedcentral.nih.gov/articlerender.fcgi?artid=122248&tool=pmcentrez&rendertype=abstract>.

Bennett MR, Farnell L, Gibson WG. The facilitated probability of quantal secretion within an array of calcium channels of an active zone at the amphibian neuromuscular junction. *Biophys. J.* 86: 2674–90, 2004.

Bennett MR, Gibson WG, Robinson J. Probabilistic secretion of quanta and the synaptosecretosome hypothesis: evoked release at active zones of varicosities, boutons, and endplates. *Biophys. J.* 73: 1815–29, 1997.

Bertram R, Sherman A, Stanley EF. Single-domain/bound calcium hypothesis of transmitter release and facilitation. [Online]. *J. Neurophysiol.* 75: 1919–31, 1996.
<http://www.ncbi.nlm.nih.gov/pubmed/8734591> [19 Jun. 2013].

Blatow M, Caputi A, Burnashev N, Monyer H, Rozov A. Ca²⁺ buffer saturation underlies paired pulse facilitation in calbindin-D28k-containing terminals. [Online]. *Neuron* 38: 79–88, 2003.
<http://www.ncbi.nlm.nih.gov/pubmed/12691666> [18 Jun. 2013].

Blundon J a, Wright SN, Brodwick MS, Bittner GD. Residual free calcium is not responsible for facilitation of neurotransmitter release. [Online]. *Proc. Natl. Acad. Sci. U. S. A.* 90: 9388–92, 1993.
<http://www.pubmedcentral.nih.gov/articlerender.fcgi?artid=47573&tool=pmcentrez&rendertype=abstract>.

Bommert K, Charlton MP, DeBello WM, Chin GJ, Betz H, Augustine GJ. Inhibition of neurotransmitter release by C2-domain peptides implicates synaptotagmin in exocytosis. *Nature* 363: 163–5, 1993.

Borst JG, Sakmann B. Effect of changes in action potential shape on calcium currents and transmitter release in a calyx-type synapse of the rat auditory brainstem. *Philos. Trans. R. Soc. Lond. B. Biol. Sci.* 354: 347–55, 1999.

Bradacs H, Cooper R, Msghina M, Atwood H. Differential physiology and morphology of phasic and tonic motor axons in a crayfish limb extensor muscle [Online]. *J. Exp. Biol.* 200: 677–91, 1997. <http://www.ncbi.nlm.nih.gov/pubmed/9318419>.

Brette R, Rudolph M, Carnevale T, Hines M, Beeman D, Bower JM, Diesmann M, Morrison A, Goodman PH, Harris FC, Zirpe M, Natschläger T, Pecevski D, Ermentrout B, Djurfeldt M, Lansner A, Rochel O, Vieville T, Muller E, Davison AP, El Boustani S, Destexhe A. Simulation of networks of spiking neurons: a review of tools and strategies. *J. Comput. Neurosci.* 23: 349–98, 2007.

Bucurenciu I, Kulik A, Schwaller B, Frotscher M, Jonas P. Nanodomain coupling between Ca²⁺ channels and Ca²⁺ sensors promotes fast and efficient transmitter release at a cortical GABAergic synapse. *Neuron* 57: 536–45, 2008.

Catterall WA, Few AP. Calcium channel regulation and presynaptic plasticity. *Neuron* 59: 882–901, 2008.

Catterall WA, Leal K, Nanou E. Calcium channels and short-term synaptic plasticity. *J. Biol. Chem.* 288: 10742–9, 2013.

Chapman ER. How does synaptotagmin trigger neurotransmitter release? *Annu. Rev. Biochem.* 77: 615–41, 2008.

Chen J, Mizushige T, Nishimune H. Active zone density is conserved during synaptic growth but impaired in aged mice. *J. Comp. Neurol.* 520: 434–52, 2012.

Cho S, Meriney SD. The effects of presynaptic calcium channel modulation by roscovitine on transmitter release at the adult frog neuromuscular junction. *Eur. J. Neurosci.* 23: 3200–8, 2006.

Coggan JS, Bartol TM, Esquenazi E, Stiles JR, Lamont S, Martone ME, Berg DK, Ellisman MH, Sejnowski TJ. Evidence for ectopic neurotransmission at a neuronal synapse. *Science* 309: 446–51, 2005.

Cowan AE, Moraru II, Schaff JC, Slepchenko BM, Loew LM. Spatial modeling of cell signaling networks. *Methods Cell Biol.* 110: 195–221, 2012.

Czech J, Dittrich M, Stiles JR. Rapid creation, Monte Carlo simulation, and visualization of realistic 3D cell models. *Methods Mol. Biol.* 500: 237–87, 2009.

Davis a F, Bai J, Fasshauer D, Wolowick MJ, Lewis JL, Chapman ER. Kinetics of synaptotagmin responses to Ca²⁺ and assembly with the core SNARE complex onto membranes. [Online]. *Neuron* 24: 363–376, 1999. <http://www.ncbi.nlm.nih.gov/pubmed/10571230>.

Delaney K, Tank DW, Zucker RS. Presynaptic Transmitter Calcium and Serotonin-mediated Enhancement Release at Crayfish Neuromuscular Junction. *J. Neurosci.* 11: 2631–2643, 1991.

Delaney KR, D.W. T. Measurement of the Dependence Synaptic Enhancement on Presynaptic Residual of Short-Term Calcium. *J. Neurosci.* 14: 5885–5902, 1994.

Delaney KR, Tank DW. A quantitative measurement of the dependence of short-term synaptic enhancement on presynaptic residual calcium. [Online]. *J. Neurosci.* 14: 5885–5902, 1994.
<http://www.ncbi.nlm.nih.gov/pubmed/7931551>.

DiAntonio A, Parfitt KD, Schwarz TL. Synaptic transmission persists in synaptotagmin mutants of *Drosophila*. *Cell* 73: 1281–1290, 1993.

Dittman JS, Kreitzer AC, Regehr WG. Interplay between facilitation, depression, and residual calcium at three presynaptic terminals. [Online]. *J. Neurosci.* 20: 1374–85, 2000.
<http://www.ncbi.nlm.nih.gov/pubmed/10662828> [17 Jun. 2013].

Dittrich M, Pattillo JM, King JD, Cho S, Stiles JR, Meriney SD. An excess-calcium-binding-site model predicts neurotransmitter release at the neuromuscular junction. *Biophys. J.* 104: 2751–63, 2013.

Dodge FA, Rahamimoff R. Co-operative action a calcium ions in transmitter release at the neuromuscular junction. [Online]. *J. Physiol.* 193: 419–32, 1967.
<http://www.pubmedcentral.nih.gov/articlerender.fcgi?artid=1365607&tool=pmcentrez&rendertype=abstract> [18 Jun. 2013].

Eccles J, Katz B, Kuffler SW. Nature of the “endplate potential” in curarized muscle.

J. Neurophysiol 4: 362–87, 1941.

Eggermann E, Bucurenciu I, Goswami SP, Jonas P. Nanodomain coupling between Ca²⁺ channels and sensors of exocytosis at fast mammalian synapses. *Nat. Rev. Neurosci.* 13: 7–21, 2012.

Faeder JR. Toward a comprehensive language for biological systems. *BMC Biol.* 9: 68, 2011.

Fatt P, Katz B. The electrical properties of crustacean muscle fibers. *Journal Physiol.* 120: 171–204, 1953.

Fedchyshyn MJ, Wang L-Y. Developmental transformation of the release modality at the calyx of Held synapse. *J. Neurosci.* 25: 4131–40, 2005.

Feng T. The changes in the end-plate potential during and after prolonged stimulation. *Chin. J. Physiol* 13: 79–107, 1941.

Fisher SA, Fischer TM, Carew TJ. Multiple overlapping processes underlying short-term synaptic enhancement. *Trends Neurosci.* 20: 170–7, 1997.

Fukuda M, Moreira JE, Liu V, Sugimori M, Mikoshiba K, Llinás RR. Role of the conserved WHXL motif in the C terminus of synaptotagmin in synaptic vesicle docking. *Proc. Natl. Acad. Sci. U. S. A.* 97: 14715–9, 2000.

Fukunaga H, Engel AG, Lang B, Newsom-Davis J, Vincent A. Passive transfer of Lambert-Eaton myasthenic syndrome with IgG from man to mouse depletes the presynaptic membrane active zones. [Online]. *Proc. Natl. Acad. Sci. U. S. A.* 80: 7636–40, 1983.
<http://www.pubmedcentral.nih.gov/articlerender.fcgi?artid=534395&tool=pmcentrez&rendertype=abstract> [29 Mar. 2014].

Galbraith CG, Galbraith JA. Super-resolution microscopy at a glance. *J. Cell Sci.* 124: 1607–11, 2011.

Gao Y, Zorman S, Gundersen G, Xi Z, Ma L, Sirinakis G, Rothman JE, Zhang Y. Single reconstituted neuronal SNARE complexes zipper in three distinct stages. *Science (80-.)*. 337: 1340–3, 2012.

Geppert M, Goda Y, Hammer RE, Li C, Rosahl TW, Stevens CF, Südhof TC. Synaptotagmin I: A major Ca²⁺ sensor for transmitter release at a central synapse. *Cell* 79: 717–727, 1994.

Gilula NB, Feldman J. *Intercellular Junctions and Synapses*. London: Chapman & Hall, 1978.

Grimes WN, Zhang J, Graydon CW, Kachar B, Diamond JS. Retinal parallel processors: more than 100 independent microcircuits operate within a single interneuron. *Neuron* 65: 873–85, 2010.

Gupta A, Wang Y, Markram H. Organizing principles for a diversity of GABAergic interneurons and synapses in the neocortex. [Online]. *Science* 287: 273–8, 2000.

<http://www.ncbi.nlm.nih.gov/pubmed/10634775> [15 Mar. 2014].

Harlow ML, Ress D, Stoschek a, Marshall RM, McMahan UJ. The architecture of active zone material at the frog’s neuromuscular junction. [Online]. *Nature* 409: 479–484, 2001.

<http://www.ncbi.nlm.nih.gov/pubmed/11206537>.

Hasting W. Monte Carlo Sampling Methods Using Markov Chains and Their Applications. *Biometrika* 57: 97–109, 1970.

Heilemann M, Herten DP, Heintzmann R, Cremer C, Muller C, Tinnefeld P, Weston KD, Wolfrum J, Sauer M. High-resolution colocalization of single dye molecules by fluorescence lifetime imaging microscopy. [Online]. *Anal. Chem.* 74: 3511–7, 2002.

<http://www.ncbi.nlm.nih.gov/pubmed/12139062> [16 Aug. 2013].

Hein B, Willig KI, Hell SW. Stimulated emission depletion (STED) nanoscopy of a fluorescent protein-labeled organelle inside a living cell. *Proc. Natl. Acad. Sci. U. S. A.* 105: 14271–6, 2008.

Heuser JE, Reese TS, Dennis MJ, Jan Y, Jan L, Evans L. Synaptic vesicle exocytosis captured by quick freezing and correlated with quantal transmitter release. *J. Cell Biol.* 81: 275–300, 1979.

Heuser JE, Reese TS, Landis DM. Functional changes in frog neuromuscular junctions studied with freeze-fracture. [Online]. *J. Neurocytol.* 3: 109–31, 1974.

<http://www.ncbi.nlm.nih.gov/pubmed/4596345> [11 Apr. 2014].

Heuser JE, Salpeter SR. Organization of acetylcholine receptors in quick-frozen, deep-etched, and rotary-replicated Torpedo postsynaptic membrane. [Online]. *J. Cell Biol.* 82: 150–173, 1979.

<http://www.pubmedcentral.nih.gov/articlerender.fcgi?artid=2110412&tool=pmcentrez&rendertype=abstract>.

Heuser JE. Review of electron microscopic evidence favouring vesicle exocytosis as the structural basis for quantal release during synaptic transmission. [Online]. *Q. J. Exp. Physiol.* 74: 1051–69, 1989.

<http://www.ncbi.nlm.nih.gov/pubmed/2560556> [18 Jun. 2013].

Holderith N, Lorincz A, Katona G, Rózsa B, Kulik A, Watanabe M, Nusser Z. Release probability of hippocampal glutamatergic terminals scales with the size of the active zone. *Nat. Neurosci.* 15: 988–97, 2012.

Holohean AM, Magleby KL. The number of components of enhancement contributing to short-term synaptic plasticity at the neuromuscular synapse during patterned nerve Stimulation progressively decreases as basal release probability is increased from low to normal levels by changing . *J. Neurosci.* 31: 7060–72, 2011.

Hua Y, Scheller RH. Three SNARE complexes cooperate to mediate membrane fusion. [Online].

Proc. Natl. Acad. Sci. U. S. A. 98: 8065–8070, 2001.

<http://www.pubmedcentral.nih.gov/articlerender.fcgi?artid=35468&tool=pmcentrez&rendertype=abstract>.

Hui E, Bai J, Chapman ER. Ca²⁺-triggered simultaneous membrane penetration of the tandem C2-domains of synaptotagmin I. *Biophys. J.* 91: 1767–77, 2006.

Hui E, Bai J, Wang P, Sugimori M, Llinas RR, Chapman ER. Three distinct kinetic groupings of the synaptotagmin family: candidate sensors for rapid and delayed exocytosis. [Online]. *Proc. Natl. Acad. Sci. U. S. A.* 102: 5210–5214, 2005.

<http://www.pubmedcentral.nih.gov/articlerender.fcgi?artid=556003&tool=pmcentrez&rendertype=abstract>.

Kaesler PS, Deng L, Wang Y, Dulubova I, Liu X, Rizo J, Südhof TC. RIM proteins tether Ca²⁺ channels to presynaptic active zones via a direct PDZ-domain interaction. *Cell* 144: 282–95, 2011.

Kamly H, Zucker R. Residual Ca²⁺ and short-term synaptic plasticity. *Nature* 371: 603–606, 1994.

Karr JR, Sanghvi JC, Macklin DN, Gutschow M V, Jacobs JM, Bolival B, Assad-Garcia N, Glass JJ, Covert MW. A whole-cell computational model predicts phenotype from genotype. *Cell* 150: 389–401, 2012.

Katz B, Miledi R. The effects of temperature on the synaptic delay at the neuromuscular junction. *J. Physiol* 181: 656–670, 1965a.

Katz B, Miledi R. The effects of calcium on acetylcholine release from motor nerve terminals. *Proc R Soc L B Biol Sci* 161: 496–503, 1965b.

Katz B, Miledi R. The role of calcium in neuromuscular facilitation. [Online]. *J. Physiol.* 195: 481–92, 1968.

<http://www.pubmedcentral.nih.gov/articlerender.fcgi?artid=1351674&tool=pmcentrez&rendertype=abstract> [10 Jun. 2013].

Kerr LM, Yoshikami D. A venom peptide with a novel presynaptic blocking action. [Online]. *Nature* 308: 282–4, 1984. <http://www.ncbi.nlm.nih.gov/pubmed/6608056> [10 Mar. 2014].

Kerr RA, Bartol TM, Kaminsky B, Dittrich M, Chang J-CJ, Baden SB, Sejnowski TJ, Stiles JR. Fast Monte Carlo simulation methods for biological reaction-diffusion systems in solution and on surfaces. *SIAM J. Sci. Comput.* 30: 3126, 2008.

Khalili-Araghi F, Gumbart J, Wen P-C, Sotomayor M, Tajkhorshid E, Schulten K. Molecular dynamics simulations of membrane channels and transporters. *Curr. Opin. Struct. Biol.* 19: 128–37, 2009.

Kinney JP, Spacek J, Bartol TM, Bajaj CL, Harris KM, Sejnowski TJ. Extracellular sheets and tunnels modulate glutamate diffusion in hippocampal neuropil. *J. Comp. Neurol.* 521: 448–64, 2013.

Kochubey O, Han Y, Schneggenburger R. Developmental regulation of the intracellular Ca²⁺ sensitivity of vesicle fusion and Ca²⁺-secretion coupling at the rat calyx of Held. *J. Physiol.* 587: 3009–23, 2009.

Kraushaar U, Jonas P. Efficacy and stability of quantal GABA release at a hippocampal interneuron-principal neuron synapse. [Online]. *J. Neurosci.* 20: 5594–607, 2000.
<http://www.ncbi.nlm.nih.gov/pubmed/10908596> [15 Apr. 2014].

Kuffler SW, Yoshikami D. The distribution of acetylcholine sensitivity at the post-synaptic membrane of vertebrate skeletal twitch muscles: iontophoretic mapping in the micron range. [Online]. *J. Physiol.* 244: 703–30, 1975.
<http://www.pubmedcentral.nih.gov/articlerender.fcgi?artid=1330831&tool=pmcentrez&rendertype=abstract> [18 Jun. 2013].

Li F, Pincet F, Perez E, Eng WS, Melia TJ, Rothman JE, Tareste D. Energetics and dynamics of SNAREpin folding across lipid bilayers. *Nat. Struct. Mol. Biol.* 14: 890–6, 2007a.

Li H, Cao Y, Petzold LR, Gillespie DT. Algorithms and software for stochastic simulation of biochemical reacting systems. *Biotechnol. Prog.* 24: 56–61, 2008.

Li L, Bischofberger J, Jonas P. Differential gating and recruitment of P/Q-, N-, and R-type Ca²⁺ channels in hippocampal mossy fiber boutons. *J. Neurosci.* 27: 13420–9, 2007b.

Liley AW, North KA. An electrical investigation of effects of repetitive stimulation on mammalian neuromuscular junction. [Online]. *J. Neurophysiol.* 16: 509–27, 1953.

<http://www.ncbi.nlm.nih.gov/pubmed/13097199> [18 Aug. 2013].

Littleton JT, Stern M, Schulze K, Perin M, Bellen HJ. Mutational analysis of *Drosophila* synaptotagmin demonstrates its essential role in Ca²⁺-activated neurotransmitter release. *Cell* 74: 1125–1134, 1993.

Lnenicka GA. The Role of Activity in the Development of Phasic and Tonic Synaptic Terminals. *Ann. N. Y. Acad. Sci.* 627: 197–211, 1991.

Luo F, Dittrich M, Stiles JR, Meriney SD. Single-pixel optical fluctuation analysis of calcium channel function in active zones of motor nerve terminals. *J. Neurosci.* 31: 11268–81, 2011.

Lynch KL, Gerona RRL, Larsen EC, Marcia RF, Mitchell JC, Martin TFJ. Synaptotagmin C2A Loop 2 Mediates Ca²⁺-dependent SNARE Interactions Essential for Ca²⁺-triggered Vesicle. 18: 4957–4968, 2007.

Ma J, Kelly L, Ingram J, Price TJ, Meriney SD, Dittrich M. New insights into short-term synaptic facilitation at the frog neuromuscular junction. *Prep.* .

Ma J, Meriney SD, Dittrich M. Functional Impact of Active Zone Organization at the Neuromuscular Junction. *Prep.* .

Magleby KL, Zengel JE. A quantitative description of stimulation-induced changes in transmitter release at the frog neuromuscular junction. [Online]. *J. Gen. Physiol.* 80: 613–38, 1982.
<http://www.pubmedcentral.nih.gov/articlerender.fcgi?artid=2228704&tool=pmcentrez&rendertype=abstract>.

Magleby KL. Facilitation, augmentation, and potentiation of transmitter release. *Prog. Brain Res.* 49: 175–82, 1979.

Magleby KL. Short-term changes in synaptic efficacy. In: *Synaptic Function*, edited by Edelman G, Gall W, WMCowan. New York: Wiley, 1987, p. 21–56.

Malsam J, Kreye S, Söllner TH. Membrane fusion: SNAREs and regulation. *Cell. Mol. Life Sci.* 65: 2814–32, 2008.

Markram H, Gupta A, Uziel A, Wang Y, Tsodyks M. Information processing with frequency-dependent synaptic connections. *Neurobiol. Learn. Mem.* 70: 101–12, 1998.

Martens S, Kozlov MM, McMahon HT. How synaptotagmin promotes membrane fusion. *Science* (80-.). 316: 1205–8, 2007.

Matveev V, Bertram R, Sherman A. Residual bound Ca²⁺ can account for the effects of Ca²⁺ buffers on synaptic facilitation. *J. Neurophysiol.* 96: 3389–97, 2006.

Matveev V, Sherman A, Zucker RS. New and Corrected Simulations of Synaptic Facilitation [Online]. *Biophys. J.* 83: 1368–1373, 2002.

<http://www.sciencedirect.com/science/article/pii/S0006349502739076> [18 Oct. 2013].

Matveev V, Zucker RS, Sherman A. Facilitation through buffer saturation: constraints on endogenous buffering properties. *Biophys. J.* 86: 2691–709, 2004.

Meinrenken CJ, Borst JGG, Sakmann B. Calcium Secretion Coupling at Calyx of Held Governed by Nonuniform Channel – Vesicle Topography [Online]. *J. Neurosci.* 22: 1648–1667, 2002.

<http://www.ncbi.nlm.nih.gov/pubmed/11880495>.

Metropolis N, Rosenbluth A., Rosenbluth M., Teller A., Teller E. Equations of State Calculations by Fast Computing Machines. *J. Chem. Phys.* 21: 1087–92, 1953.

Mikoshiba K, Fukuda M, Moreira JE, Lewis FM, Sugimori M, Niinobe M, Llinas R. Role of the C2A domain of synaptotagmin in transmitter release as determined by specific antibody injection into the squid giant synapse preterminal. *Proc. Natl. Acad. Sci.* 92: 10703–10707, 1995.

Miledi R. Junctional and extra-junctional acetylcholine receptors in skeletal muscle fibres. [Online]. *J. Physiol.* 151: 24–30, 1960.

<http://www.pubmedcentral.nih.gov/articlerender.fcgi?artid=1363215&tool=pmcentrez&rendertype=abstract> [18 Jun. 2013].

Millar AG, Bradacs H, Charlton MP, Atwood HL. Inverse Relationship between Release Probability and Readily Releasable Vesicles in Depressing and Facilitating Synapses [Online]. *J. Neurosci.* 22: 9661–9667, 2002. <http://www.jneurosci.org/content/22/22/9661.long> [12 Aug. 2013].

Millar AG, Zucker RS, Ellis-Davies GCR, Charlton MP, Atwood HL. Calcium sensitivity of neurotransmitter release differs at phasic and tonic synapses. *J. Neurosci.* 25: 3113–25, 2005.

Mochida S, Few AP, Scheuer T, Catterall WA. Regulation of presynaptic Ca(V)2.1 channels by Ca²⁺ sensor proteins mediates short-term synaptic plasticity. *Neuron* 57: 210–6, 2008.

Msghina M, Govind CK, Atwood HL. Synaptic structure and transmitter release in crustacean phasic and tonic motor neurons. [Online]. *J. Neurosci.* 18: 1374–82, 1998. <http://www.ncbi.nlm.nih.gov/pubmed/9454846> [12 Aug. 2013].

Msghina M, Millar AG, Charlton MP, Govind CK, Atwood HL. Calcium Entry Related to Active Zones and Differences in Transmitter Release at Phasic and Tonic Synapses [Online]. *J. Neurosci.* 19: 8419–8434, 1999. <http://www.jneurosci.org/content/19/19/8419.long> [12 Aug. 2013].

Mukhamedyarov M a, Grishin SN, Zefirov AL, Palotás A. The mechanisms of multi-component paired-pulse facilitation of neurotransmitter release at the frog neuromuscular junction. *Pflugers Arch.* 458: 563–70, 2009.

Mukhamedyarov M a, Zefirov AL, Palotás A. Paired-pulse facilitation of transmitter release at different levels of extracellular calcium concentration. *Neurochem. Res.* 31: 1055–8, 2006.

Müller M, Felmy F, Schwaller B, Schneggenburger R. Parvalbumin is a mobile presynaptic Ca²⁺ buffer in the calyx of held that accelerates the decay of Ca²⁺ and short-term facilitation. *J. Neurosci.* 27: 2261–71, 2007.

Nadkarni S, Bartol TM, Sejnowski TJ, Levine H. Modelling vesicular release at hippocampal synapses. *PLoS Comput. Biol.* 6: e1000983, 2010.

Nagel A, Engel AG, Lang B, Newsom-Davis J, Fukuoka T. Lambert-Eaton myasthenic syndrome IgG depletes presynaptic membrane active zone particles by antigenic modulation. *Ann. Neurol.* 24: 552–8, 1988.

Nagwaney S, Harlow ML, Jung JH, Szule J a, Ress D, Xu J, Marshall RM, McMahan UJ. Macromolecular connections of active zone material to docked synaptic vesicles and presynaptic membrane at neuromuscular junctions of mouse. *J. Comp. Neurol.* 513: 457–68, 2009.

Naraghi M, Neher E. Linearized buffered Ca²⁺ diffusion in microdomains and its implications for calculation of [Ca²⁺] at the mouth of a calcium channel. [Online]. *J. Neurosci.* 17: 6961–73, 1997. <http://www.ncbi.nlm.nih.gov/pubmed/9278532>.

Nguyen P V, Marin L, Atwood HL. Synaptic physiology and mitochondrial function in crayfish tonic and phasic motor neurons. [Online]. *J. Neurophysiol.* 78: 281–94, 1997. <http://www.ncbi.nlm.nih.gov/pubmed/9242280> [12 Aug. 2013].

Nicholls JG, Martin AR, Wallace BG, Fuchs PA. *From Neuron to Brain*. 4th ed. Sunderland: Sinauer Associates, Inc, 2000.

Nonet ML, Grundahl K, Meyer BJ, Rand JB. Synaptic function is impaired but not eliminated in *C. elegans* mutants lacking synaptotagmin. *Cell* 73: 1291–1305, 1993.

Oshima A. Structure and closure of connexin gap junction channels. *FEBS Lett.* (February 1, 2014). doi: 10.1016/j.febslet.2014.01.042.

Paddock BE, Wang Z, Biela LM, Chen K, Getzy MD, Striegel A, Richmond JE, Chapman ER, Featherstone DE, Reist NE. Membrane penetration by synaptotagmin is required for coupling calcium binding to vesicle fusion in vivo. *J. Neurosci.* 31: 2248–57, 2011.

Pagani R, Song M, McEnery M, Qin N, Tsien RW, Toro L, Stefani E, Uchitel OD. Differential expression of alpha 1 and beta subunits of voltage dependent Ca²⁺ channel at the neuromuscular junction of normal and P/Q Ca²⁺ channel knockout mouse. [Online]. *Neuroscience* 123: 75–85, 2004. <http://www.ncbi.nlm.nih.gov/pubmed/14667443> [29 Mar. 2014].

Pan B, Zucker RS. A general model of synaptic transmission and short-term plasticity. *Neuron* 62: 539–54, 2009.

Pawson PA, Grinnell AD, Wolowske B. Quantitative freeze-fracture analysis of the frog neuromuscular junction synapse--I. Naturally occurring variability in active zone structure. [Online]. *J. Neurocytol.* 27: 361–77, 1998. <http://www.ncbi.nlm.nih.gov/pubmed/9923981> [20 Jun. 2013].

Plimpton SJ, Slepoy A. Microbial cell modeling via reacting diffusing particles. In: *Journal of physics: Conference Series 16*. 2005, p. 305–309.

Propst W. Correlations Between Active Zone Ultrastructure and Synaptic Function Studied with Freeze-Fracture of Physiologically Identified Neuromuscular Junctions. *J. Neurosci.* 7: 3654–3664, 1985.

Pumplin DW, Reese TS, Llinás R. Are the presynaptic membrane particles the calcium channels? [Online]. *Proc. Natl. Acad. Sci. U. S. A.* 78: 7210–7213, 1981.

<http://www.pubmedcentral.nih.gov/articlerender.fcgi?artid=349226&tool=pmcentrez&rendertype=abstract>.

Radhakrishnan A, Stein A, Jahn R, Fasshauer D. The Ca²⁺ affinity of synaptotagmin 1 is markedly increased by a specific interaction of its C2B domain with phosphatidylinositol 4,5-bisphosphate. *J. Biol. Chem.* 284: 25749–60, 2009.

Rizo J, Rosenmund C. Synaptic vesicle fusion. *Nat. Struct. Mol. Biol.* 15: 665–674, 2009.

Rizo J. Synaptotagmin-SNARE coupling enlightened. *Nat. Struct. Mol. Biol.* 17: 260–2, 2010.

Rust MJ, Bates M, Zhuang X. Sub-diffraction-limit imaging by stochastic optical reconstruction microscopy (STORM). *Nat. Methods* 3: 793–5, 2006.

Schneppenburger R, Neher E. Intracellular calcium dependence of transmitter release rates at a fast central synapse. *Nature* 406: 889–93, 2000.

Scimemi A, Diamond JS. The number and organization of Ca²⁺ channels in the active zone shapes neurotransmitter release from Schaffer collateral synapses. *J. Neurosci.* 32: 18157–76, 2012.

Shahrezaei V, Cao A, Delaney KR. Ca²⁺ from one or two channels controls fusion of a single vesicle at the frog neuromuscular junction. *J. Neurosci.* 26: 13240–9, 2006.

Sheng J, He L, Zheng H, Xue L, Luo F, Shin W, Sun T, Kuner T, Yue DT, Wu L-G. Calcium-channel number critically influences synaptic strength and plasticity at the active zone. *Nat. Neurosci.* 15: 998–1006, 2012.

Sherman RG, Atwood HL. Correlated electrophysiological and ultrastructural studies of a crustacean motor unit. [Online]. *J. Gen. Physiol.* 59: 586–615, 1972.
<http://www.pubmedcentral.nih.gov/articlerender.fcgi?artid=2203193&tool=pmcentrez&rendertype=abstract> [15 Mar. 2014].

Shi L, Shen Q, Kiel A, Wang J, Wang H, Melia TJ, Rothman JE, Pincet F. SNARE Proteins : One to Fuse and Fusion Pore Open. *Science* (80-.). 335: 1355–1359, 2012.

Shin O-H, Lu J, Rhee J-S, Tomchick DR, Pang ZP, Wojcik SM, Camacho-Perez M, Brose N, Machius M, Rizo J, Rosenmund C, Südhof TC. Munc13 C2B domain is an activity-dependent Ca²⁺ regulator of synaptic exocytosis. *Nat. Struct. Mol. Biol.* 17: 280–8, 2010.

Simon SM, Llinás RR. Compartmentalization of the submembrane calcium activity during calcium influx and its significance in transmitter release. *Biophys. J.* 48: 485–98, 1985.

Slater CR. Structural factors influencing the efficacy of neuromuscular transmission. *Ann. N. Y. Acad. Sci.* 1132: 1–12, 2008.

Smith DO. Muscle-Specific Decrease in Presynaptic Calcium Dependence and Clearance During Neuromuscular Transmission in Aged Rats. *J. Neurophysiol.* 59, 1988.

Sørensen JB. Conflicting views on the membrane fusion machinery and the fusion pore. *Annu. Rev. Cell Dev. Biol.* 25: 513–37, 2009.

Stanley EF, Reese TS, Wang GZ. Molecular scaffold reorganization at the transmitter release site with vesicle exocytosis or botulinum toxin C1. *Eur. J. Neurosci.* 18: 2403–2407, 2003.

Stanley EF. Single Calcium Channels and Acetylcholine at a Presynaptic Nerve Terminal. 11: 1007–1011, 1993.

Stiles JR, Bartol TM. Monte Carlo methods for simulating realistic synaptic microphysiology using MCell. In: *Computational Neuroscience: Realistic Modeling of Experimentalists*, edited by De Schutter E. Boca Raton: CRC Press, 2001, p. 87–127.

Stiles JR, Van Helden D, Bartol TM, Salpeter EE, Salpeter MM. Miniature endplate current rise times less than 100 microseconds from improved dual recordings can be modeled with passive acetylcholine diffusion from a synaptic vesicle. [Online]. *Proc. Natl. Acad. Sci. U. S. A.* 93: 5747–52, 1996.
<http://www.pubmedcentral.nih.gov/articlerender.fcgi?artid=39132&tool=pmcentrez&rendertype=abstract> [20 Jun. 2013].

Südhof TC, Malenka RC. Understanding synapses: past, present, and future. *Neuron* 60: 469–76, 2008.

Südhof TC, Rothman JE. Membrane fusion: grappling with SNARE and SM proteins. *Science* 323: 474–7, 2009.

Südhof TC. The presynaptic active zone. *Neuron* 75: 11–25, 2012.

Suzuki S, Osanai M, Murase M, Suzuki N, Ito K, Shirasaki T, Narita K, Ohnuma K, Kuba K, Kijima H. Ca²⁺ dynamics at the frog motor nerve terminal. [Online]. *Pflugers Arch.* 440: 351–65, 2000. <http://www.ncbi.nlm.nih.gov/pubmed/10954322> [7 Jun. 2013].

Szabo Z, Obermair GJ, Cooper CB, Zamponi GW, Flucher BE. Role of the synprint site in presynaptic targeting of the calcium channel CaV2.2 in hippocampal neurons. *Eur. J. Neurosci.* 24: 709–18, 2006.

Takamori S, Holt M, Stenius K, Lemke E a, Grønborg M, Riedel D, Urlaub H, Schenck S, Brügger B, Ringler P, Müller S a, Rammner B, Gräter F, Hub JS, De Groot BL, Mieskes G, Moriyama Y, Klingauf J, Grubmüller H, Heuser J, Wieland F, Jahn R. Molecular anatomy of a trafficking organelle. *Cell* 127: 831–46, 2006.

Tanabe BYN, Kijima H. Ca²⁺-dependent and -independent components of transmitter release at the frog neuromuscular junction. *J. Physiol.* 455: 271–289, 1992.

Tanabe N, Kijima H. Both augmentation and potentiation occur independently of internal Ca²⁺ at the frog neuromuscular junction. [Online]. *Neurosci. Lett.* 99: 147–52, 1989.
<http://www.ncbi.nlm.nih.gov/pubmed/2501716> [17 Jun. 2013].

Tang Y, Schlumpberger T, Kim T, Lueker M, Zucker RS. Effects of Mobile Buffers on Facilitation: Experimental and Computational Studies. *Biophys. J.* 78: 2735–2751, 2000.

Tank DW, Regehr WG, Delaney KR. A quantitative analysis of presynaptic calcium dynamics that contribute to short-term enhancement. [Online]. *J. Neurosci.* 15: 7940–52, 1995.
<http://www.ncbi.nlm.nih.gov/pubmed/8613732> [17 Jun. 2013].

Tarr TB, Dittrich M, Meriney SD. Are unreliable release mechanisms conserved from NMJ to CNS? *Trends Neurosci.* 36: 14–22, 2013.

Taschenberger H, Leão RM, Rowland KC, Spirou GA, von Gersdorff H. Optimizing synaptic architecture and efficiency for high-frequency transmission. [Online]. *Neuron* 36: 1127–43, 2002. <http://www.ncbi.nlm.nih.gov/pubmed/12495627> [3 Apr. 2014].

Thomson AM. Molecular frequency filters at central synapses. [Online]. *Prog. Neurobiol.* 62: 159–96, 2000. <http://www.ncbi.nlm.nih.gov/pubmed/10828382> [15 Mar. 2014].

Urbano FJ, Piedras-Rentería ES, Jun K, Shin H-S, Uchitel OD, Tsien RW. Altered properties of quantal neurotransmitter release at endplates of mice lacking P/Q-type Ca²⁺ channels. [Online]. *Proc. Natl. Acad. Sci. U. S. A.* 100: 3491–3496, 2003. <http://www.pubmedcentral.nih.gov/articlerender.fcgi?artid=152320&tool=pmcentrez&rendertype=abstract>.

Vavylonis D, Kovar DR, O’Shaughnessy B, Pollard TD. Model of formin-associated actin filament elongation. *Mol. Cell* 21: 455–66, 2006.

Vincent A, Lang B, Newsom-Davis J. Autoimmunity to the voltage-gated calcium channel underlies the Lambert-Eaton myasthenic syndrome, a paraneoplastic disorder. [Online]. *Trends Neurosci.* 12: 496–502, 1989. <http://www.ncbi.nlm.nih.gov/pubmed/2480664> [29 Mar. 2014].

Vyleta N, Jonas P. Loose Coupling Between Ca²⁺ Channels and Release Sensors at a Plastic Hippocampal Synapse. *Science (80-.).* 343: 665–670, 2014.

Wachman ES, Poage RE, Stiles JR, Farkas DL, Meriney SD. Spatial Distribution of Calcium Entry Evoked by Single Action Potentials within the Presynaptic Active Zone. *J. Neurosci.* 24: 2877–85, 2004.

Weber AM, Wong FK, Tufford AR, Schlichter LC, Matveev V, Stanley EF. N-type Ca²⁺ channels carry the largest current: implications for nanodomains and transmitter release. *Nat. Neurosci.* 13: 1348–50, 2010.

Wiederhold K, Fasshauer D. Is assembly of the SNARE complex enough to fuel membrane fusion? *J. Biol. Chem.* 284: 13143–52, 2009.

Wiersma CAG. *The Physiology of Crustacea.* New York: Academic, 1961.

Wilkinson DJ. Stochastic modelling for quantitative description of heterogeneous biological systems. *Nat. Rev. Genet.* 10: 122–33, 2009.

Winslow JL, Duffy SN, Charlton MP. Homosynaptic facilitation of transmitter release in crayfish is not affected by mobile calcium chelators: implications for the residual ionized calcium hypothesis from electrophysiological and computational analyses. [Online]. *J. Neurophysiol.* 72: 1769–1793, 1994. <http://www.ncbi.nlm.nih.gov/pubmed/7823101>.

Worden MK, Bykhovskaia M, Hackett JT. Facilitation at the lobster neuromuscular junction: a stimulus-dependent mobilization model. [Online]. *J. Neurophysiol.* 78: 417–28, 1997. <http://www.ncbi.nlm.nih.gov/pubmed/9242290> [20 Aug. 2013].

Wu L-GG, Borst JGG. The reduced release probability of releasable vesicles during recovery from short-term synaptic depression. *Neuron* 23: 821–832, 1999.

Xu T, Naraghi M, Kang H, Neher E. Kinetic studies of Ca²⁺ binding and Ca²⁺ clearance in the cytosol of adrenal chromaffin cells. *Biophys. J.* 73: 532–45, 1997.

Xu YF, Hewett SJ, Atchison WD. Passive transfer of Lambert-Eaton myasthenic syndrome induces dihydropyridine sensitivity of ICa in mouse motor nerve terminals. [Online]. *J. Neurophysiol.* 80: 1056–69, 1998. <http://www.ncbi.nlm.nih.gov/pubmed/9744921> [29 Mar. 2014].

Yamada WM, Zucker RS. Time course of transmitter release calculated from simulations of a calcium diffusion model. *Biophys. J.* 61: 671–82, 1992.

Yazejian B, Sun X, Grinnell AD. Tracking presynaptic Ca²⁺ dynamics during neurotransmitter release with Ca²⁺-activated K⁺ channels. *Nat. Neurosci.* 3: 2–7, 2000.

Young SM, Neher E. Synaptotagmin has an essential function in synaptic vesicle positioning for synchronous release in addition to its role as a calcium sensor. *Neuron* 63: 482–96, 2009.

Zhai RG, Vardinon-Friedman H, Cases-Langhoff C, Becker B, Gundelfinger ED, Ziv NE, Garner CC. Assembling the presynaptic active zone: a characterization of an active one precursor vesicle. [Online]. *Neuron* 29: 131–143, 2001. <http://www.ncbi.nlm.nih.gov/pubmed/11182086>.

Zucker RS, Regehr WG. Short-term synaptic plasticity. *Annu. Rev. Physiol.* 64: 355–405, 2002.

Zucker RS. Short-term synaptic plasticity. *Annu. Rev. Neurosci.* 12: 13–31, 1989.